

6.0 3DCM MODEL POSTTEST ANALYSIS

6.1 Overview of Pretest Model and Focus of Posttest Analysis

The 3DCM model is a detailed representation of a horizontal slice through the PCCV cylinder that extends from elev. 4.67 m to elev. 8.96 m, and extends 360 degrees circumferentially, as shown in Figure 6-1. For modeling convenience, the centerline elevations of the E/H, A/L, and M/S were assumed to be the same (requiring only a few centimeters upward and downward adjustment of these centerlines from their true location). The penetrations, therefore, were represented in vertical half-symmetry. Both buttresses were modeled. The liner was explicitly modeled with shell elements; liner anchors were modeled with beam elements; and rebar was modeled one-for-one with rebar subelements. The liner grid density was not as fine as for the individual local models, so the 3DCM model was not used to predict peak local liner strains. The grid was considered fine enough, however, to represent the stiffness and yielding behavior of the liner in order to predict displacement versus pressure histories at the boundaries of local models. A more detailed description of the 3DCM model, its objectives, and pretest results can be found in [1]. Some results of the final pretest 3DCM model were shown in Chapter 2.

The modeling of the hoop and vertical tendons in the 3DCM is analogous to that described for the axisymmetric model meridional dome tendons. Each tendon was modeled with a truss element and friction truss-ties to adjacent concrete nodes, as shown in Figure 6-2. The tie elements have a length equal to the radius of the tendon ducts. When the tendon is curved, the truss ties are oriented at an angle of $\arctan(0.21)$, because the coefficient of angular friction used in the model design and assumed for its behavior was 0.21. By assigning this system of tendon elements small displacement theory, the friction truss-ties always transmit the exact amount of theoretical angular friction force from the tendon to the concrete. When the tendon segment being tied is straight, the tie element is oriented perpendicular to the tendon (no friction). Thus, wobble friction along straight runs of tendon is not modeled directly. Wobble friction was considered, however, in estimating tendon stresses at the boundaries of the models. Anchor set losses were simulated by reversing the orientation of the friction truss elements over the anchor set loss zone. The length of this zone was predetermined from design calculations to be 37.5 degrees from the buttress centerline, as shown in Figure 2-14.

Because the model and tendons deform during prestress equilibration, the anchor stress application required several trial iterations to achieve the desired anchor force on all tendons at the end of the prestress loading step. The hoop tendon anchor force was applied at both ends of the tendons. The vertical tendon stresses (1341 MPa) were applied to the tendon element tails at the bottom of the model. The target stress for vertical tendons away from penetrations was the design stress. The target stress for vertical tendons with any path deviation caused by penetrations was reduced from the design stress by the angular friction loss encountered between the base of the PCCV wall (Elev. 0) and the base of the 3DCM model. This theoretical loss along portions outside the 3DCM model was performed by hand calculation.

After prestressing, pressure was applied to the model. The distribution of stress and strain in the hoop tendons of the 3DCM pretest model was shown in Chapter 2. By 3.0 Pd, strains in the hoop tendon adjacent to the hatches reached 1.4%, while strains elsewhere were generally between 0.006 and 0.010. At 3.5 Pd, peak strains exceeded 5%, which is enough to rupture a tendon. Thus, if model pressurization were not precluded by a liner failure/leakage, the 3DCM model predicts 3.5 Pd as a structural limit state. (Note that this is lower than that predicted by 2D (axisymmetric analysis alone.)

Important observations of the 3DCM model response and of comparisons to the LST follow.

1. The 3DCM model deforms radially outward significantly more than the test measurements and more than the axisymmetric analysis (as shown in Figures 2-17 and 2-18). (The 3DCM model exhibits on-set of global yielding at a lower pressure. Global yielding occurs over a broader range of pressure, and the post-yield behavior is softer than the axisymmetric model.)
2. At pressures lower than 3.0 Pd, the buttresses (90 and 270 degrees) actually displace radially more than most other azimuths. This trend reverses itself beyond 3.0 Pd, but at $P < 3.0$ Pd, the trend is clearly at odds with test observation.

3. As shown in Figures 6-3 through 6-6, while the 3DCM model provided a good simulation of the tendon stress distribution at the test's initial conditions, as pressure increased, different stress redistribution occurred in the tendons than was simulated by the analysis.

Addressing these three differences between the 3DCM model and the LST observations became the primary focus of the 3DCM posttest analysis work.

6.2 Analysis of Special Models to Derive 3DCM Buttress Springs

In looking for modeling assumptions that would cause the observed variances with the LST, the first observation was that the buttresses above and below the 3DCM model boundaries have meridional bending stiffness not represented in the analysis boundary conditions. A reasonably simple way to account for this would be to derive equivalent spring properties and then apply radial spring elements, as shown in Figure 6-2. The global axisymmetric models were used for this purpose, as shown in Figures 6-7 and 6-8.

The derivation was performed by adding a 2D plane stress representation of a buttress to the axisymmetric model. The model was then cut at the appropriate 3DCM model horizontal boundary. Zero rotation boundary conditions were applied at the cut boundary, and horizontal and vertical tendon prestress was maintained as in the full axisymmetric models. A horizontal displacement was then applied to the cut boundary, as shown in Figures 6-7 and 6-8. Separate models were analyzed with and without the buttress present and the force versus displacement results were plotted and differenced, as shown in the Figures 6-7 and 6-8. The difference results become the force versus deflection properties assigned to the buttress springs. The force versus deflection in Figure 6-7 shows a force plateau reached beyond displacement of about 1.3 mm (0.005 inches). The spring force-displacement curves were defined to large displacements.

The displacement results with this buttress spring change are plotted later in the chapter.

6.3 Posttest Tendon Modeling (and Intermediate Results)

The next and only other modeling assumption at significant variance with observed test behavior was the tendon modeling, especially the representation of friction. A lengthy study and series of analyses focused on this phenomenon. This chapter discusses and presents results for run numbers 4, 5, 6, 7, and 9 from that study.

The 3DCM tendon modeling was reviewed in detail and a first change was implemented based on the observation that from the tendon tangent points 5 degrees from the buttress edge to the tendon anchor point, the tendons were not previously tied to the concrete mesh (i.e., they were assumed frictionless). The situation is shown in Figure 6-9. The pretest modeling approach was consistent with the 1999 axisymmetric modeling assumption that straight tendon runs do not require friction modeling. Moreover, in the pretest work, this distance was short enough that direct tendon-to-concrete contact was not required. With hindsight from the test, however, it was observed that at higher pressures, the tendon nodes in this region passed through the concrete mesh, which, of course, cannot occur in the structure, except for small readjustments of the tendon location within the tendon duct.

Figure 6-9 shows the remedy. These straight segments were still assumed frictionless, but were simply tied to the concrete with perpendicular truss elements. Moving past several preliminary investigative analyses, the change depicted in Figure 6-9 was named 3DCM Model 4. 3DCM Model 5 simply added the previously described buttress springs. Results of Models 4 and 5 are provided in Figures 6-10 through 6-19. These figures show improvements over the pretest analysis, but still have significant differences from the test.

The focus of the posttest effort then returned to the tendon friction modeling methodology. Significant insights into the behavior of the tendons were provided by the tendon force (and strain) test measurements shown previously in Figures 6-3 to 6-6. The locations of these tendons on the 3DCM (H35, H53, H67, and H68) are shown in Figure 6-20. The symbols plotted on the tendon for the profile plots are a combination of the load cells (force) and wire strain gage (strain converted to force) measurements. The "Tensmeg" data was not used. The strain gage data was converted to force by first converting the strain gage measurements to axial strain (according to formulae described in [6] which account for the pitch of the individual wires in the tendon strands), then converting to stress using average tendon stress-strain data,

and finally multiplying by the nominal area of the tendon, 3.393 cm² (0.525 in²), to get force. These calculations were prepared by SNL.

Tendon H35 shows good agreement with initial analytical stress distributions, but most of the data for H35 is at the tendon ends. Tendons H53, H67, and H68, which have some good data interior from the ends, again show good agreement with initial stress distribution, but significant differences as pressurization builds. This tends to validate the initial approach to tendon friction modeling. (Note that in the tendon modeling approach the correct stress distribution is achieved by only applying stress at the anchorage; no initial stress is applied interior to the ends of the tendon).

Two important observations can be made about the hoop tendon behavior as pressure increases.

1. When pressure reaches the pressure to overcome prestress, $P = 0.59$ MPa (see discussion in [1] for the pressure calculation), tendon stress distributions begin to change from the classical angular friction design assumption to an approximately uniform distribution. This change occurs between approximately 1.5 Pd and 2.5 Pd; then the stress distributions stay fairly uniform at most higher pressures.
2. The apparent strain increases in the tendons corresponding to the force/strain gage readings are significantly larger (e.g. 0.48% versus 0.36% for H53) than the strain that corresponds purely to radial expansion. This can only be explained by force redistribution associated with sliding. Thus, the position of the tendon relative to the concrete must be allowed to change after initial prestress in order to adequately simulate tendon behavior during overpressurization.

These observations led to some extensive changes and studies of the tendon friction modeling. It was understood throughout the project that tendon friction may be quite complex, and that it may even dynamically change with pressure, but the tools to model such behavior were limited. The analysis strategies that were investigated were chosen to, at the very least, bracket the observed LST behavior. The analyses presented herein are as follows.

Model 6. (Shown in Figure 6-21). Apply prestress. Then, by using the ABAQUS *MODEL CHANGE capability, fix the tendon nodes at their initially deformed position relative to the concrete. In other words, start from classical design prestress with friction and then grout (bond) the tendons.

Model 7. (Shown in Figure 6-22). Based on observation 1 (above), perform run 5 (the run with only buttress springs added) up to $P = 1.5$ Pd (0.59 MPa), then model change all friction elements to non-friction elements (truss ties aligned perpendicular to the tendons). In other words, at $P = 1.5$ Pd, perfectly unbond the tendons.

Model 9. (Shown in Figure 6-23). Try a case with some aspects of run 6 and 7. After prestress, keep the initial friction elements, but add a new set of friction elements in the reverse orientation so that if points on the tendon move in the reverse direction from that of initial prestress, they will experience reverse direction friction in the process.

To simplify the friction study, anchor set losses were approximated more simply than in the pretest analysis. The same anchor set azimuth was used as before, but the friction was removed along the anchor set zone, so that tendon stress became constant over the anchor set zone. The initial tendon stress profile for all three runs (6, 7, and 9) are shown in Figures 6-24, 6-25, and 6-26, respectively. This approximation was deemed reasonable to study the more global effects of varying friction treatment along the remaining path of the tendons.

6.4 Posttest Results and Comparisons

The results of the different tendon friction bounding cases are plotted in Figures 6-27 through 6-54. Figures 6-38 to 6-54 demonstrate the effects on tendon stress in the different tendon friction simulations.

Considering run 6 with essentially bonded tendons (Figures 6-27 to 6-30), the "free-field" azimuth (135 and 180 degrees) agree well with the axisymmetric analysis and the test behavior, while the radial displacement of the E/H is overpredicted. The buttress radial displacement is also more in line with the test.

Considering run 7 with essentially unbonded tendons (after $P = 1.5 P_d$), the E/H displacement prediction is very good, but the 180 degrees and other nearby azimuths are significantly overpredicted.

Run 9 with two-direction friction behaves closer to run 6, the bonded case, but here the tendons are not bonded – their sliding just meets friction resistance in either direction. Although the E/H radial displacement is still somewhat overpredicted, run 9 is the best representation of tendon friction possible without resorting to a contact-surface type of tendon-to-concrete friction simulation.

6.5 Conclusions on 3DCM Analysis and Tendon Behavior

The posttest 3DCM models provide a bracketed simulation of the tendon friction behavior and the radial displacement patterns that occurred in the test. The comparisons that help form conclusions on tendon modeling and behavior are the replotting of the tendon stress distributions shown in Figures 6-3 through 6-6 for the posttest analysis. This is done in Figures 6-46 through 6-56. Runs 6, 7, and 9 are shown for each case. The following summarizes the additional observations provided by these figures.

The effects of friction are most clearly shown for the H35 tendon, which sweeps around all of the penetrations. Run 6 shows the most pronounced friction effects, run 9 shows a little less, and run 7 shows uniform distribution after $1.5 P_d$.

In general, the tendon friction simulation runs 6, 7, and 9 show progressively better agreement with test measurements, with run 9 showing quite good agreement at the anchors and at most points interior to the tendon ends. (Consider tendon H68, for example, Figure 6-56. At $3.0 P_d$, the analysis force distribution passes almost directly through the test data points. Note that the top curve is for $3.5 P_d$ – it would be reasonable to roughly interpolate between $3.0 P_d$ and $3.5 P_d$ to estimate the $3.3 P_d$ curve.)

Based on these and the other observations in this chapter, the results of run 9 are used to drive the M/S (and estimated F/W) penetrations posttest analysis.

Finally, in regards to tendon friction behavior, the test measurements and analytical evidence support the conclusion that tendon friction is important to the tendon behavior, but traditional friction design formulas that predict tendon stress distribution begin to break down once pressurization exceeds the pressure that overcomes prestress (in this case, roughly $1.5 P_d$). Some parts of the tendon are forced to slide relative to the duct in the reverse direction of travel from that during prestressing. Under this action, angular friction properties probably still hold, but the direction of friction forces are opposite to the direction of travel. The best calculation methods recommended to account for this are, in descending order of preference, 1) an advanced contact friction surface between the tendons and the concrete (not manageable for the current problem size and complexity); 2) preset friction ties applied in one direction during prestressing and added in the other direction during pressurization (3DCM Model 9); and 3) if neither of these methods are practical within the scope of the calculation, start with an average stress level (using a friction loss design formula), but assume uniform stress distribution in the tendons throughout pressurization, i.e., an unbonded tendon assumption, and finally 4) same as 3, but using a bonded tendon assumption. For method 4, however, this can lead to a premature prediction of tendon rupture, because the tendon strain increments during pressurization will match the hoop strain increments of the vessel wall one-to-one, and this was not observed during the PCCV LST.

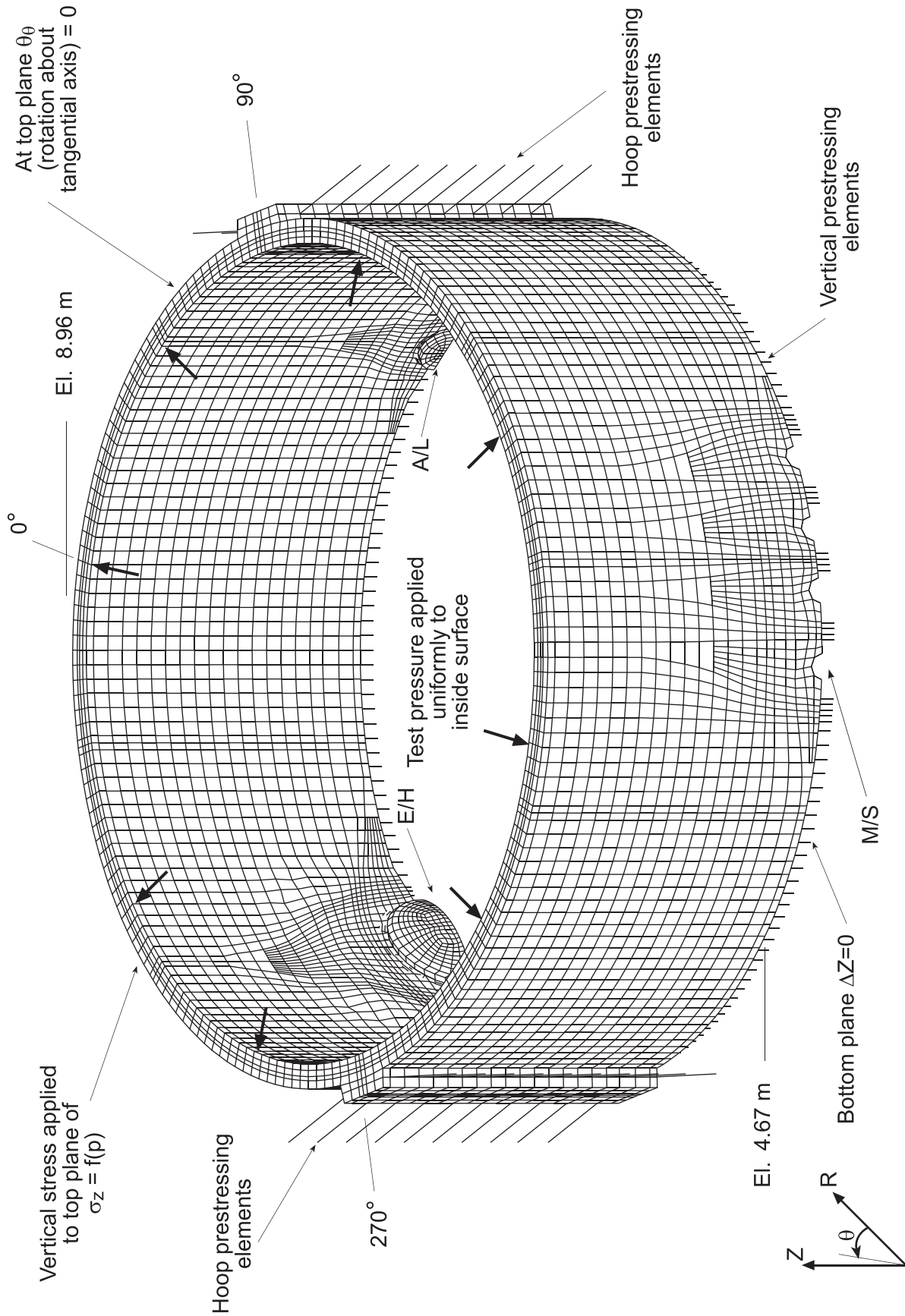


Figure 6-1. 3DCM Model Vertical Boundary Conditions

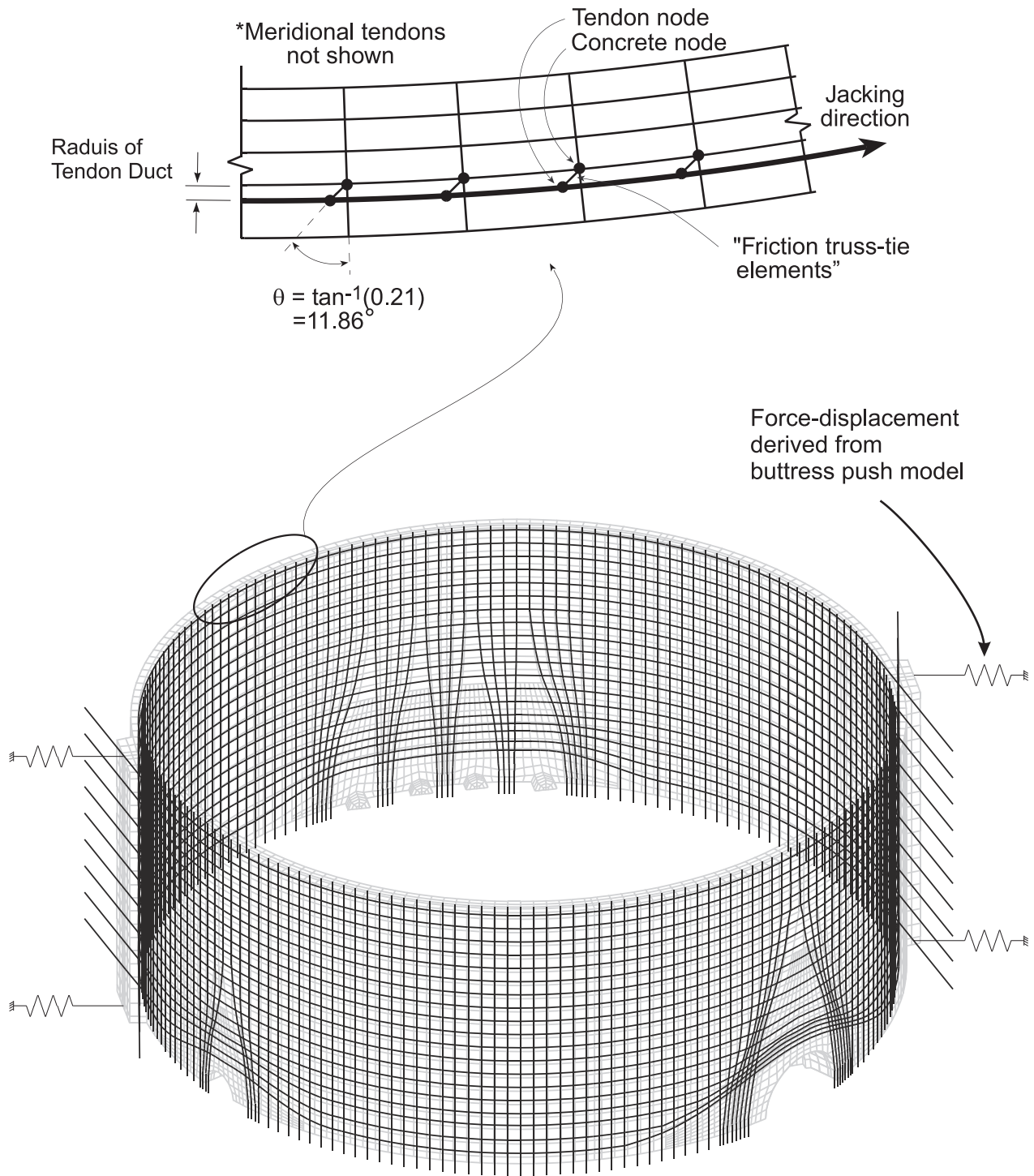


Figure 6-2. Isometric View of 3DCM Tendon Modeling and Added Buttress Springs

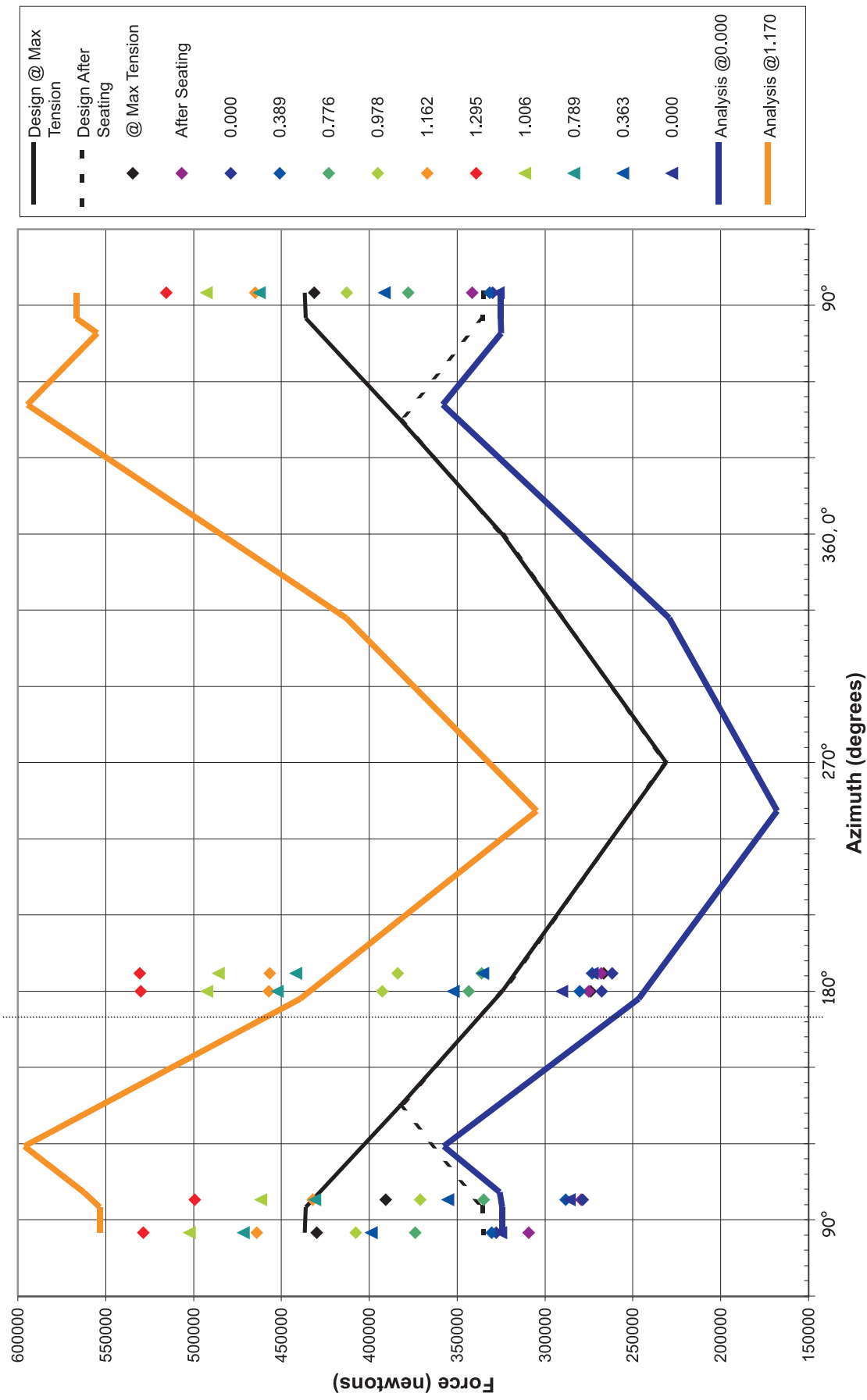


Figure 6-3. H35 Tendon Force Comparisons to Pretest

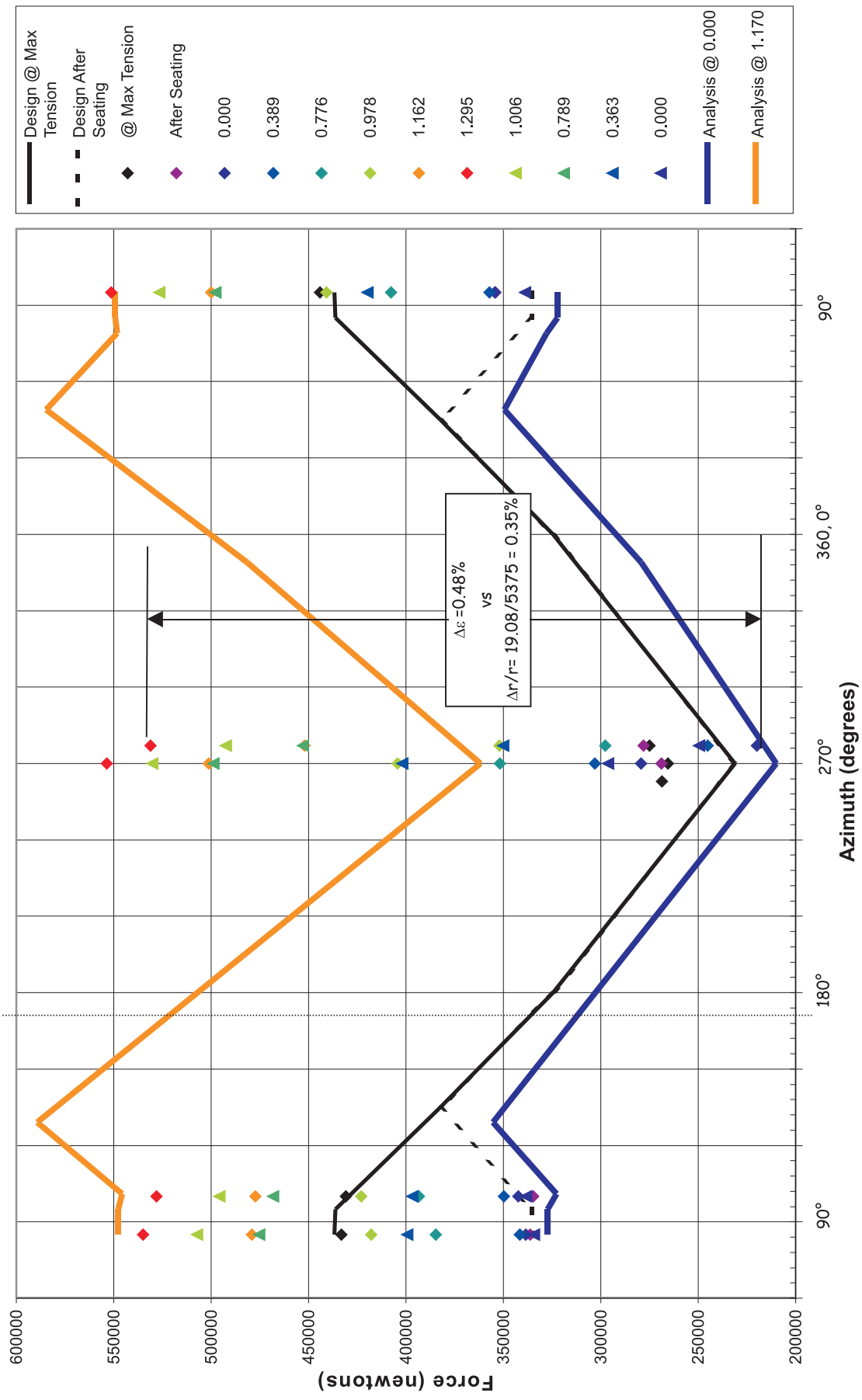


Figure 6-4. H53 Tendon Force Comparisons to Pretest

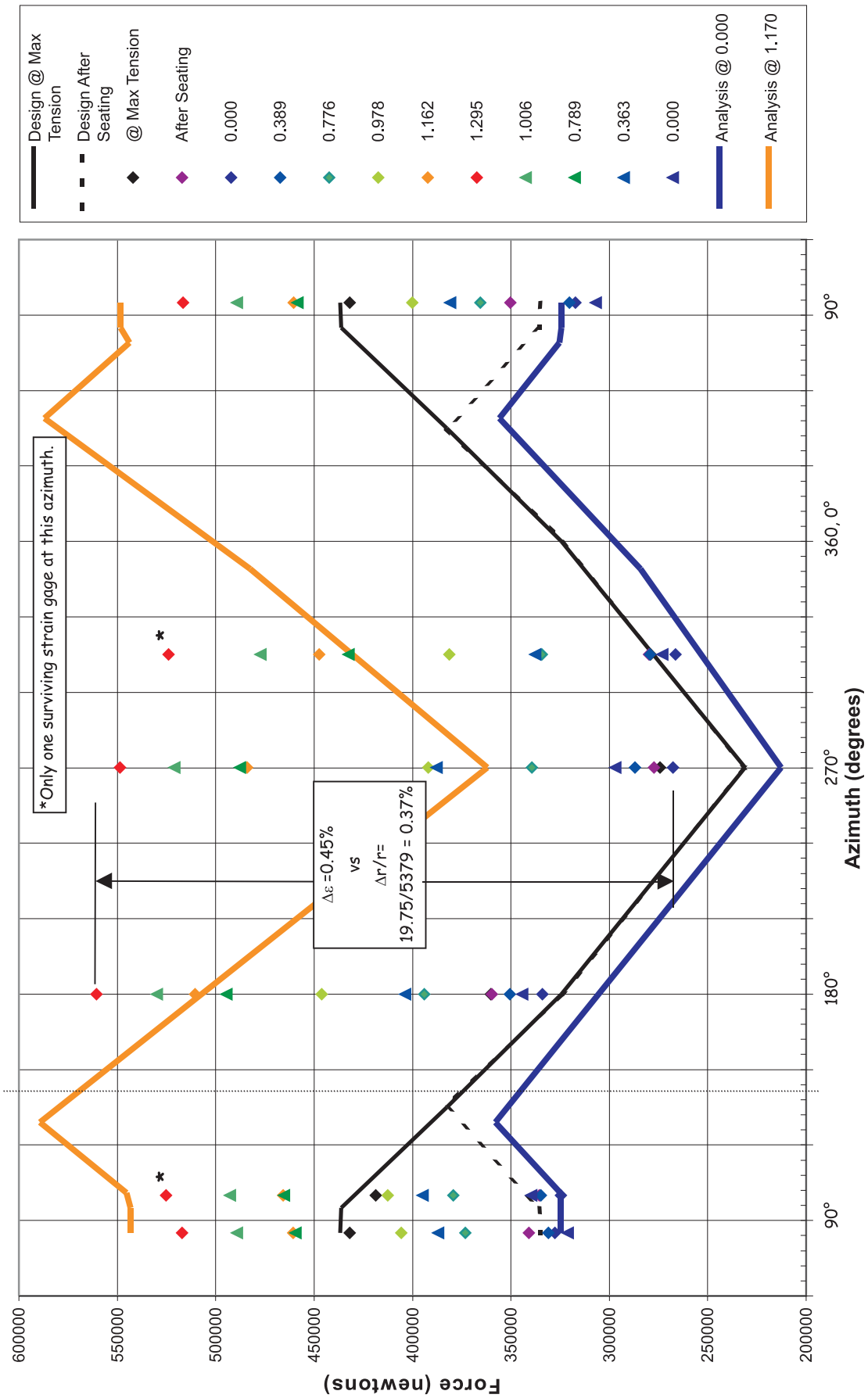


Figure 6-5. H67 Tendon Force Comparisons to Pretest

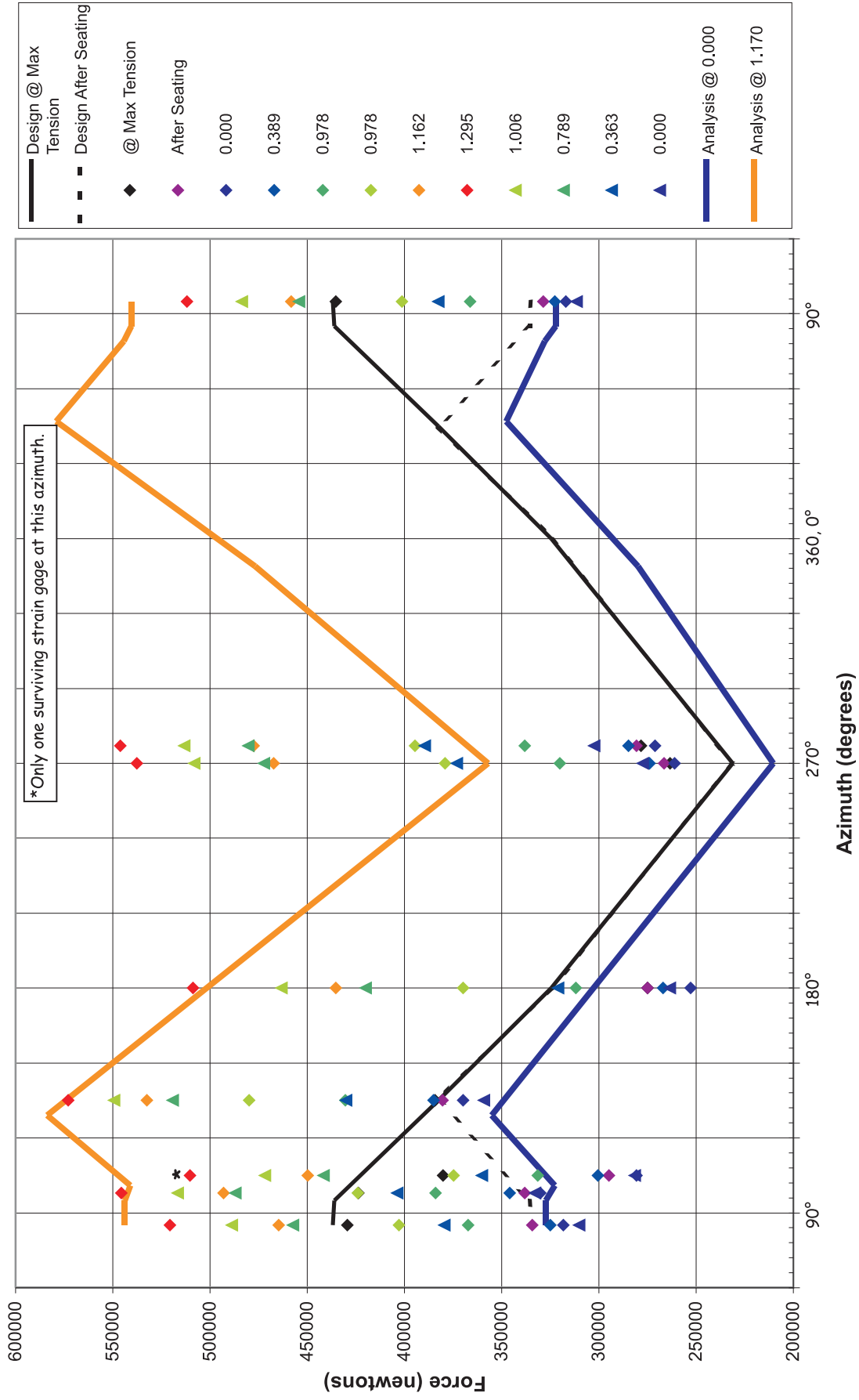


Figure 6-6. H68 Tendon Force Comparisons to Pretest

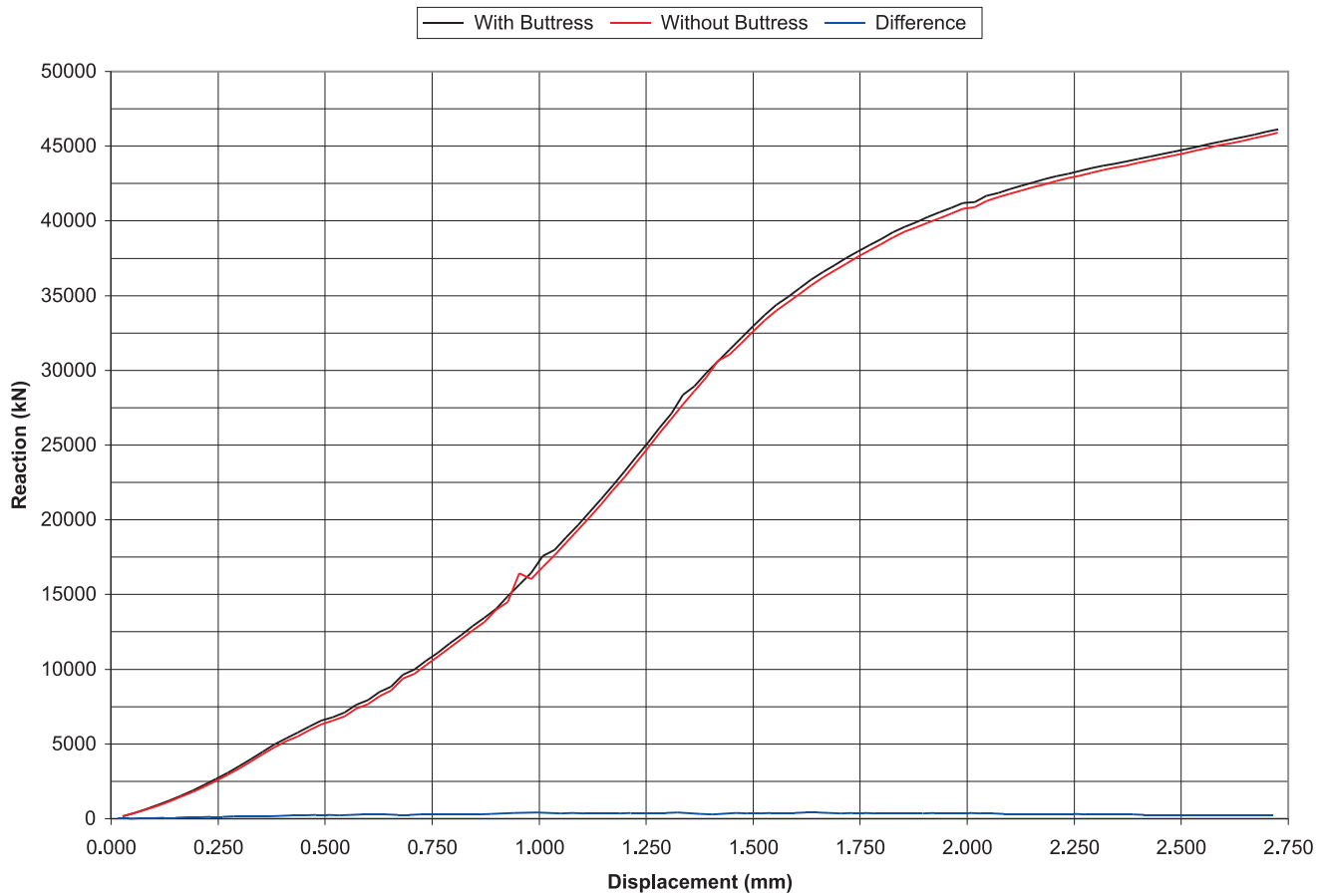
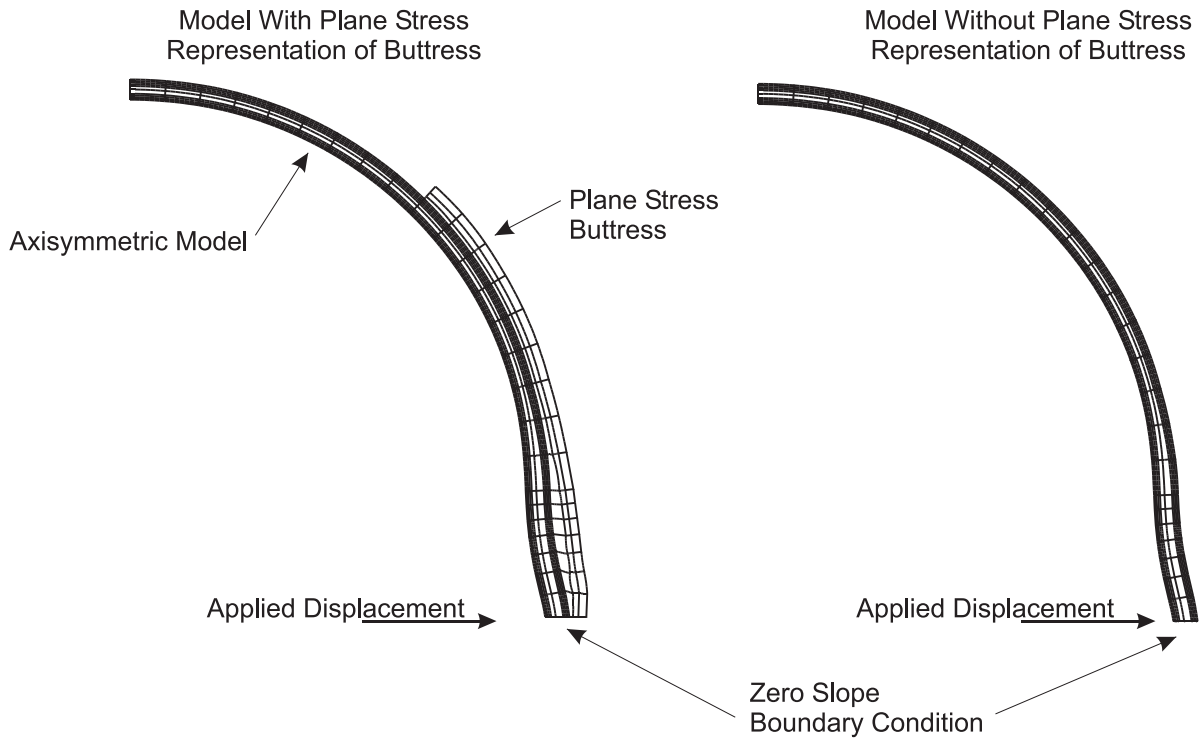


Figure 6-7. Definition of Upper 3DCM Buttress Radial Spring Properties by Axisymmetric Analysis

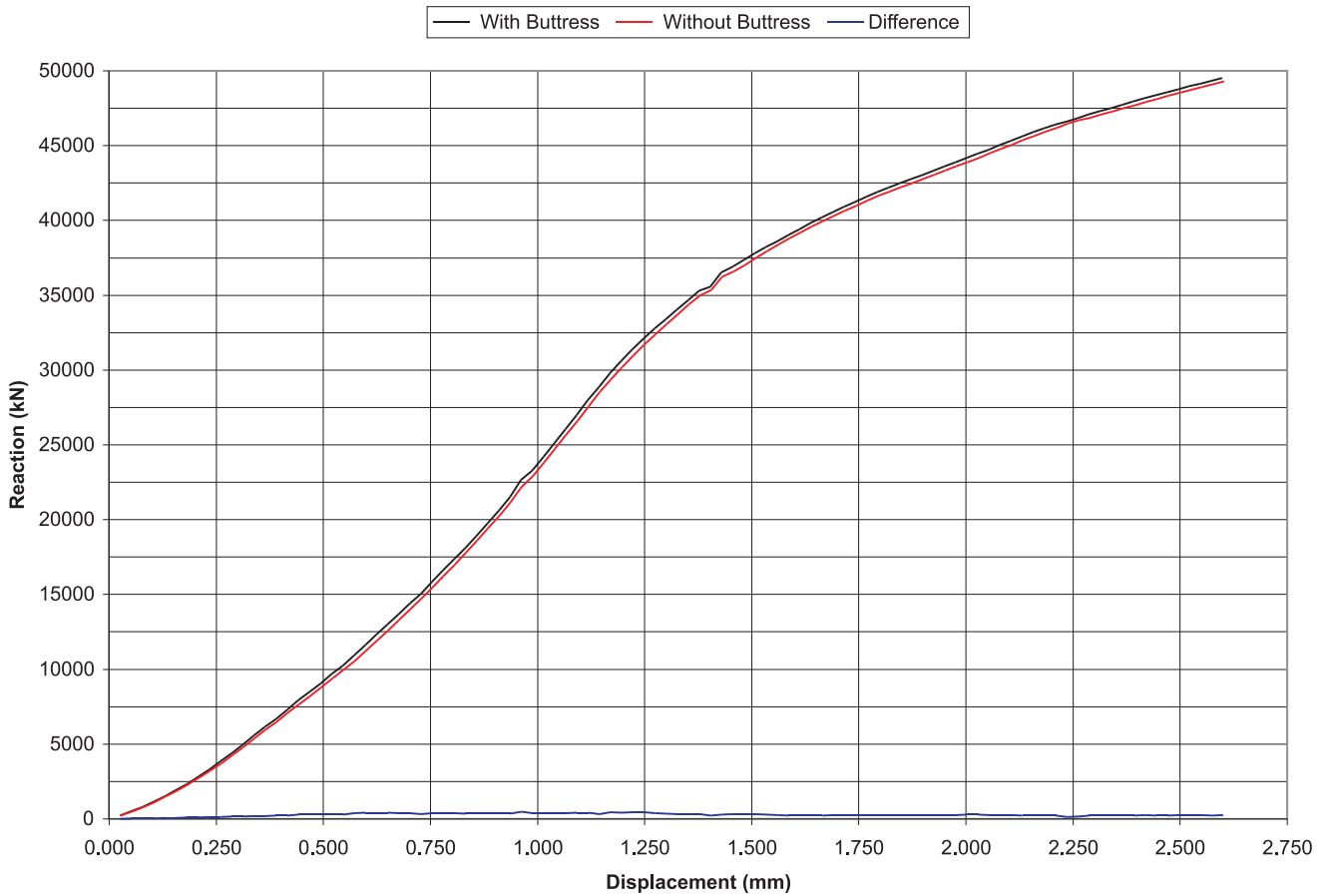
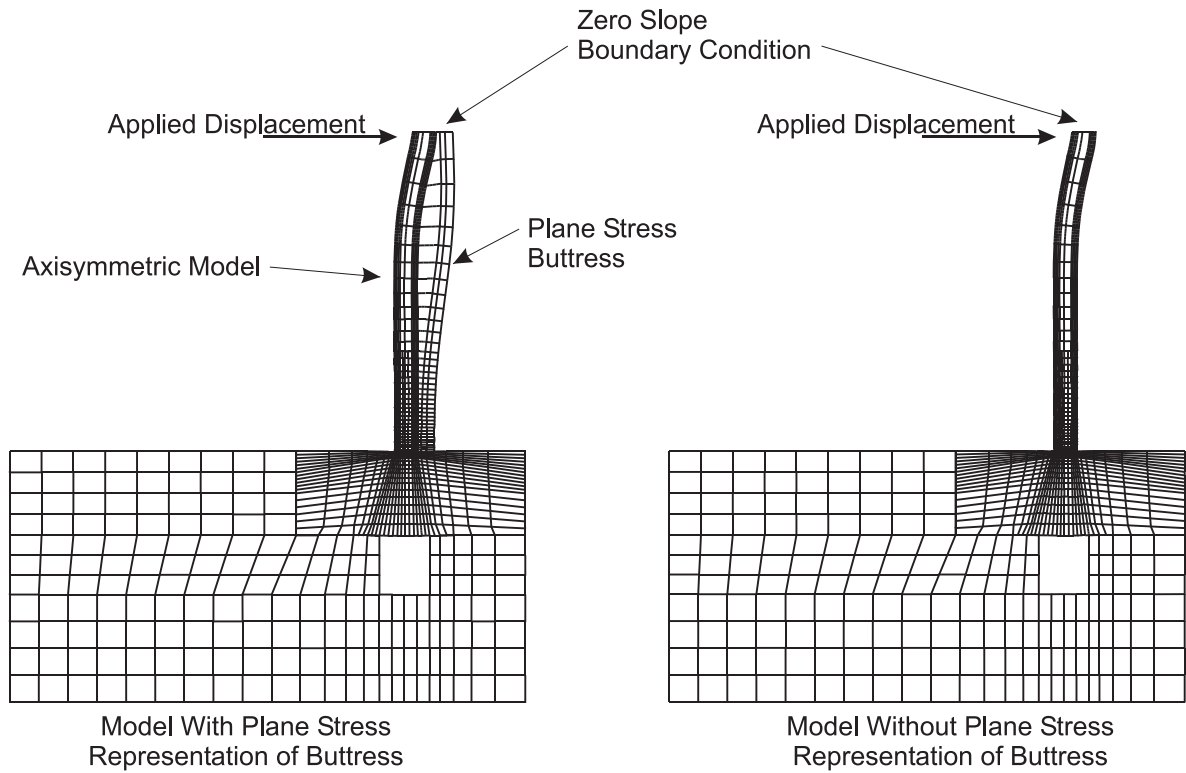


Figure 6-8. Definition of Lower 3DCM Buttress Radial Spring Properties by Axisymmetric Analysis

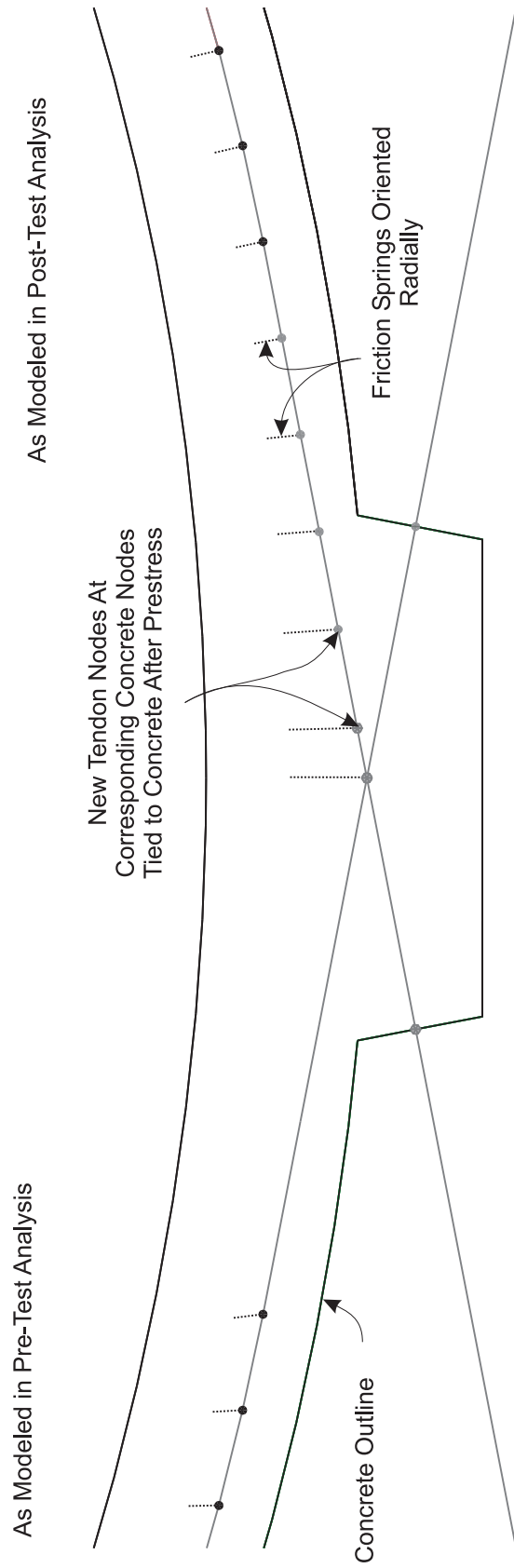


Figure 6-9. Addition of Tendon Ties in Straight Run of Tendons Between Tangent Points and Anchorages

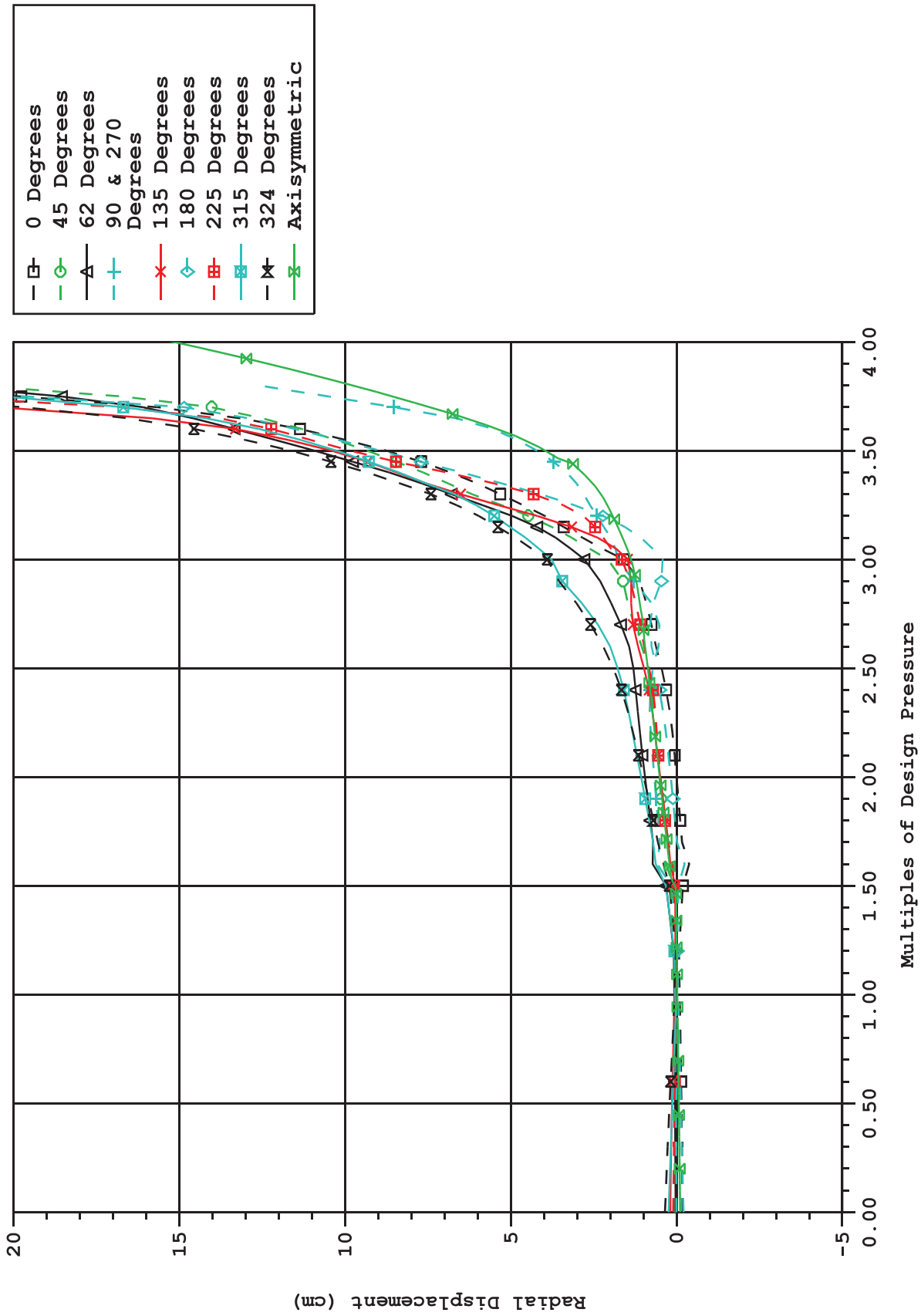


Figure 6-10. Radial Displacement at Elevation 4.7M, 3DCM Run 4 Compared to Axisymmetric

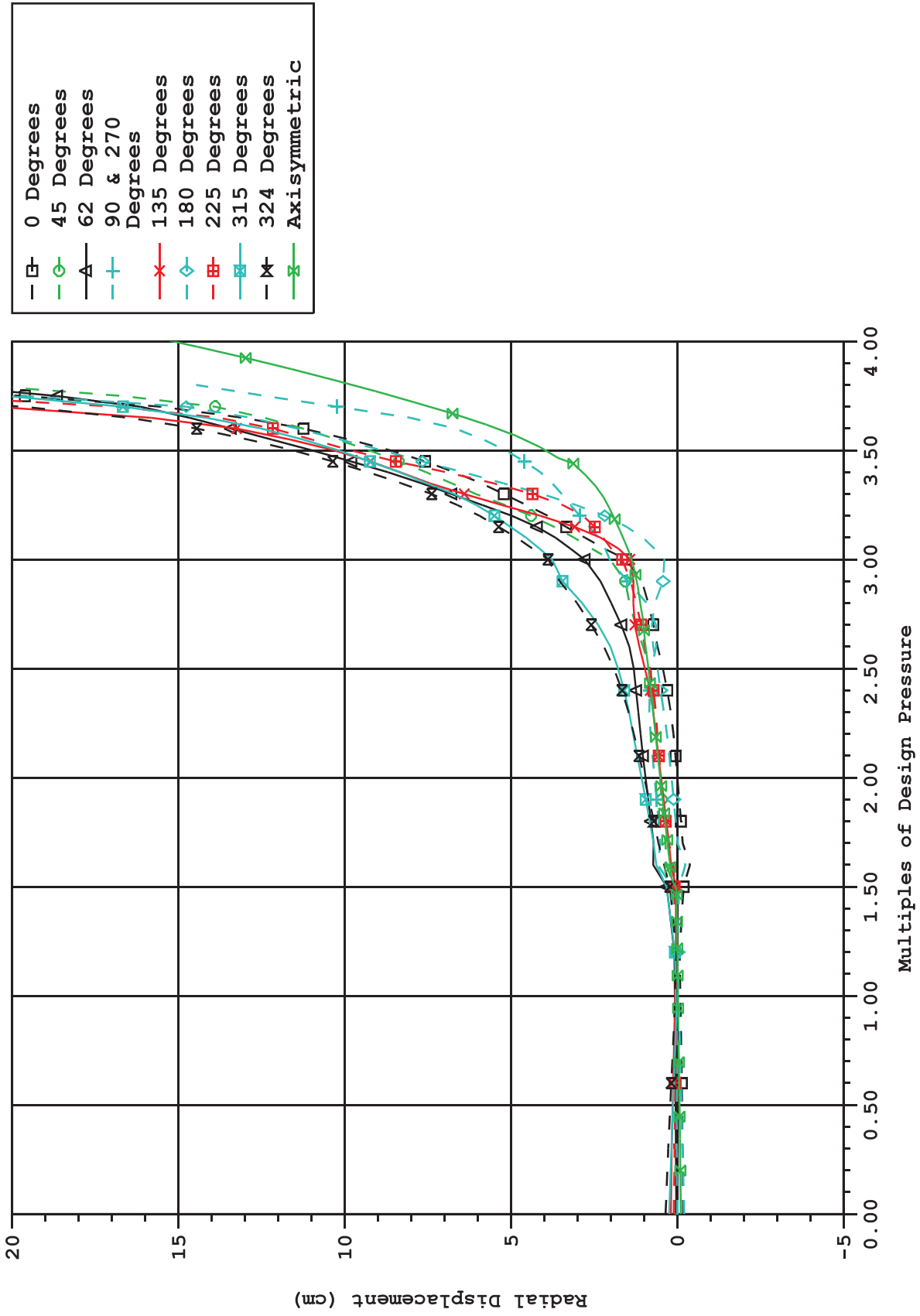


Figure 6-11. Radial Displacement at Elevation 4.7M, 3DCM Run 5 Compared to Axisymmetric

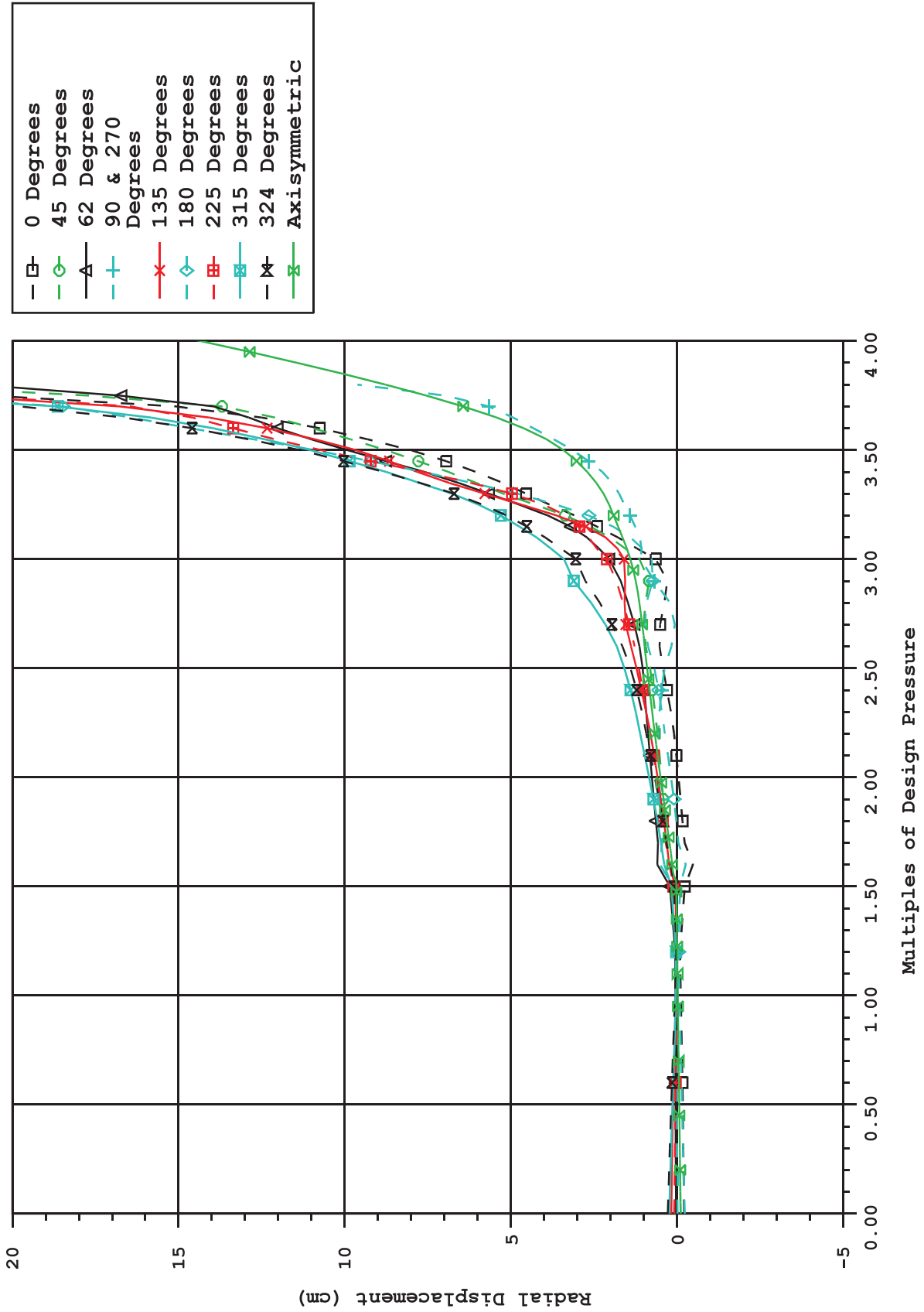


Figure 6-12. Radial Displacement at Elevation 8.9M, 3DCM Run 4 Compared to Axisymmetric

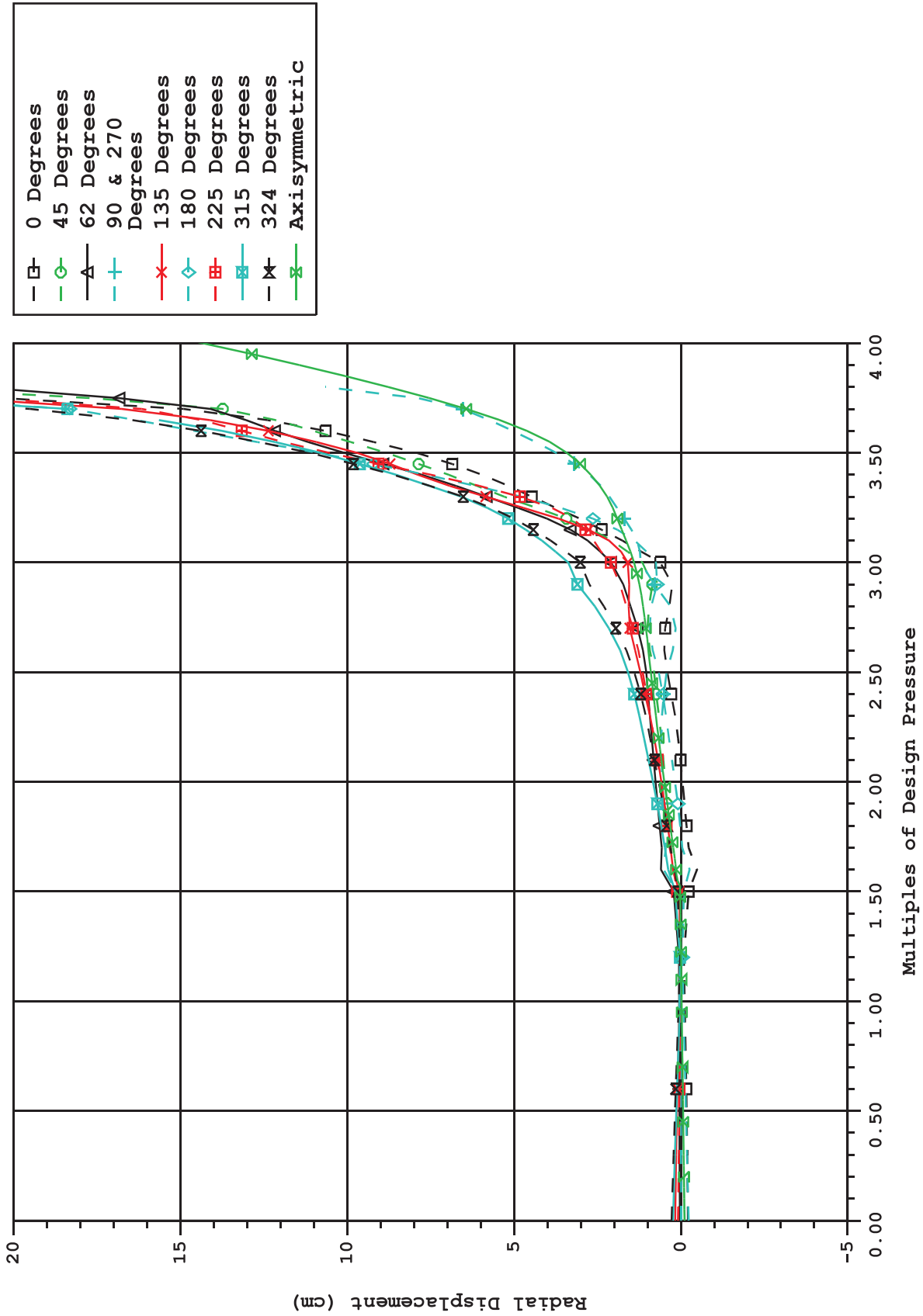


Figure 6-13. Radial Displacement at Elevation 8.9M, 3DCM Run 5 Compared to Axisymmetric

Standard Output Location Comparison

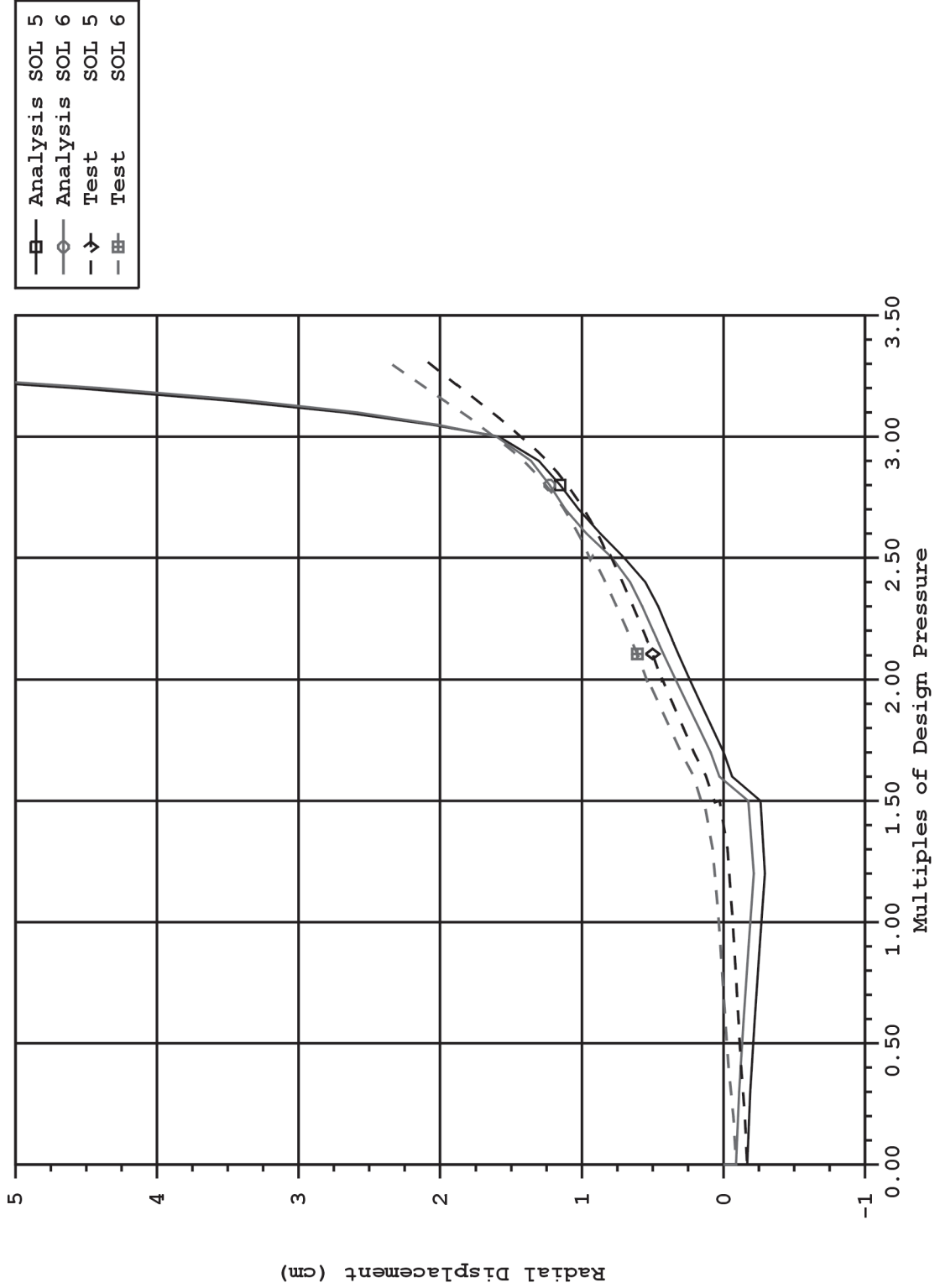


Figure 6-14. Comparison of Run 4 SOL 5 and 6 (Radial Displacement at 135 Degrees, 4.7M, 6.2M)

Standard Output Location Comparison

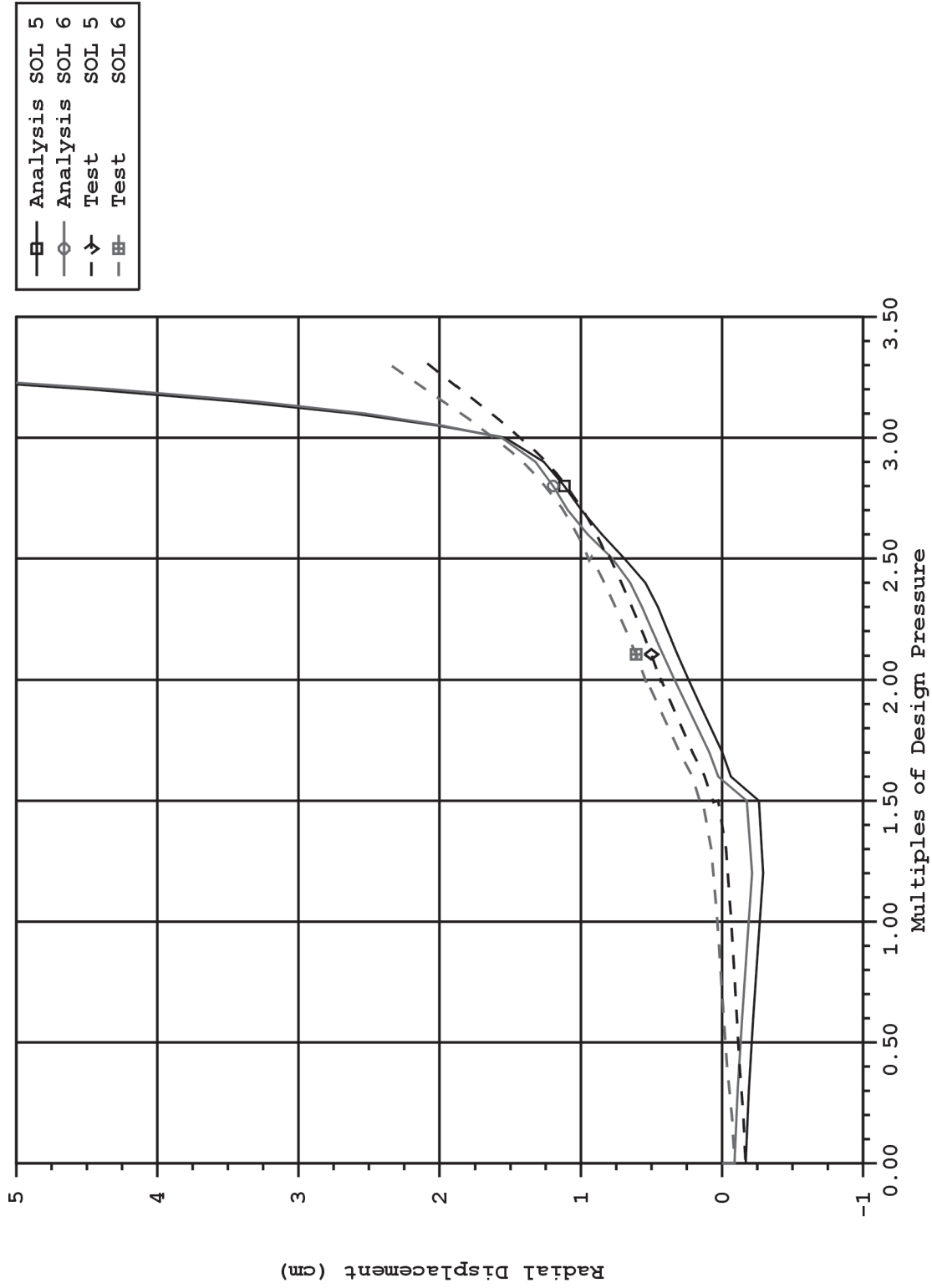


Figure 6-15. Comparison of Run 5 SOL 5 and 6 (Radial Displacement at 135 Degrees, 4.7M, 6.2M)

Standard Output Location Comparison

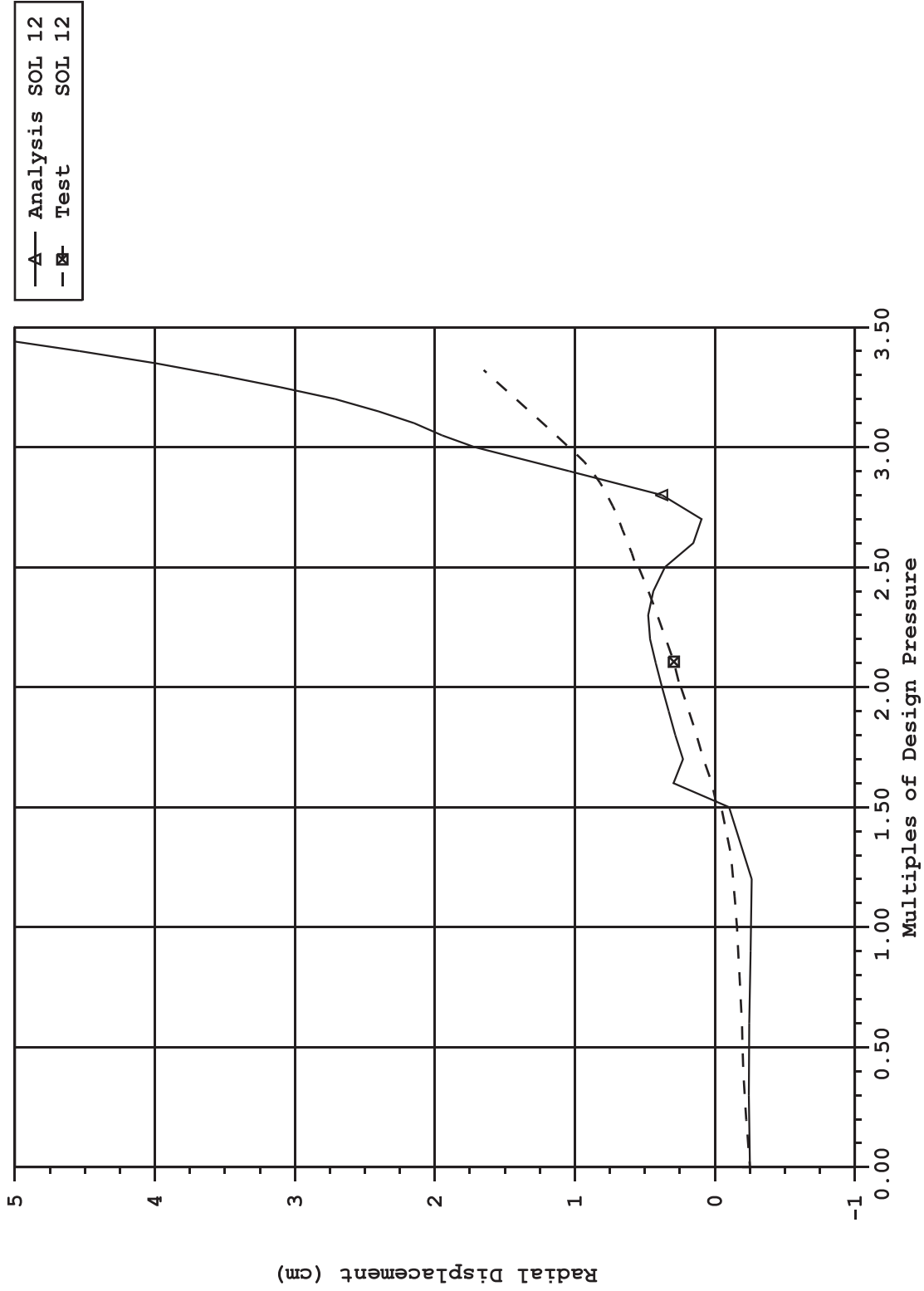


Figure 6-16. Comparison of Run 4 SOL 12 (Radial Displacement at 90 Degrees Buttress, 6.2M)

Standard Output Location Comparison

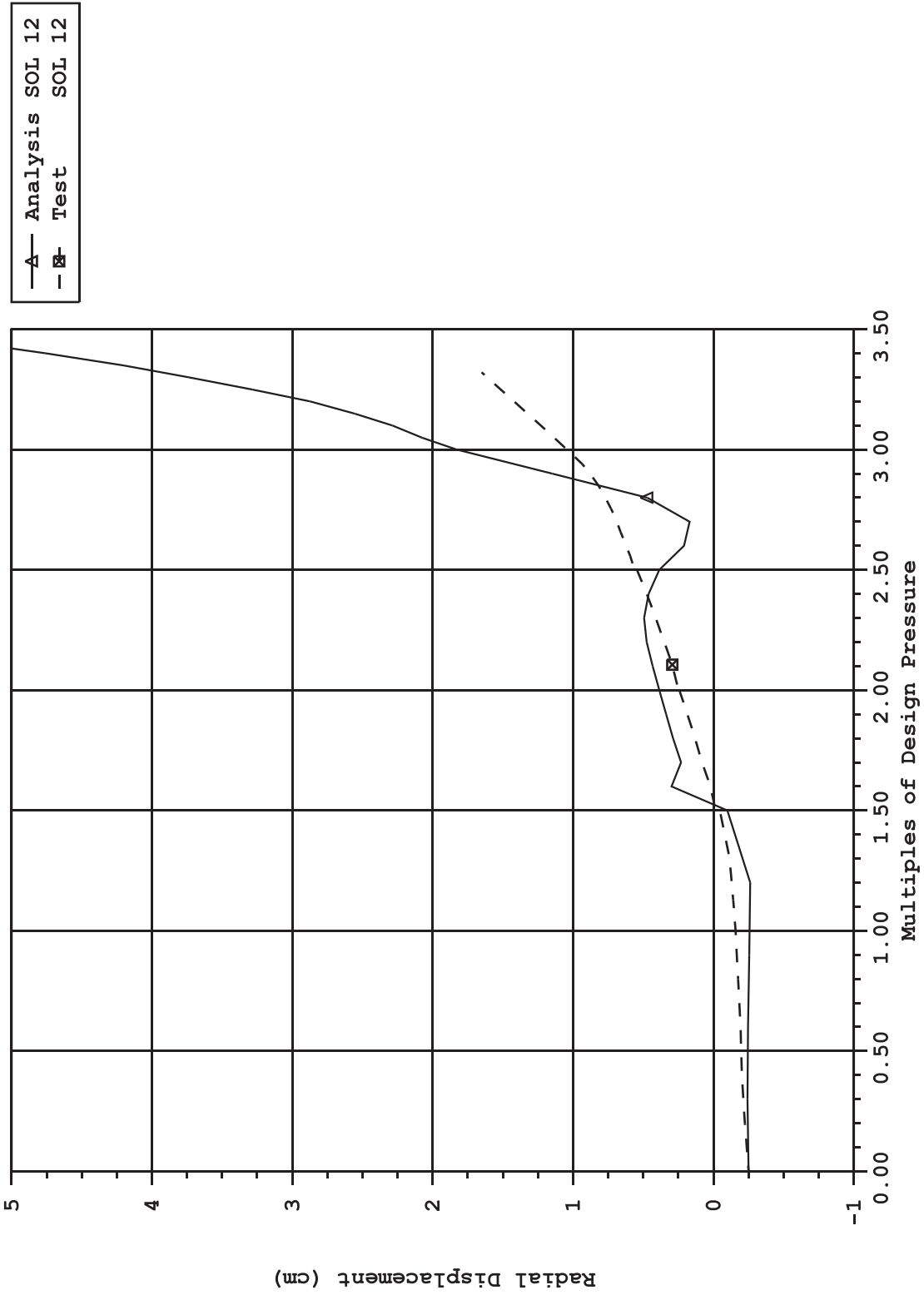


Figure 6-17. Comparison of Run 5 SOL 12 (Radial Displacement at 90 Degrees Buttress, 6.2M)

Standard Output Location Comparison

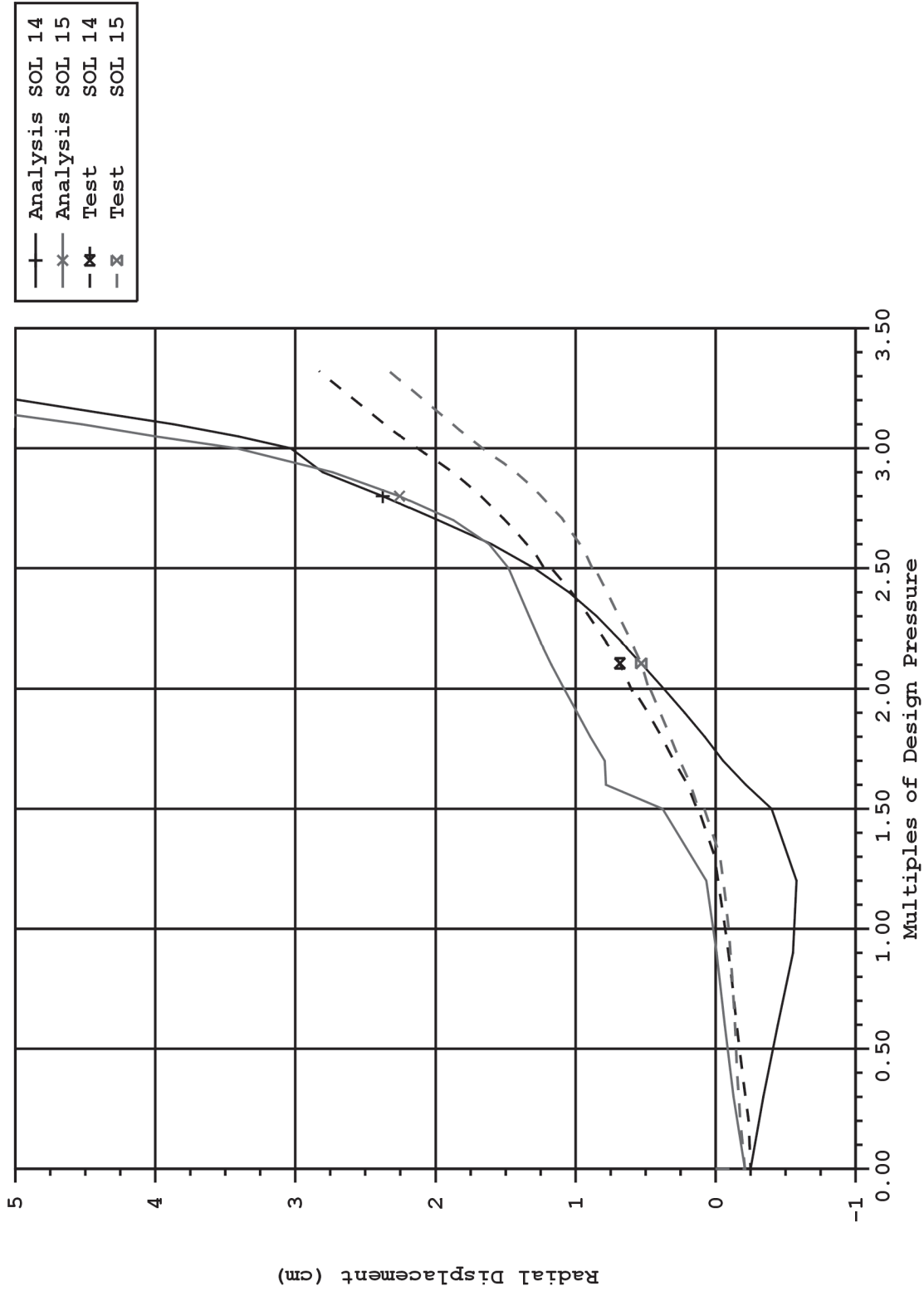


Figure 6-18. Comparison of Run 4 SOL 14 and 15 (Radial Displacement at E/H and A/L)

Standard Output Location Comparison

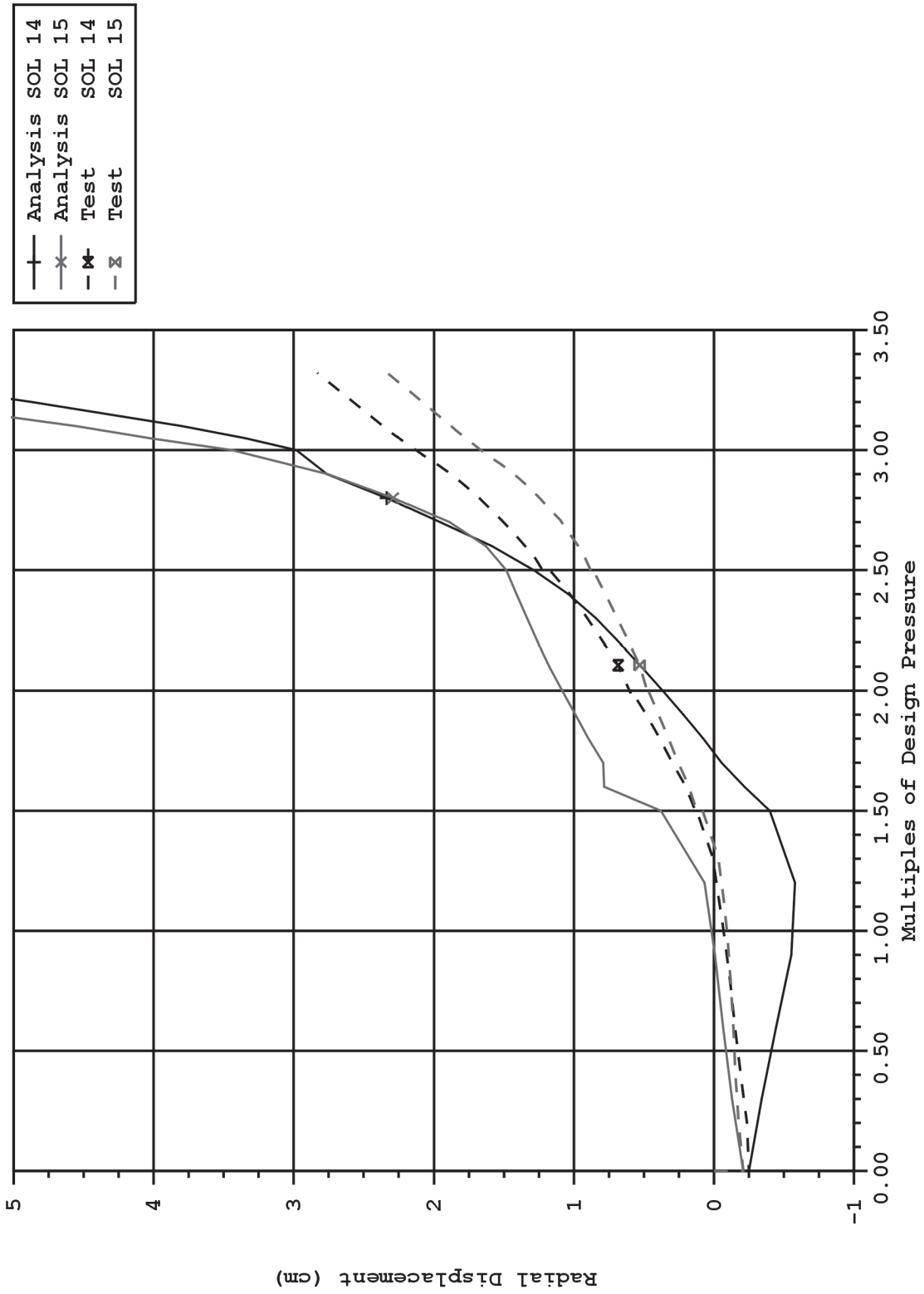


Figure 6-19. Comparison of Run 5 SOL 14 and 15 (Radial Displacement at E/H and A/L)

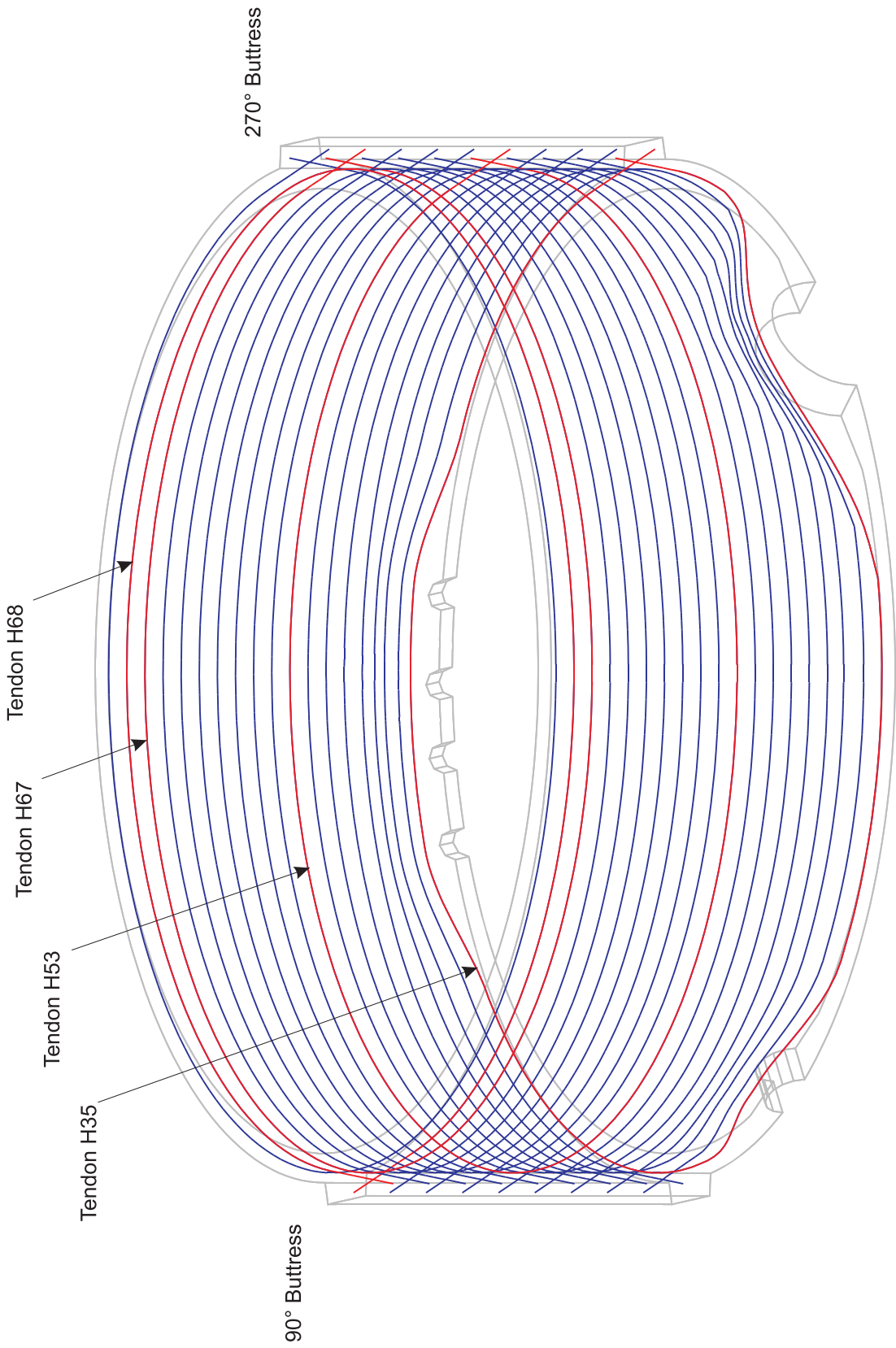
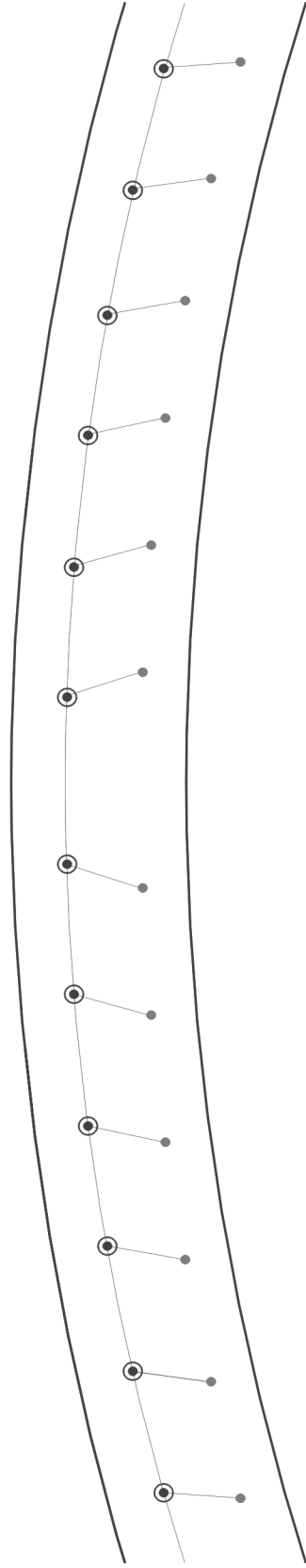


Figure 6-20. Location of Instrumented Tendons H35, H53, H67, and H68

○ Concrete Node
 ● Tendon Node
 ● Friction Node

Step 1. Apply Post-Tensioning with Original Friction Element Modeling



Step 2. After Post-Tensioning Lock-in Post-Tension effects.

- Remove Friction Elements
- Numerically Constrain Tendon Nodes to Concrete Nodes in Deformed Position

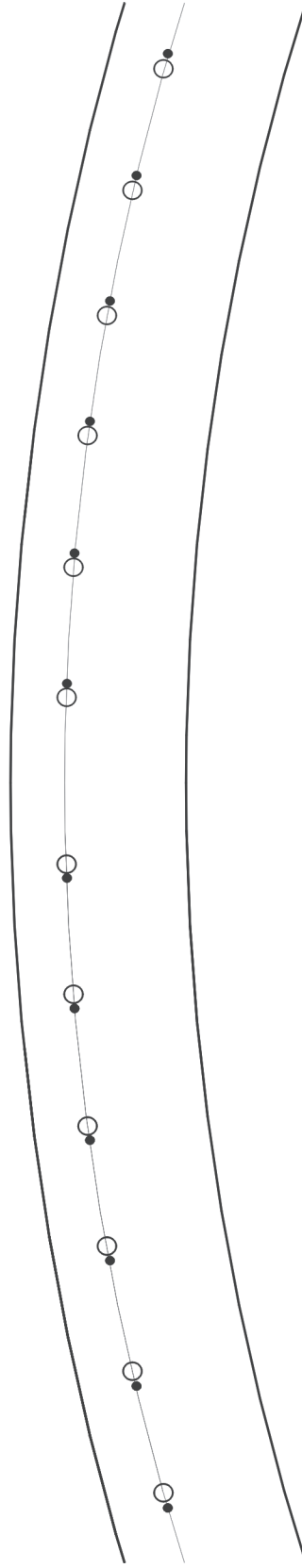


Figure 6-21. Tendon Friction Modeling Schematic for Run 6

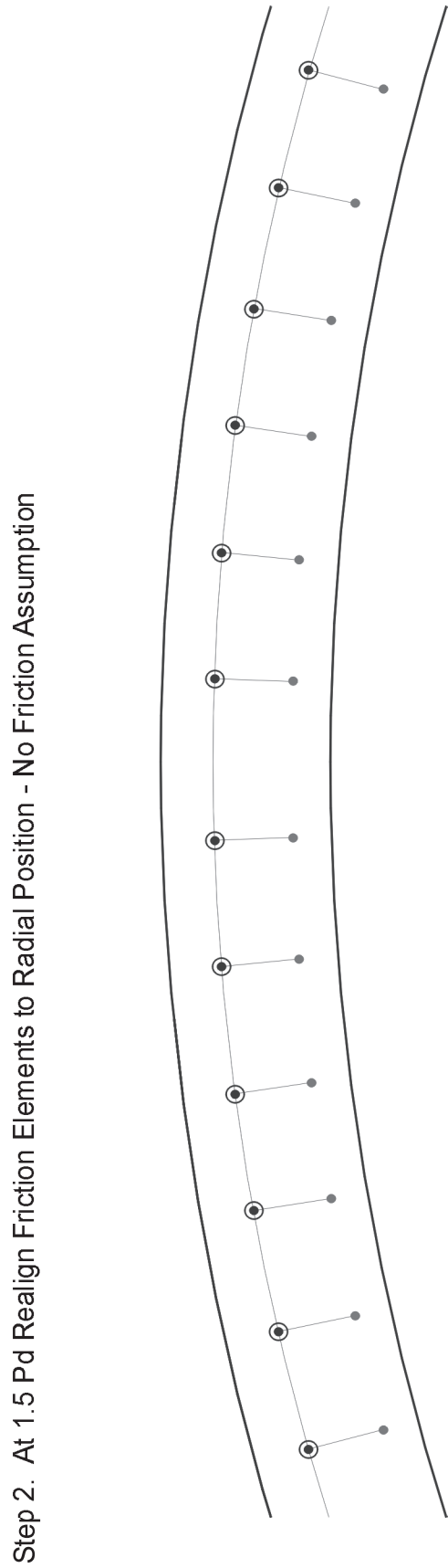
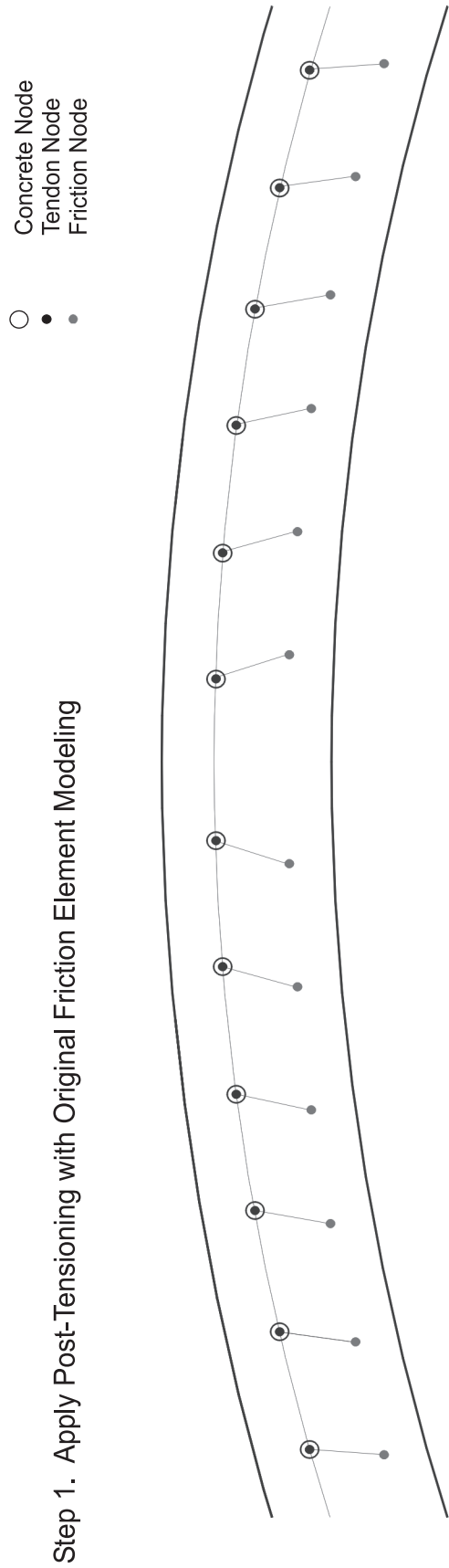
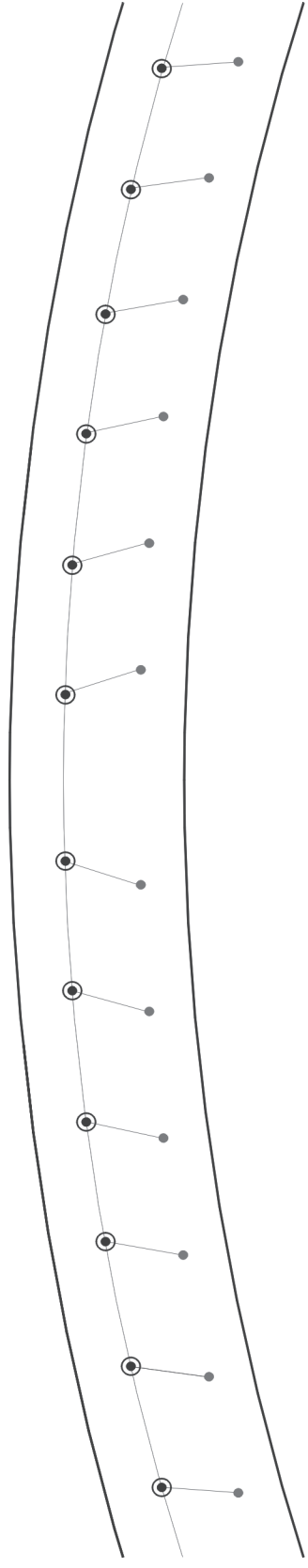


Figure 6-22. Tendon Friction Modeling Schematic for Run 7

○ Concrete Node
 ● Tendon Node
 ● Friction Node

Step 1. Apply Post-Tensioning with Original Friction Element Modeling



Step 2. After Post-Tensioning Add Second Series of Friction Elements Strain Free with Opposite Orientation

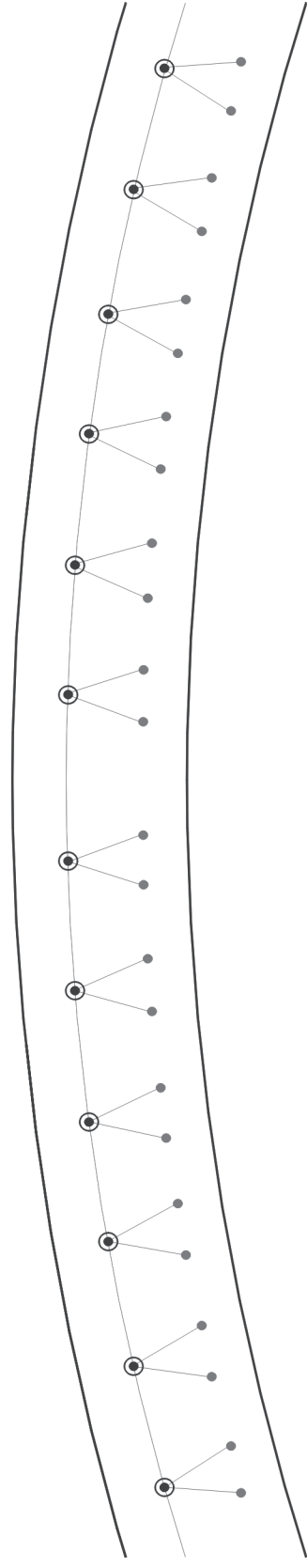


Figure 6-23. Tendon Friction Modeling Schematic for Run 9

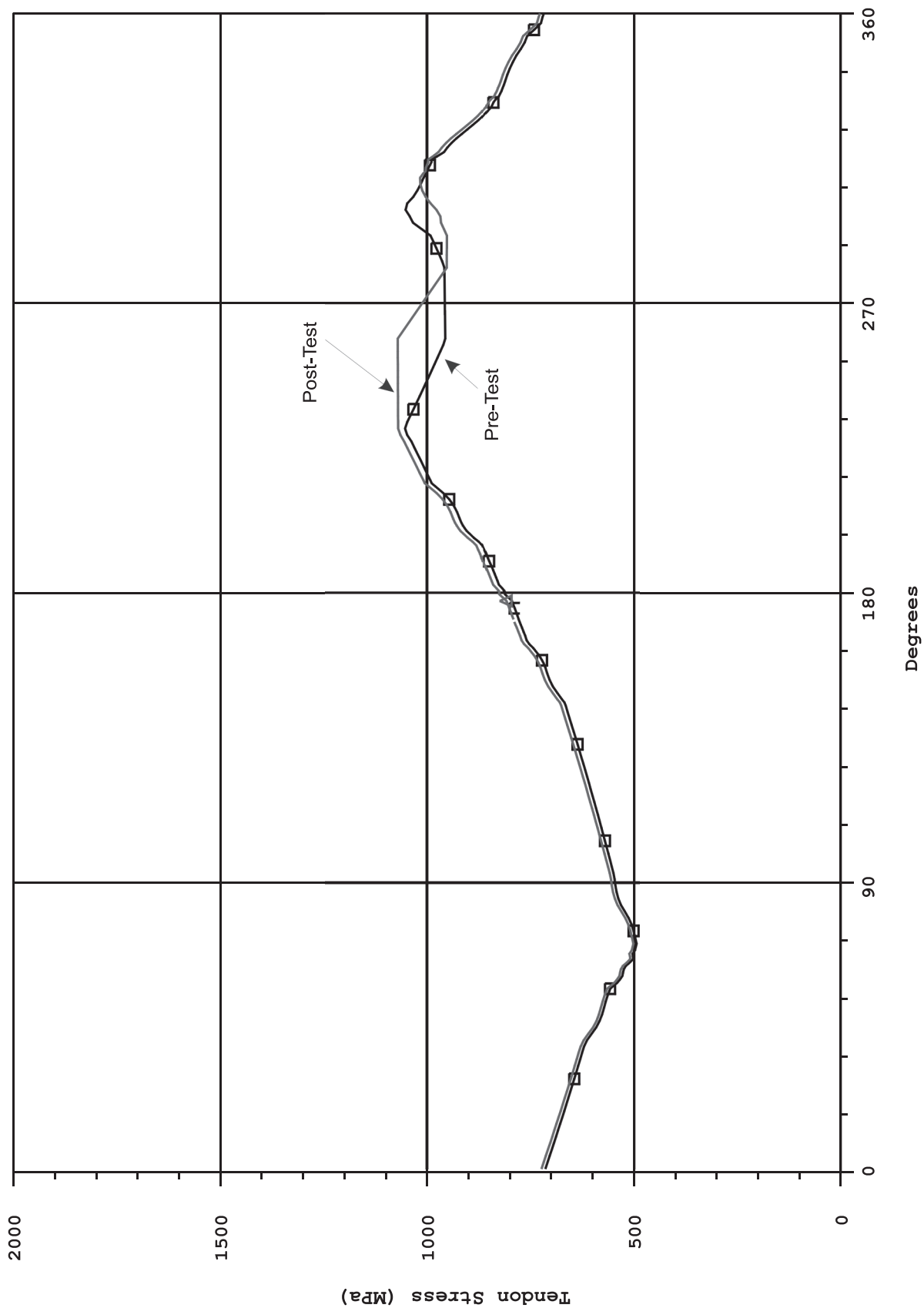


Figure 6-24. Changes to Anchor Set Prestress for Posttest 3DCM Study, Tendon H35

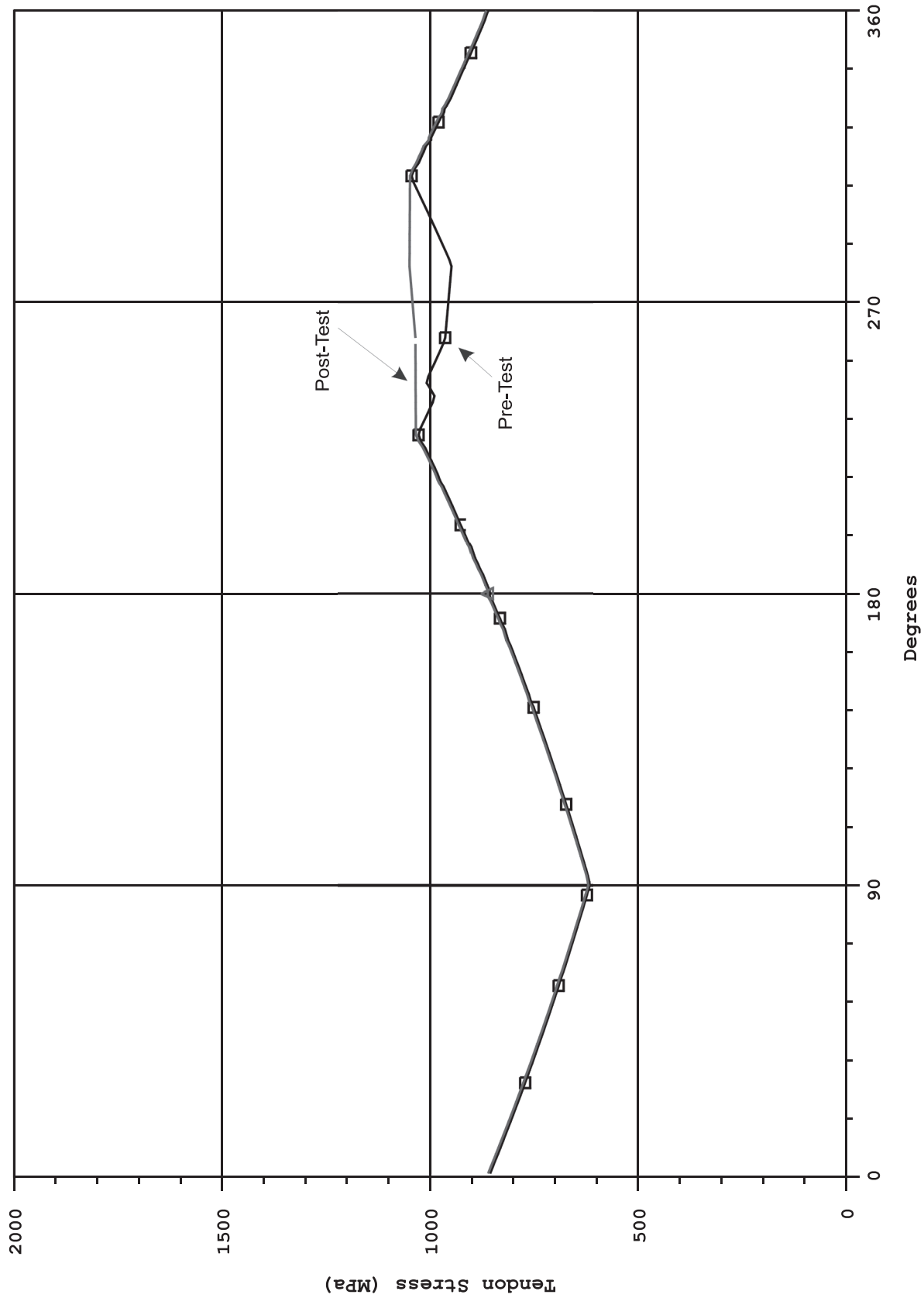


Figure 6-25. Changes to Anchor Set Prestress for Posttest 3DCM Study, Tendon H53

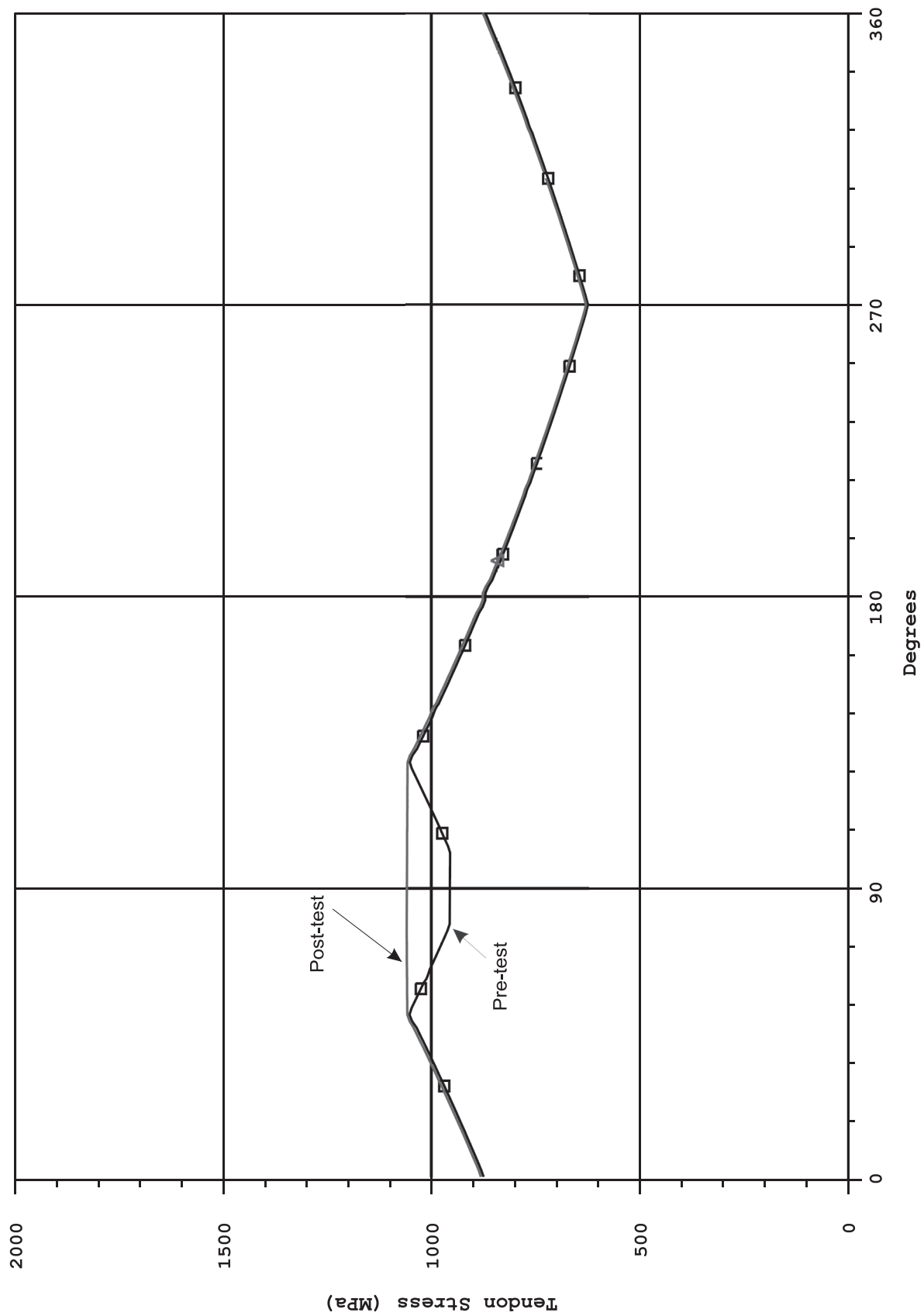


Figure 6-26. Changes to Anchor Set Prestress for Posttest 3DCM Study, Tendon H68

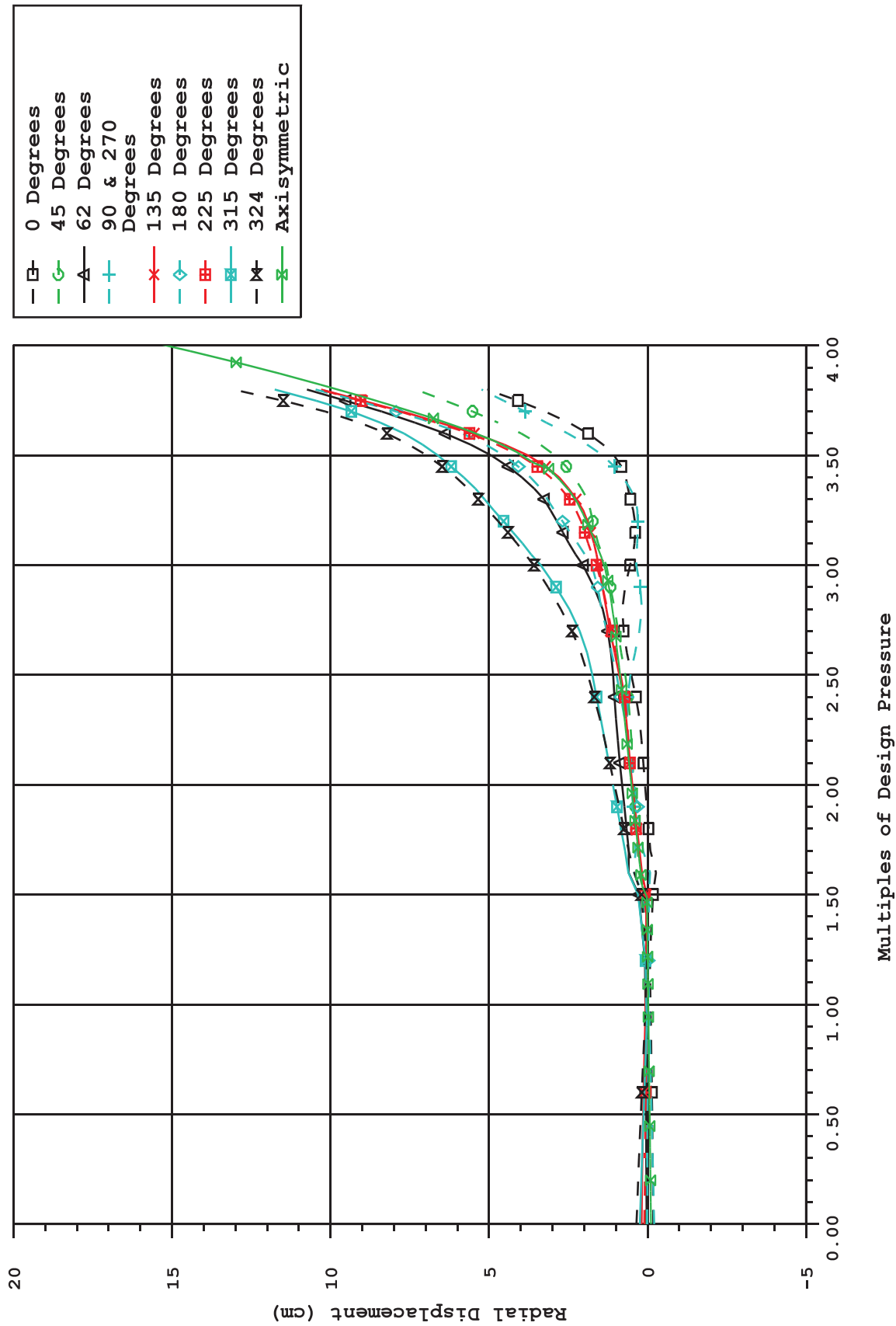


Figure 6-27. Radial Displacement at Elev. 4.7M, Posttest 3DCM Run 6
(Tendons "Bonded" After Prestressing) Compared to Axisymmetric

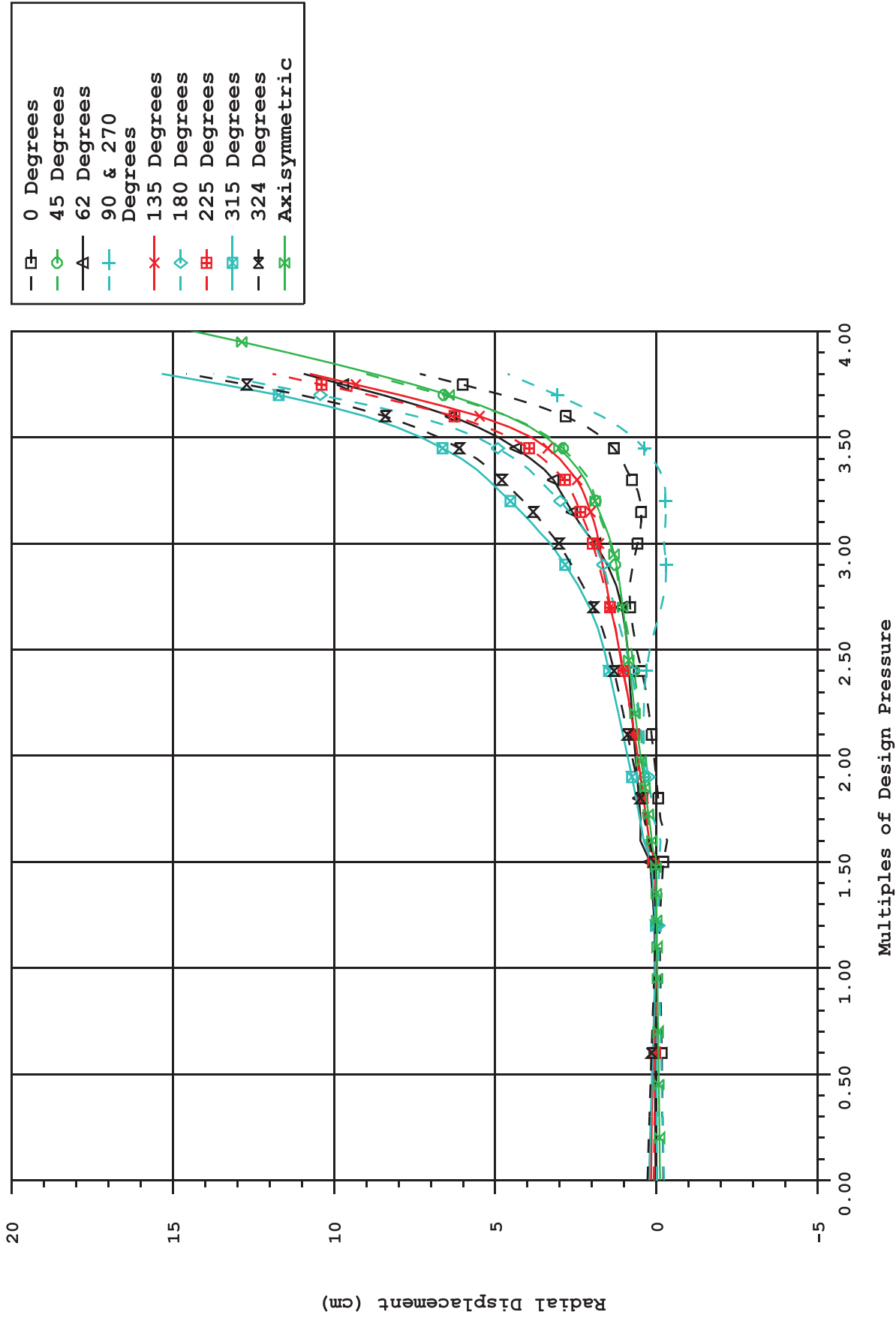


Figure 6-28. Radial Displacement at Elev. 6.2M, Posttest 3DCM Run 6 Compared to Axisymmetric

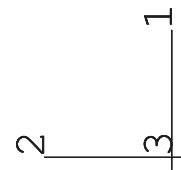
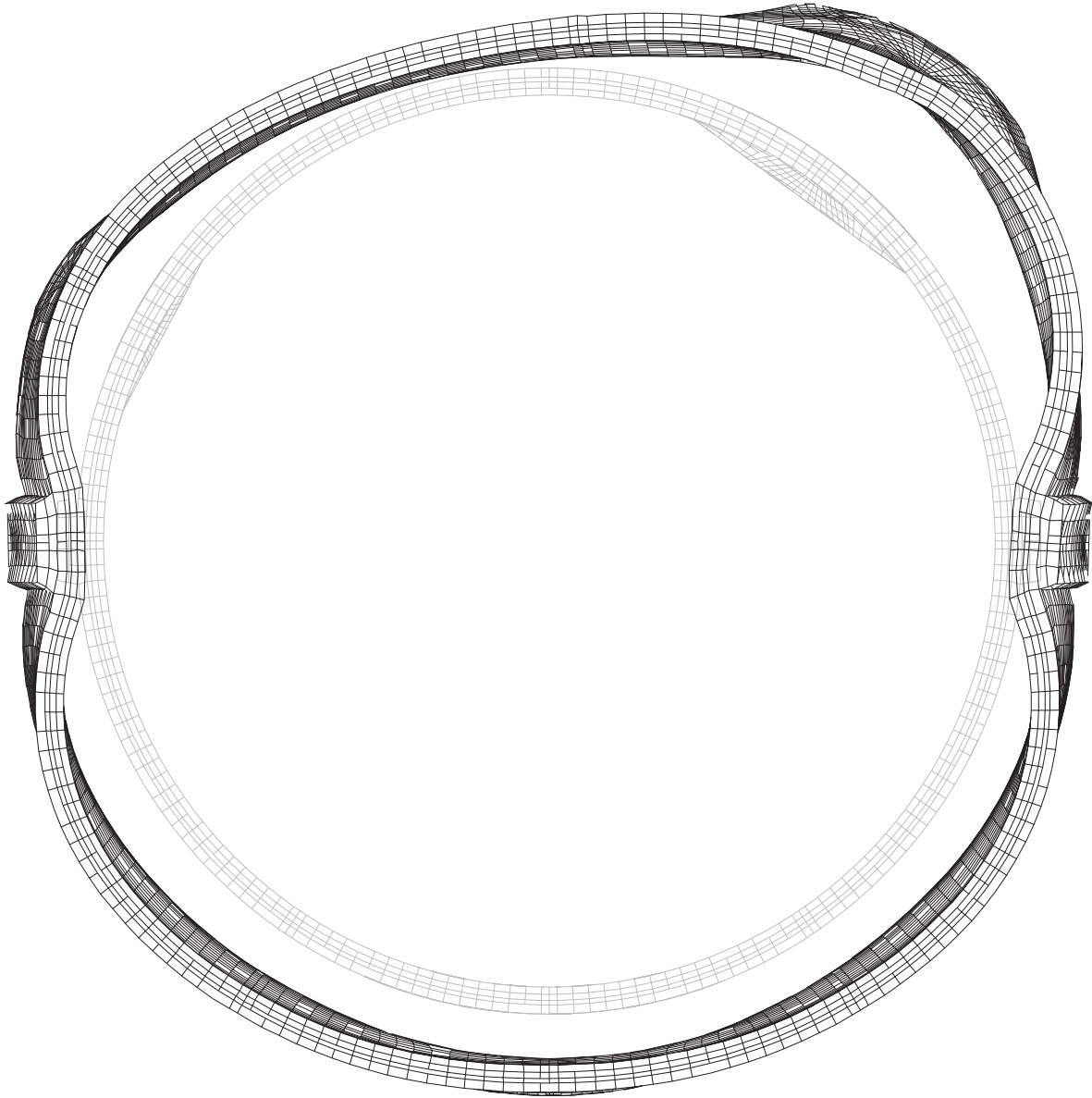


Figure 6-29. 3DCM Posttest Deformed Shape at $P = 2.5Pd$, Run 6 (mag. Factor = 100 \times)

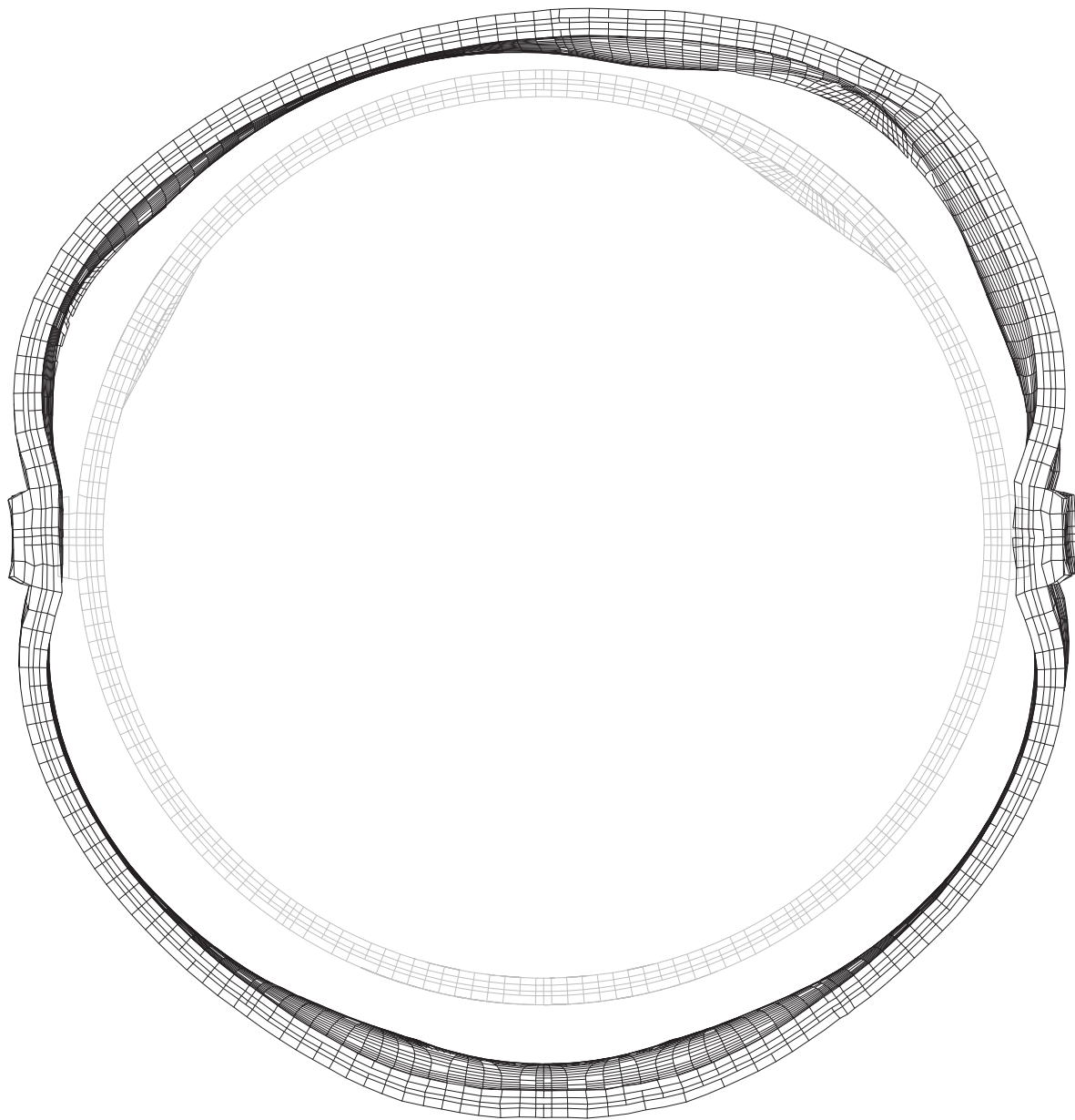


Figure 6-30. 3DCM Posttest Deformed Shape at $P = 3.8P_d$, Run 6 (mag. Factor = $10\times$)

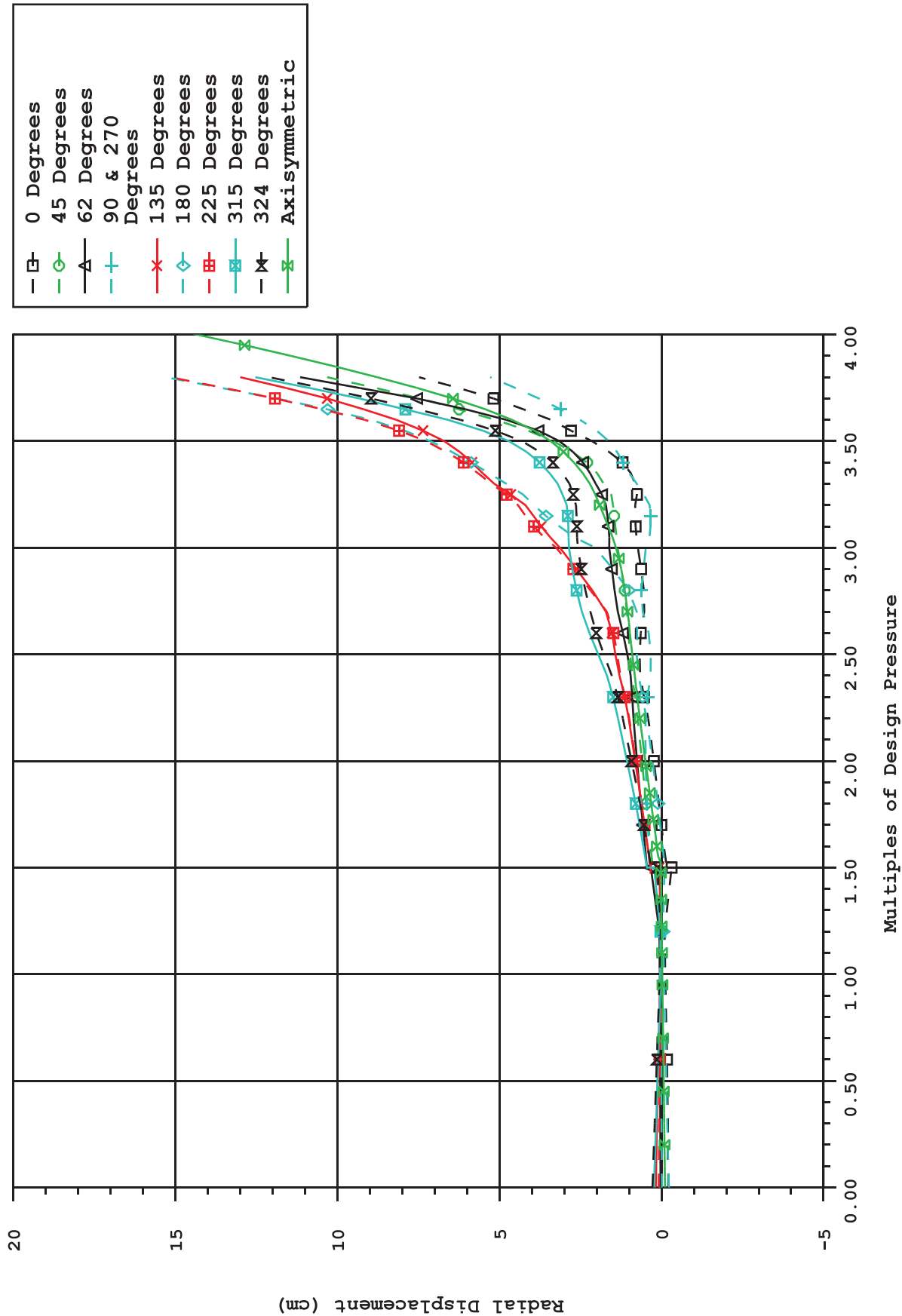


Figure 6-31. Radial Displacement at Elev. 6.2M, Posttest 3DCM Run 7 (No Friction After Prestress is Overcome) Compared to Axisymmetric

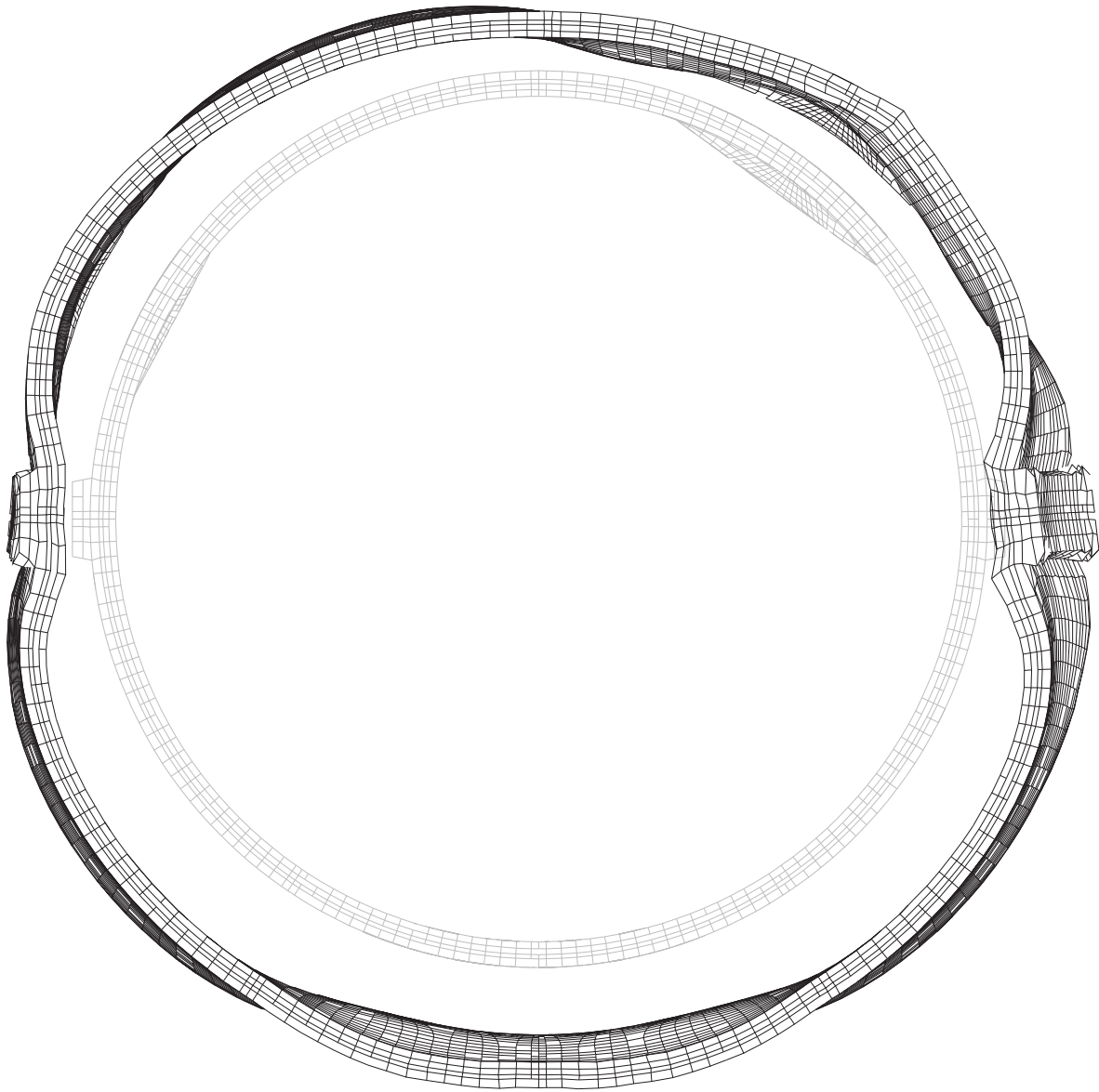
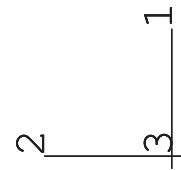


Figure 6-32. 3DCM Posttest Deformed Shape at $P = 2.0 P_d$, Run 7 (mag. Factor = $100\times$)



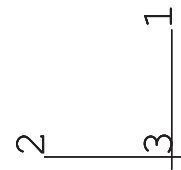
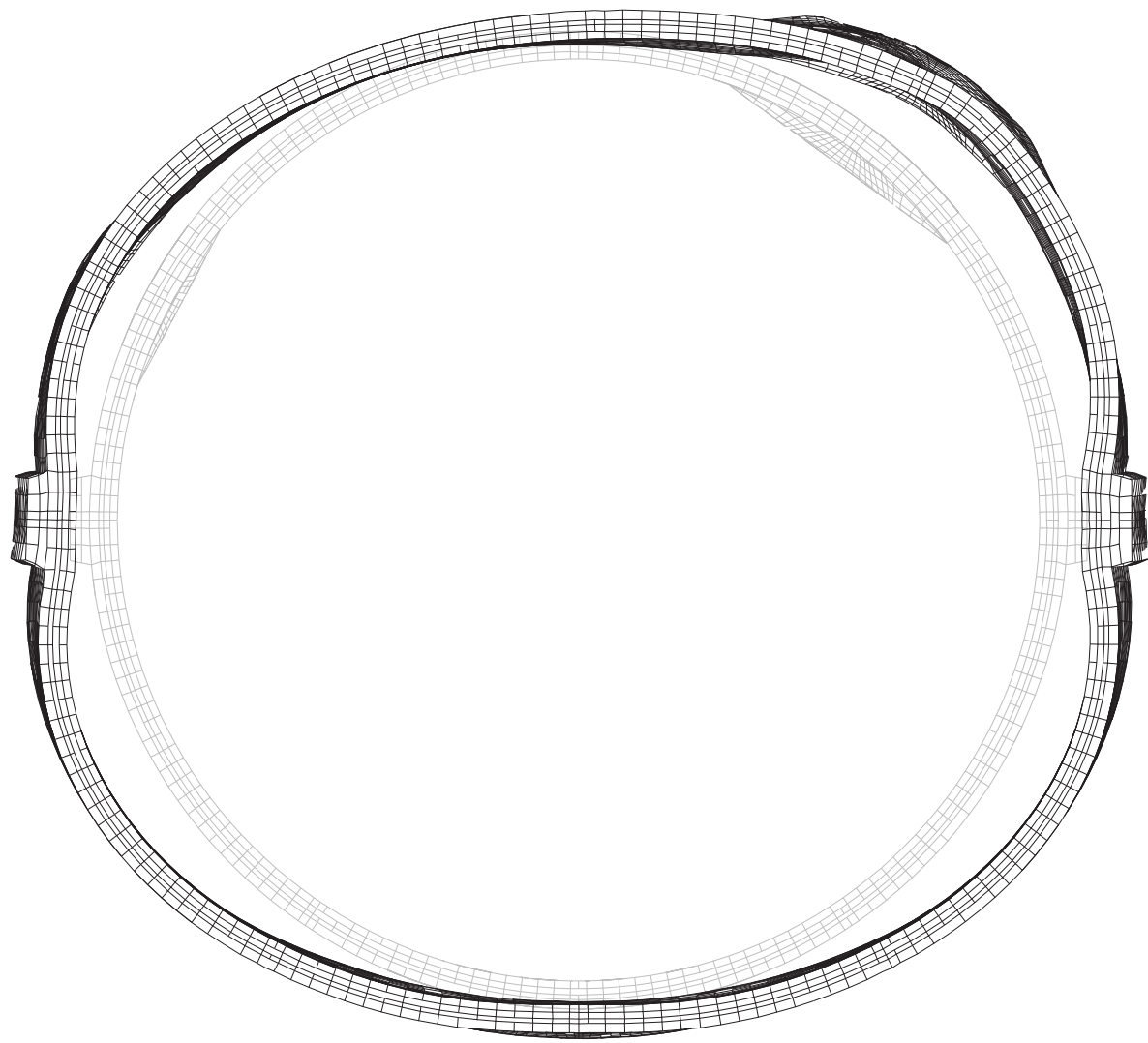


Figure 6-33. 3DCM Posttest Deformed Shape at $P = 3.8$ Pd, Run 7 (mag. Factor = $10\times$)

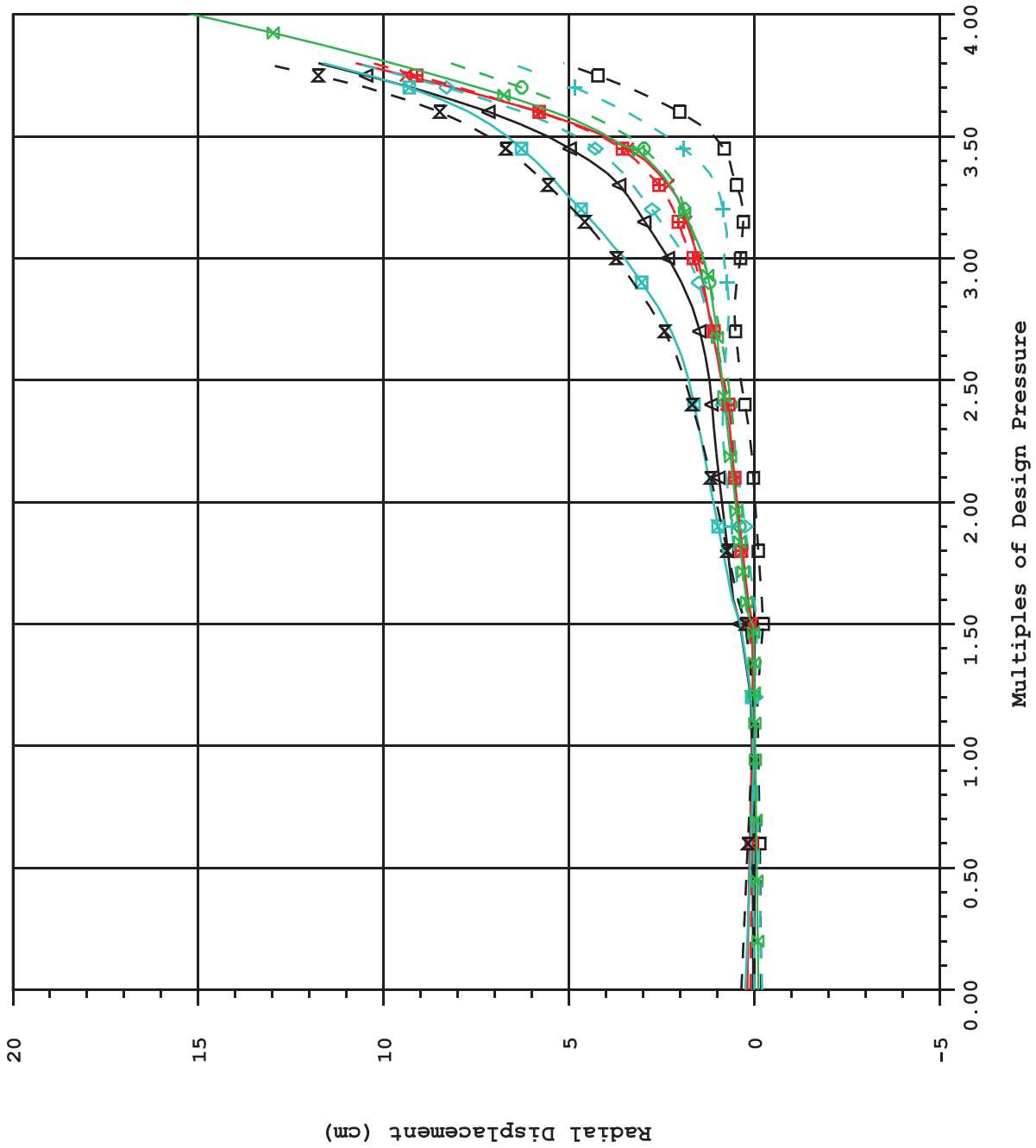


Figure 6-34. Radial Displacement at Elev. 4.7M, Posttest 3DCM Run 9 (Bi-directional Friction) Compared to Axisymmetric

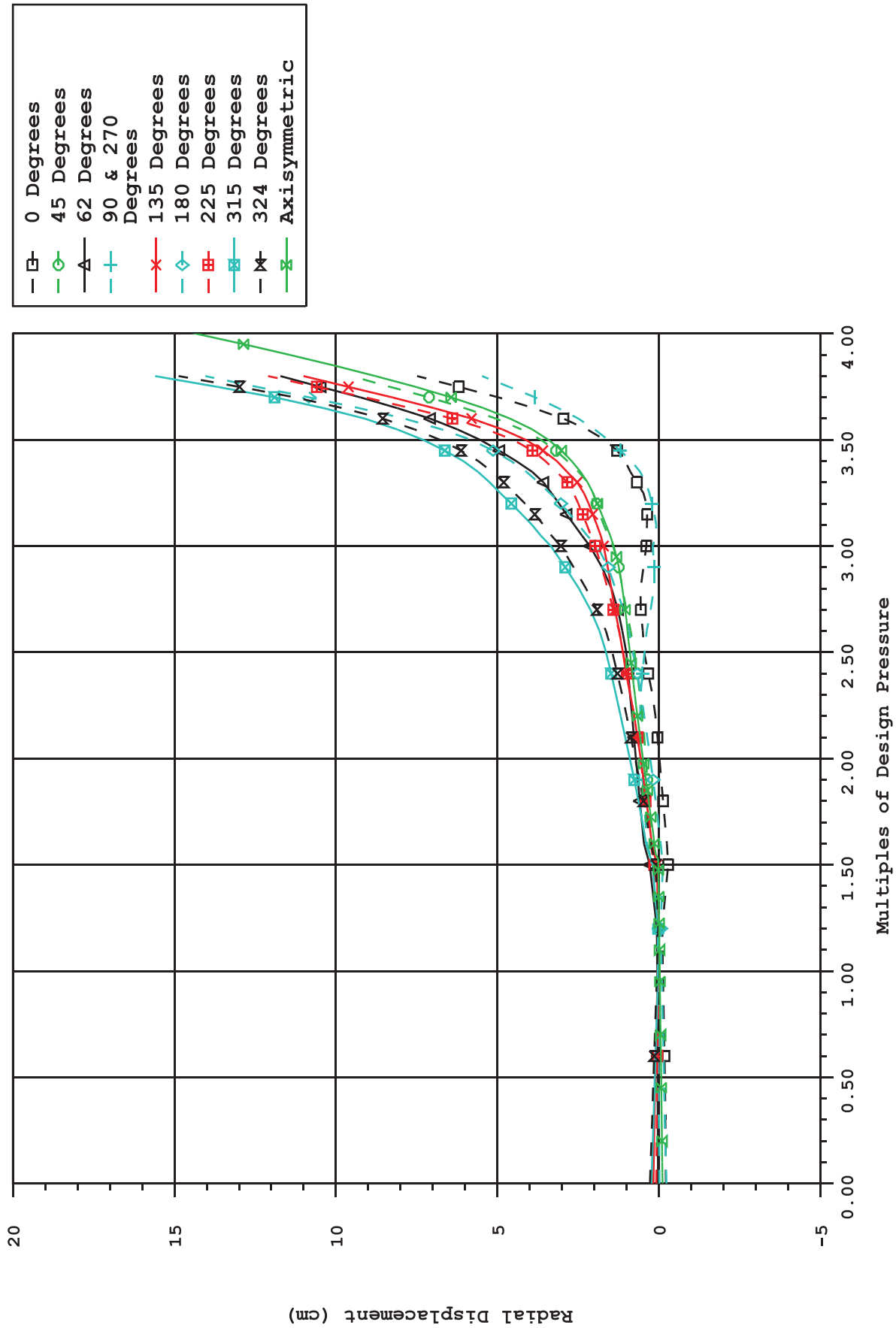
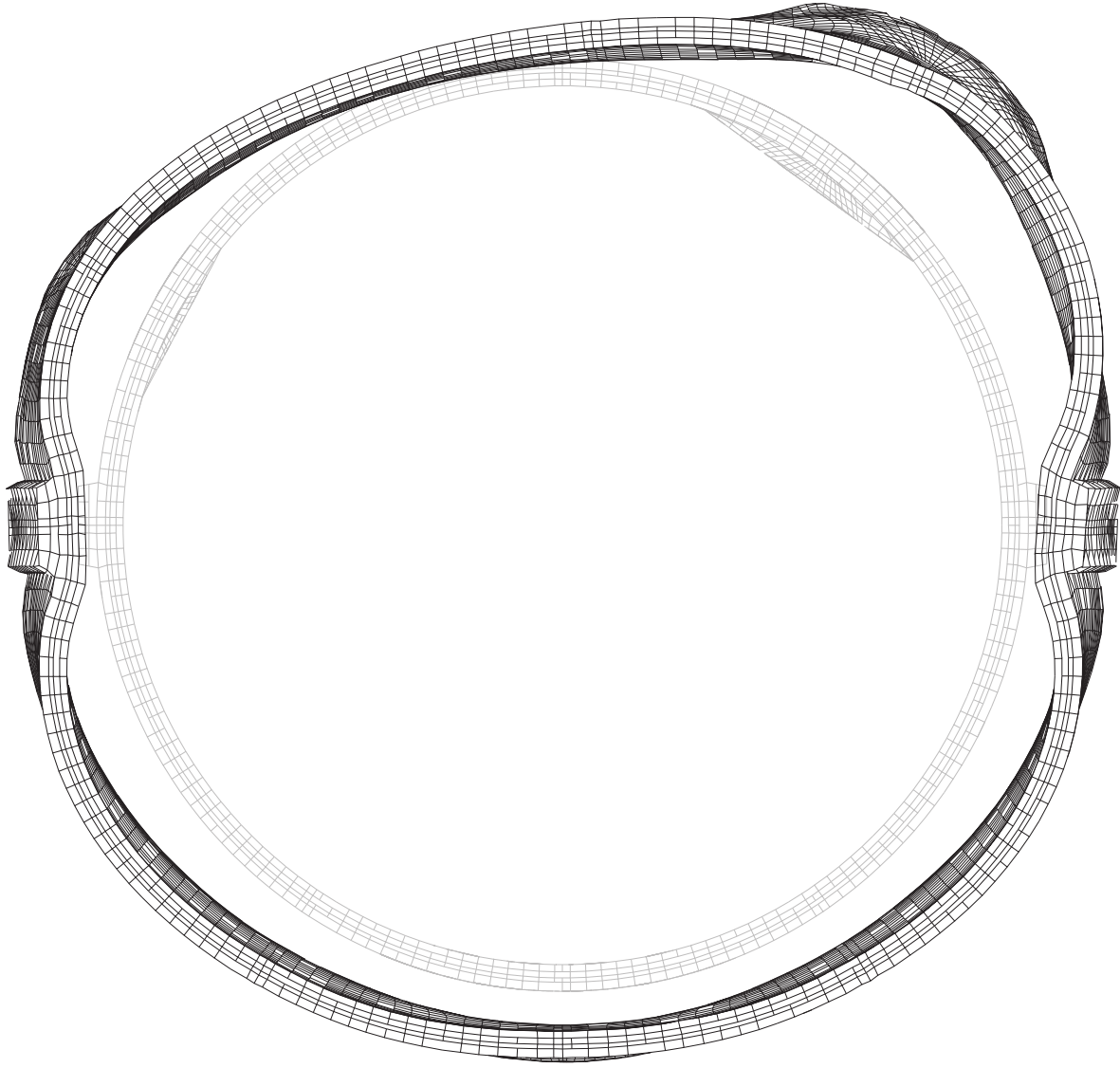


Figure 6-35. Radial Displacement at Elev. 6.2M, Posttest 3DCM Run 9 Compared to Axisymmetric



2
3
1

Figure 6-36. 3DCM Posttest Deformed Shape at $P = 2.5$ Pd, Run 9 (mag. Factor = $100\times$)

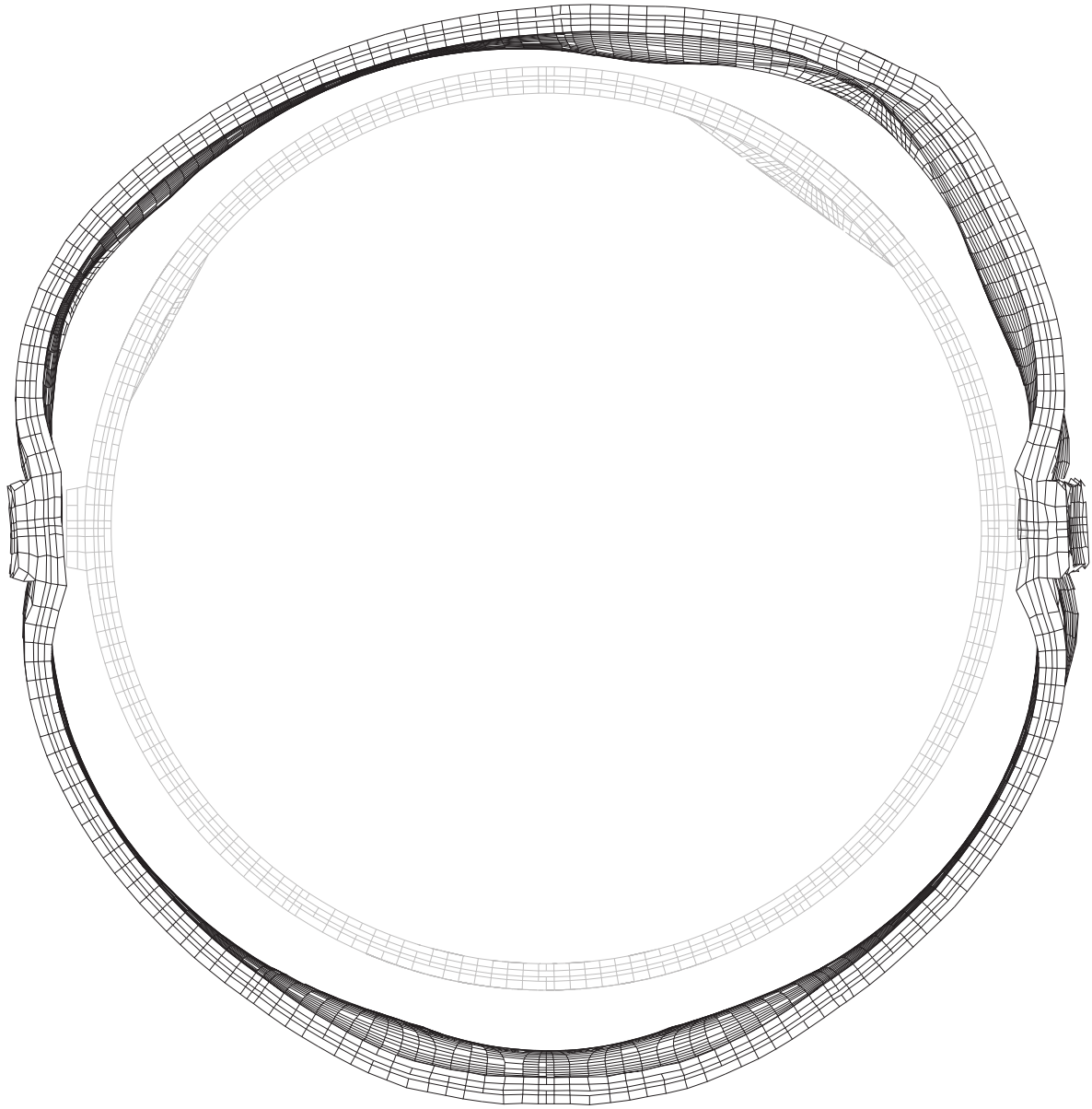


Figure 6-37. 3DCM Posttest Deformed Shape at $P = 3.8 P_d$, Run 9 (mag. Factor = $10\times$)

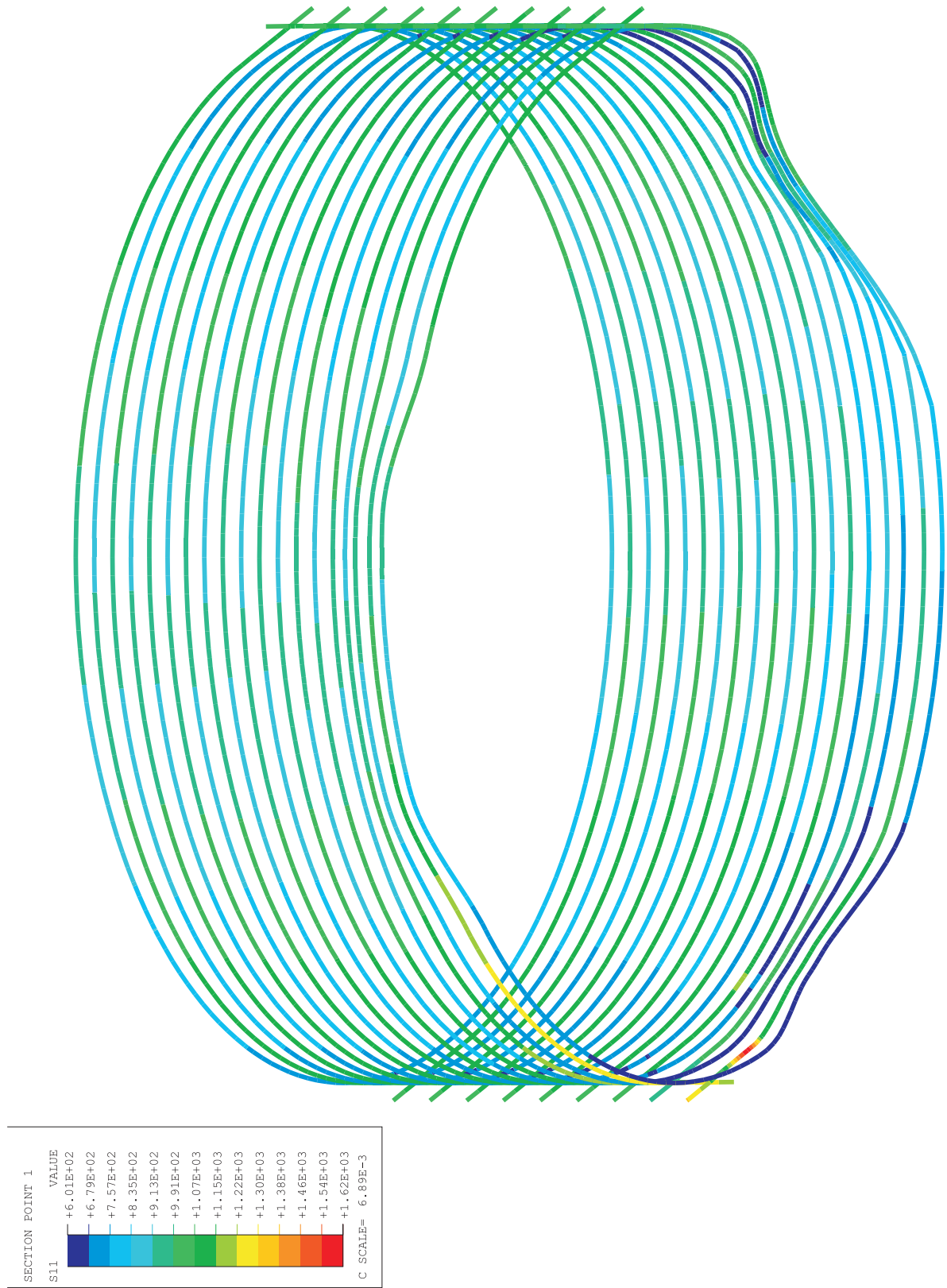


Figure 6-38. 3DCM Posttest Tendon Stress Contours at P = 1.5 Pd, Run 6

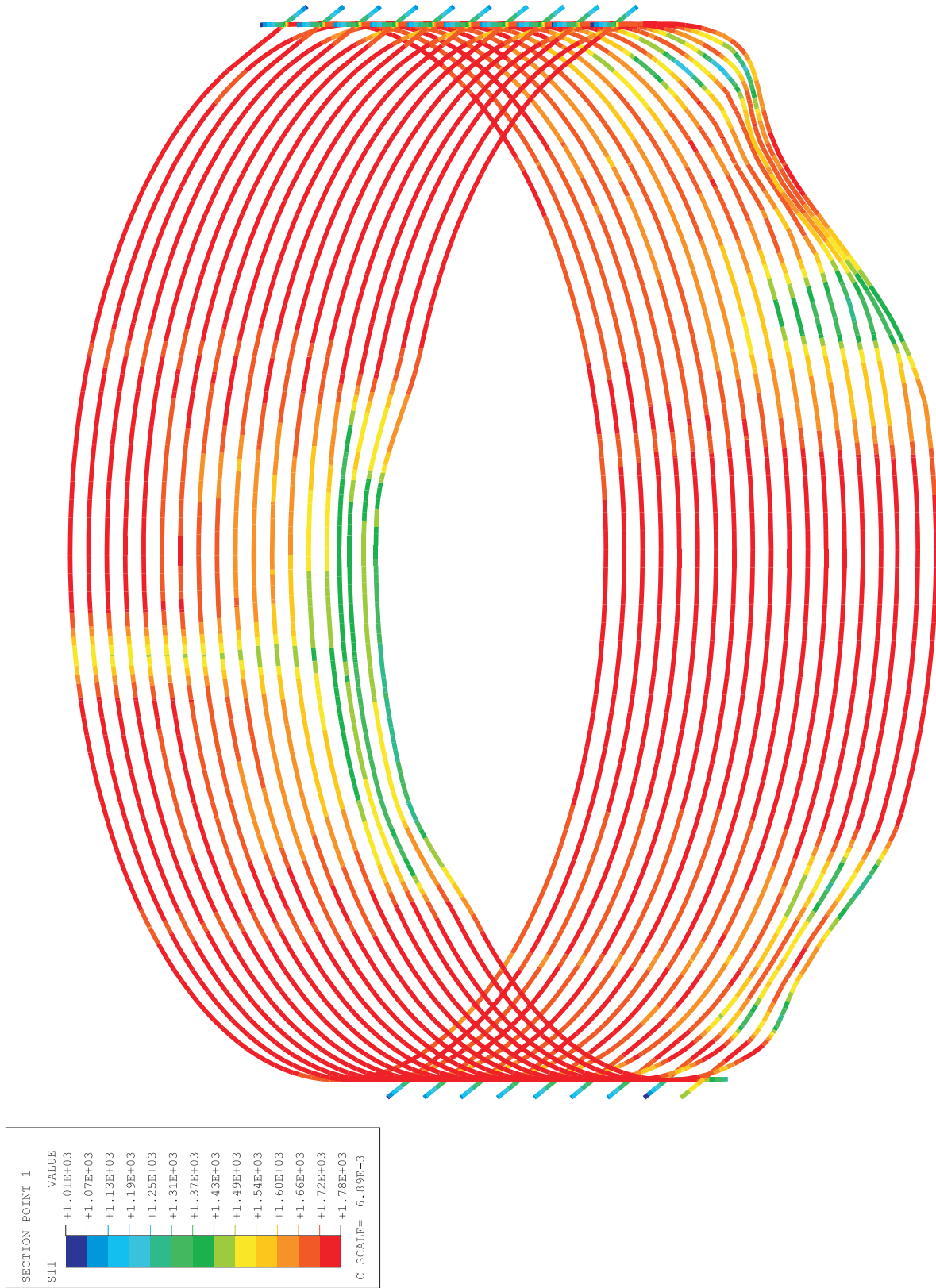


Figure 6-39. 3DCM Posttest Tendon Stress Contours at P = 3.5 Pd, Run 6

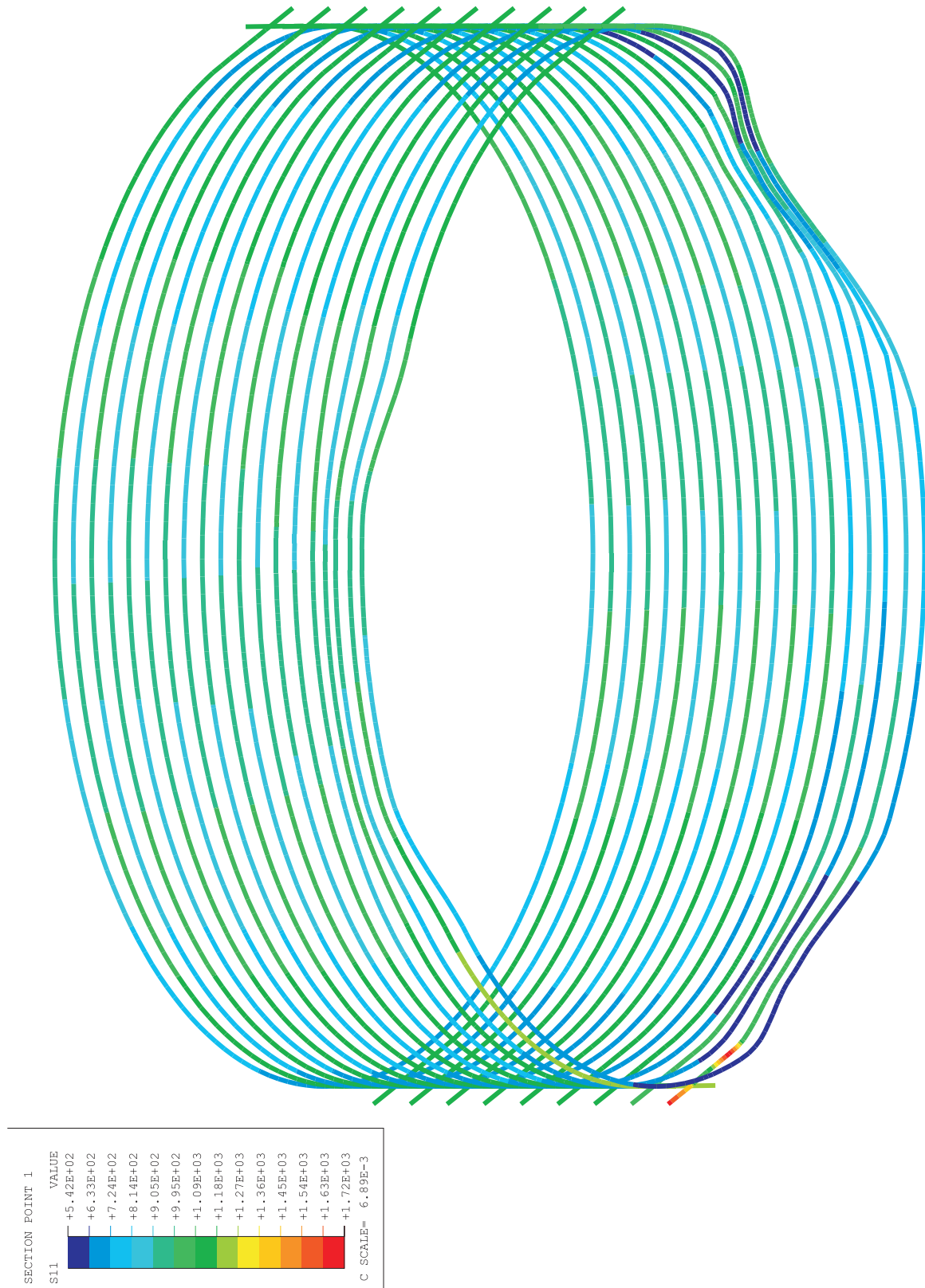


Figure 6-40. 3DCM Posttest Tendon Stress Contours at P = 1.5 Pd, Run 7, Before Friction Element Modeling Modification

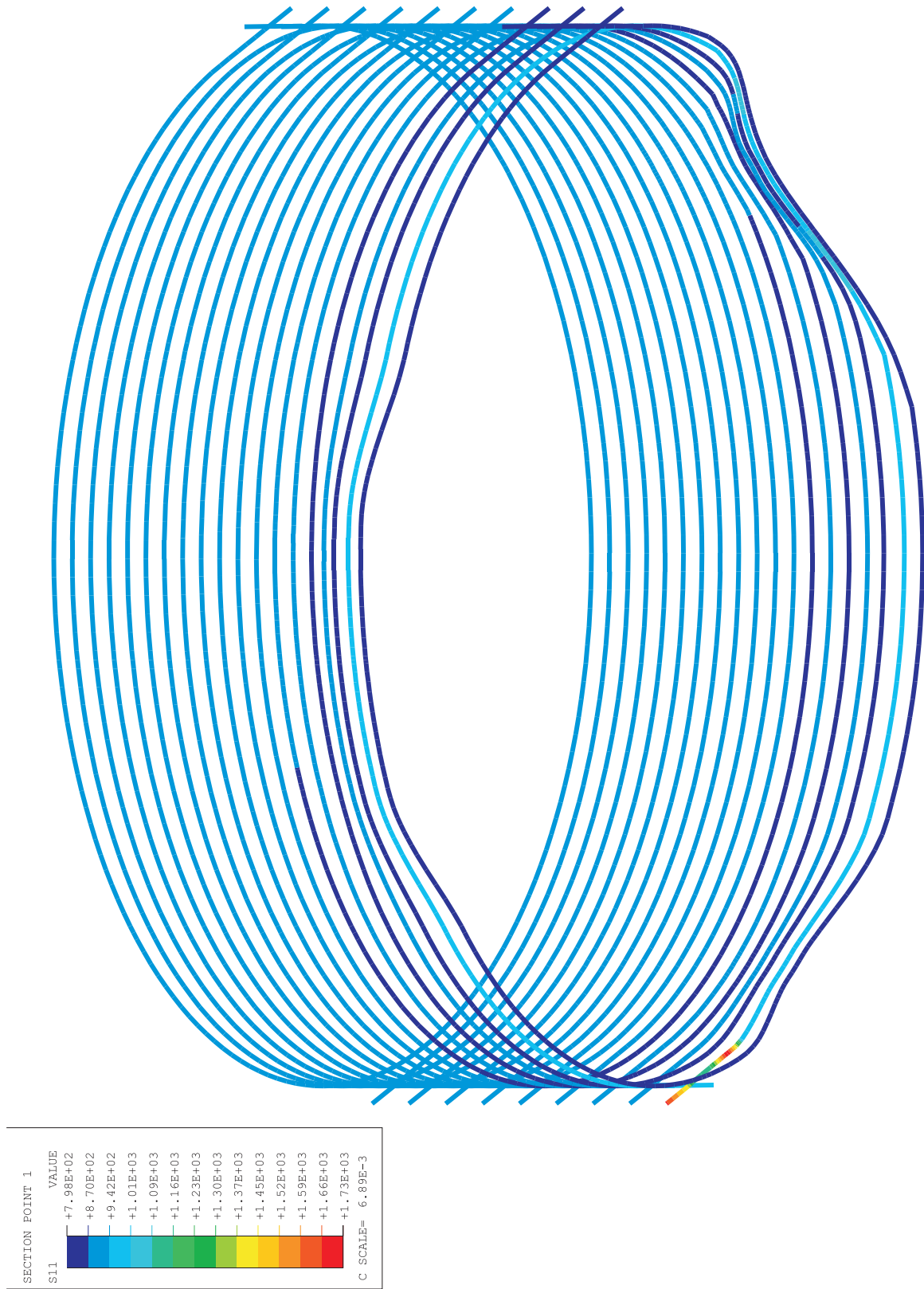


Figure 6-41. 3DCM Posttest Tendon Stress Contours at P = 1.5 Pd, Run 7, After Friction Element Modeling Modification

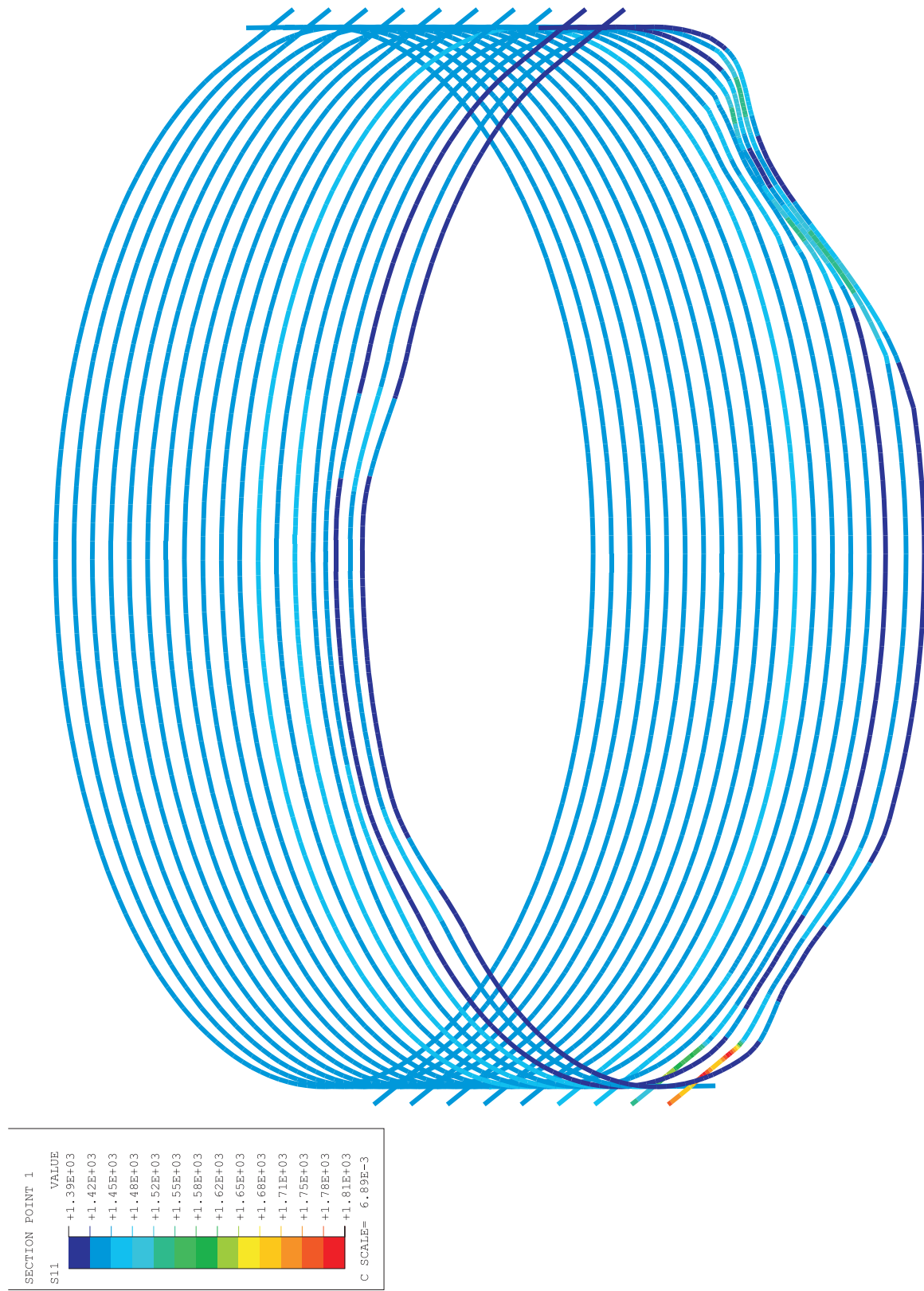


Figure 6-42. 3DCM Posttest Tendons Stress Contours at P = 3.5 Pd, Run 7

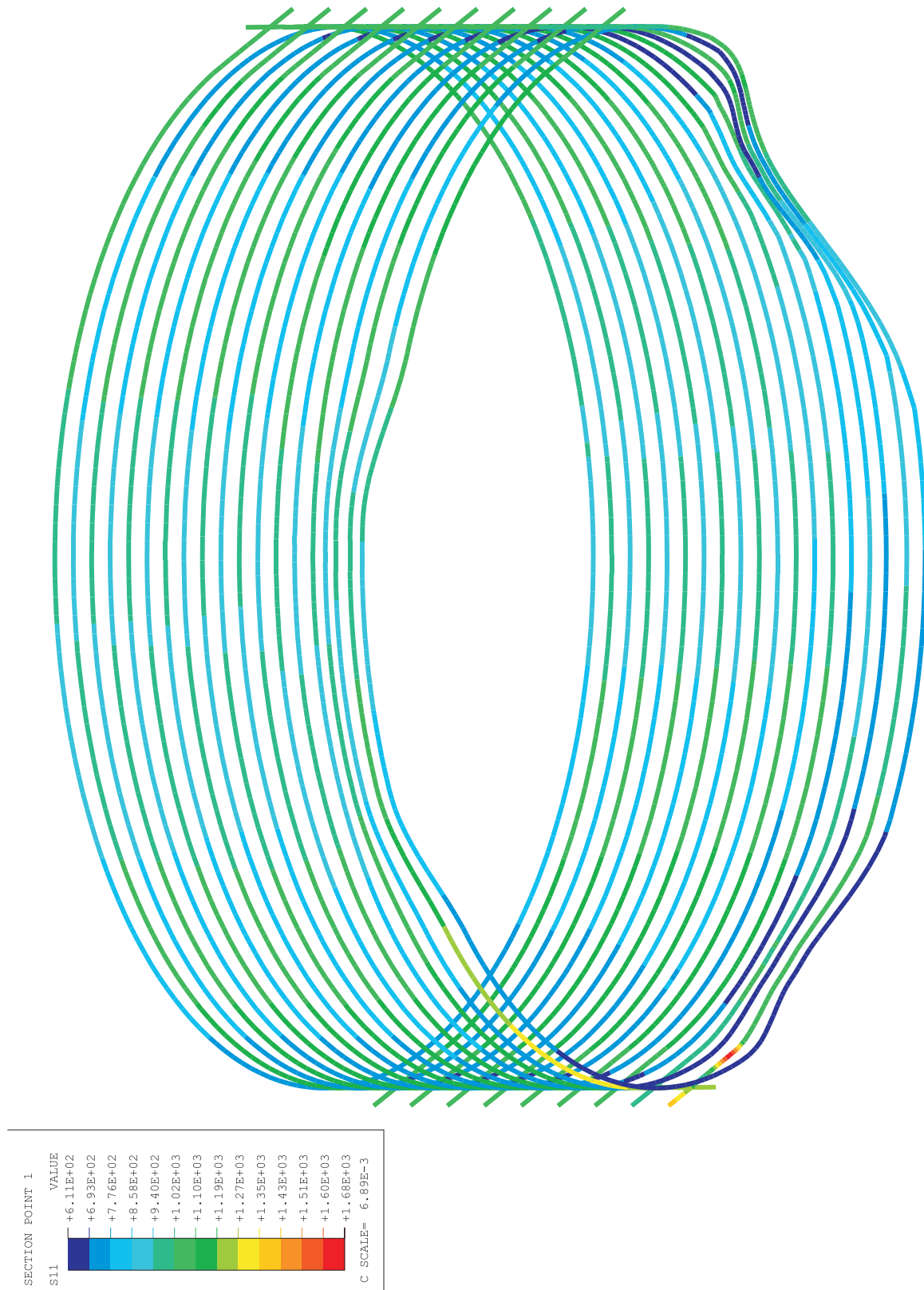


Figure 6-43. 3DCM Posttest Tendon Stress Contours at P = 1.5 Pd, Run 9

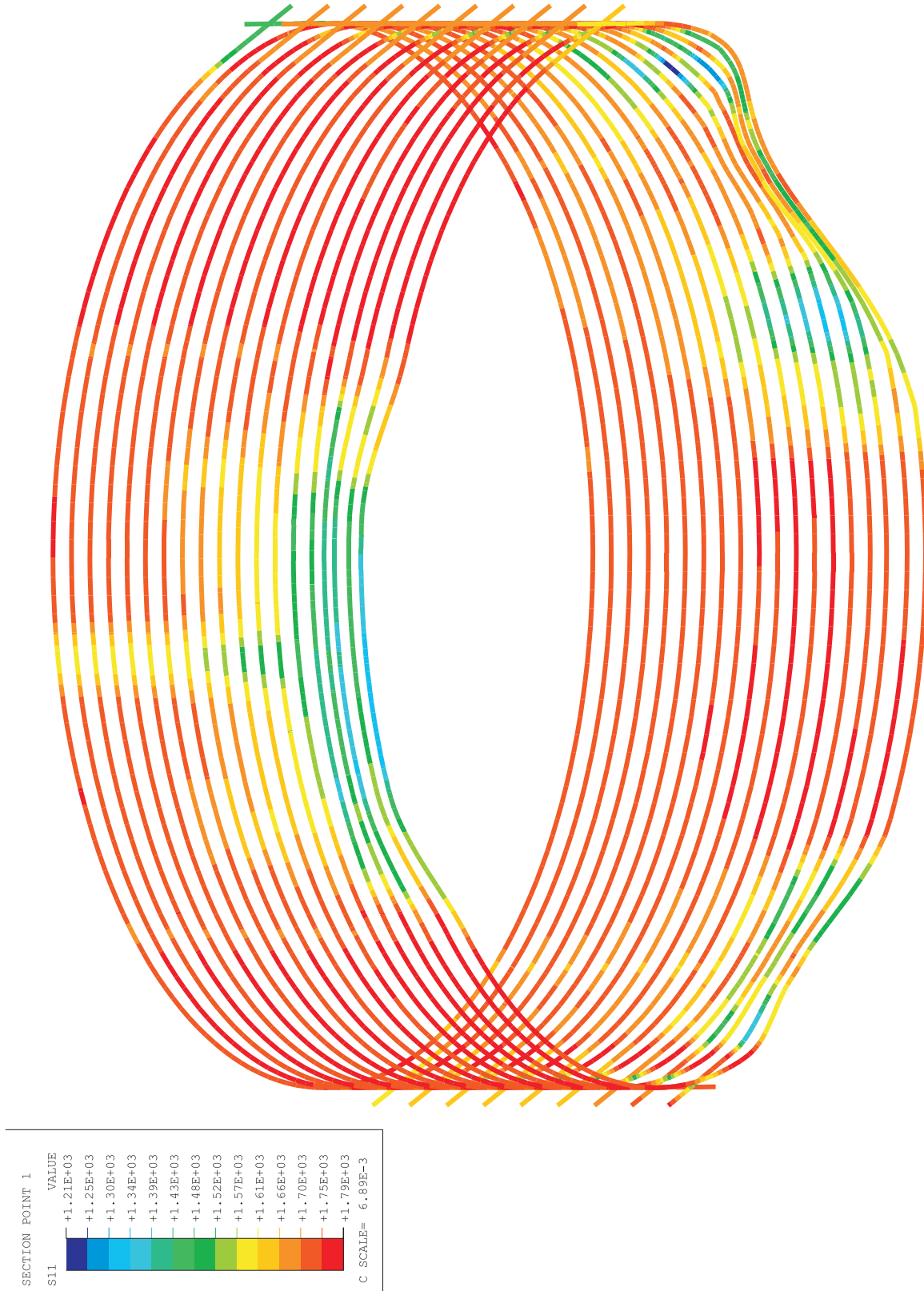


Figure 6-44. 3DCM Posttest Tendon Stress Contours at P = 3.5 Pd, Run 9

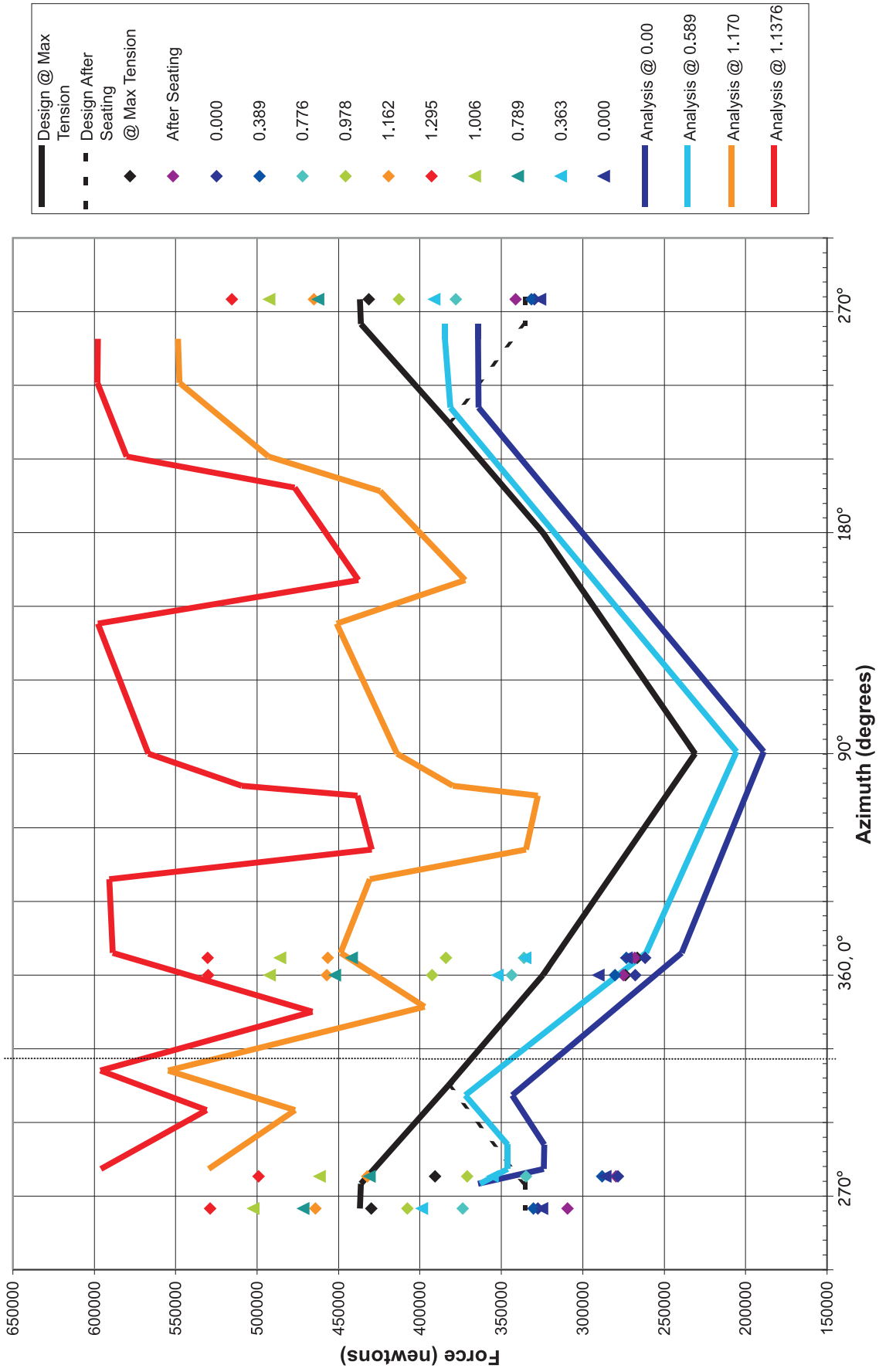


Figure 6-45. H35 Hoop Tendon Force Comparisons to Posttest Run #6

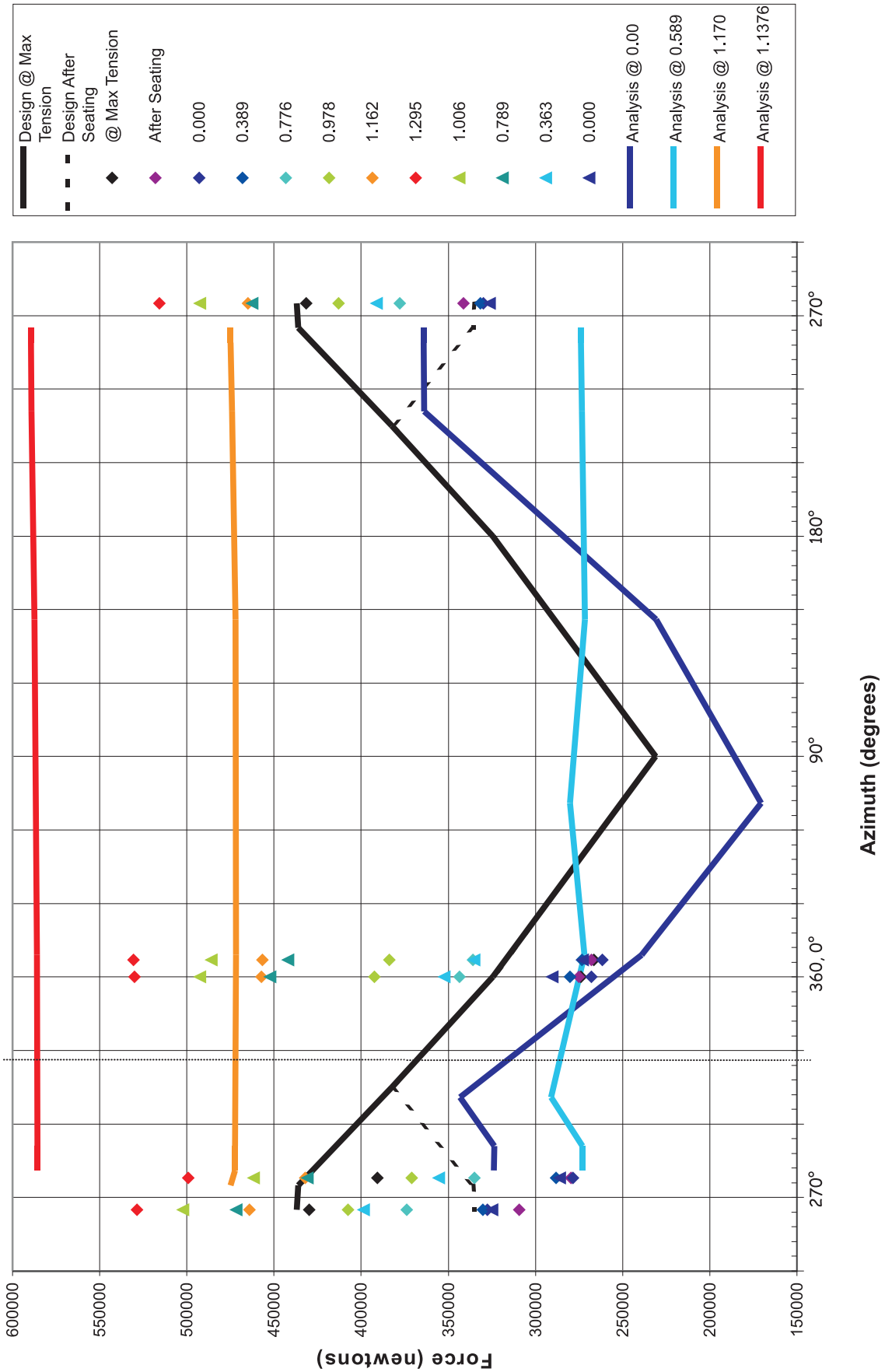


Figure 6-46. H35 Hoop Tendon Force Comparisons to Posttest Run #7

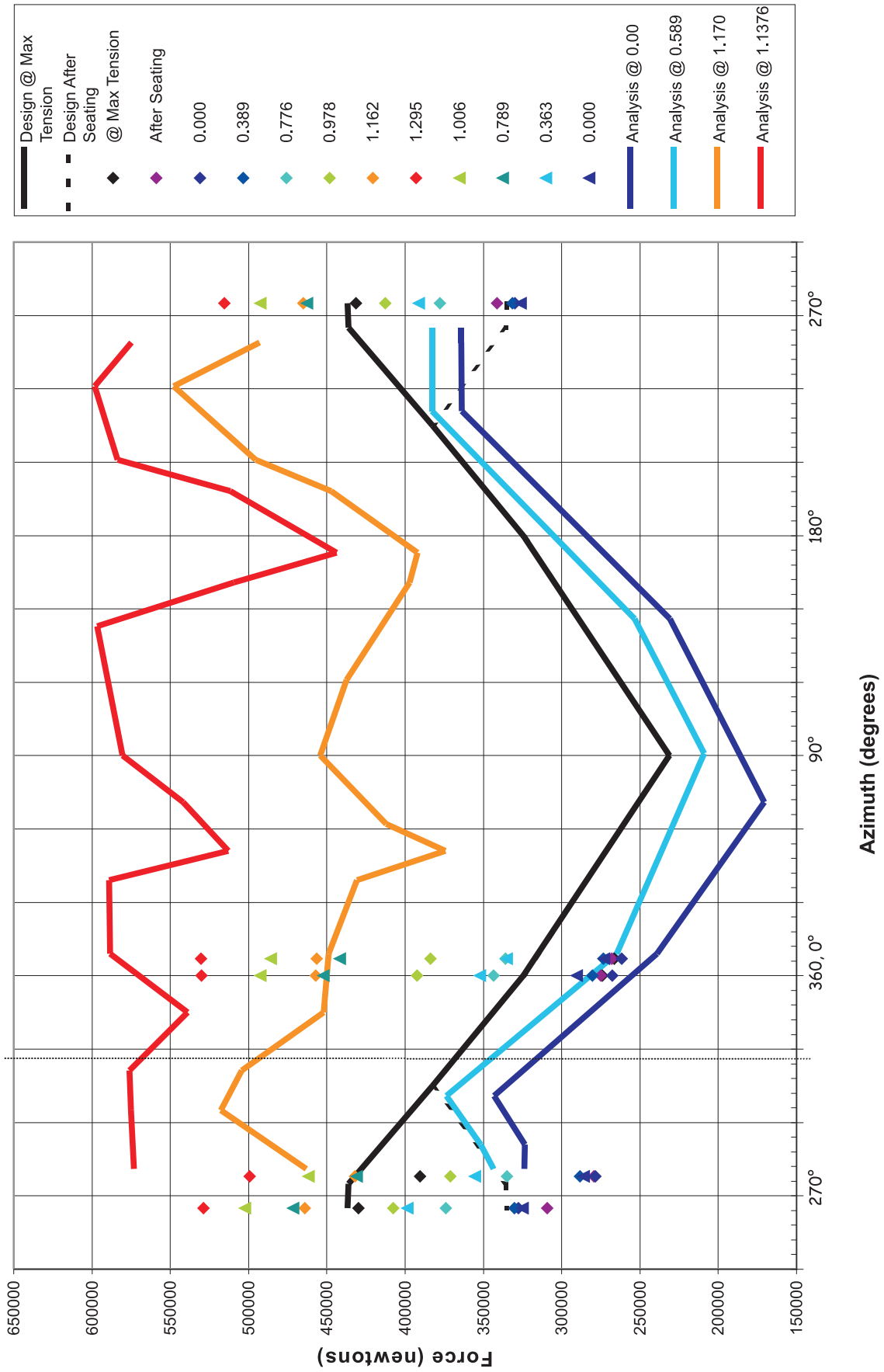


Figure 6-47. H35 Hoop Tendon Force Comparisons to Posttest Run #9

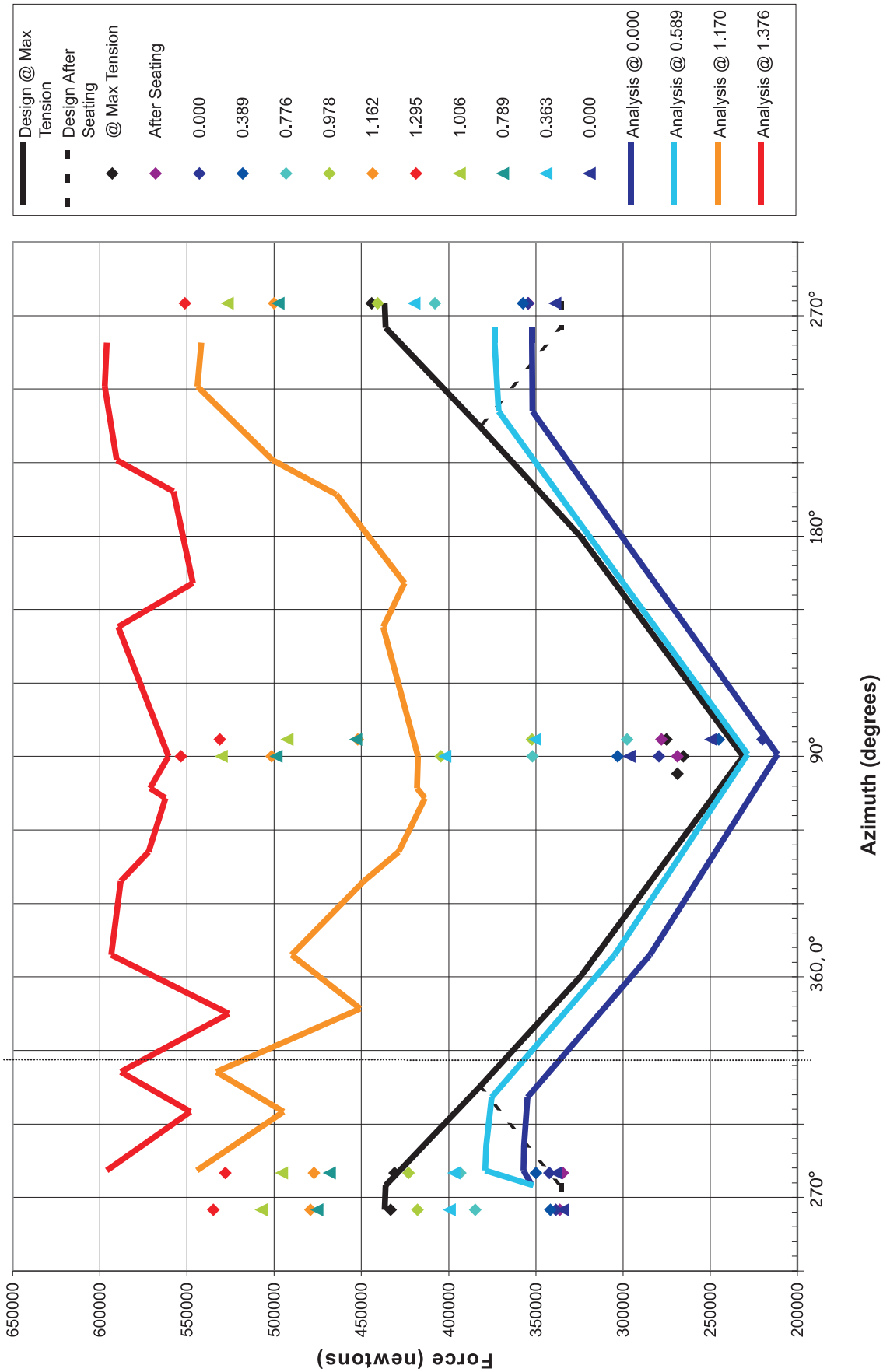


Figure 6-48. H53 Hoop Tendon Force Comparisons to Posttest Run #6

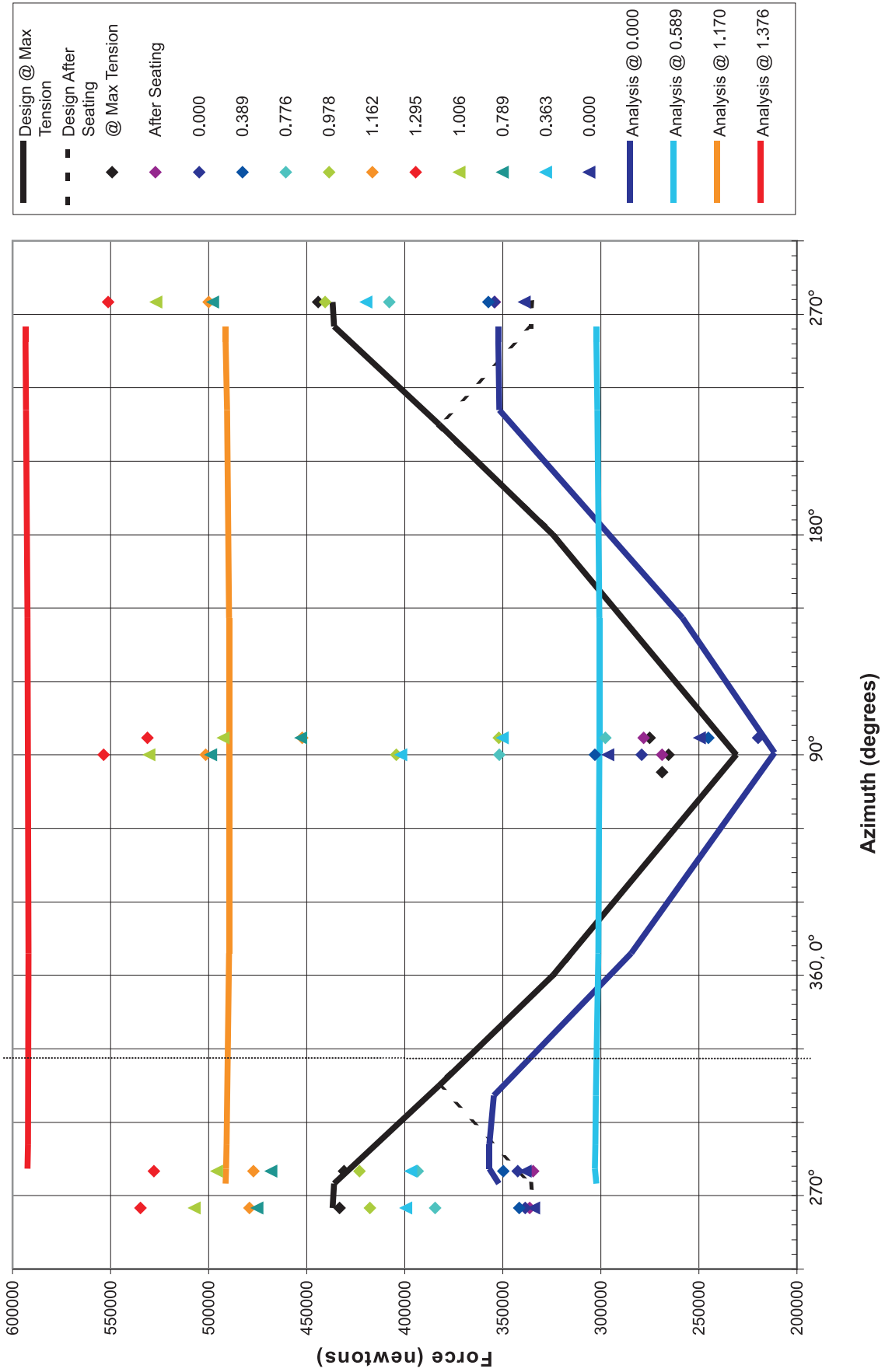


Figure 6-49. H53 Hoop Tendon Force Comparisons to Posttest Run #7

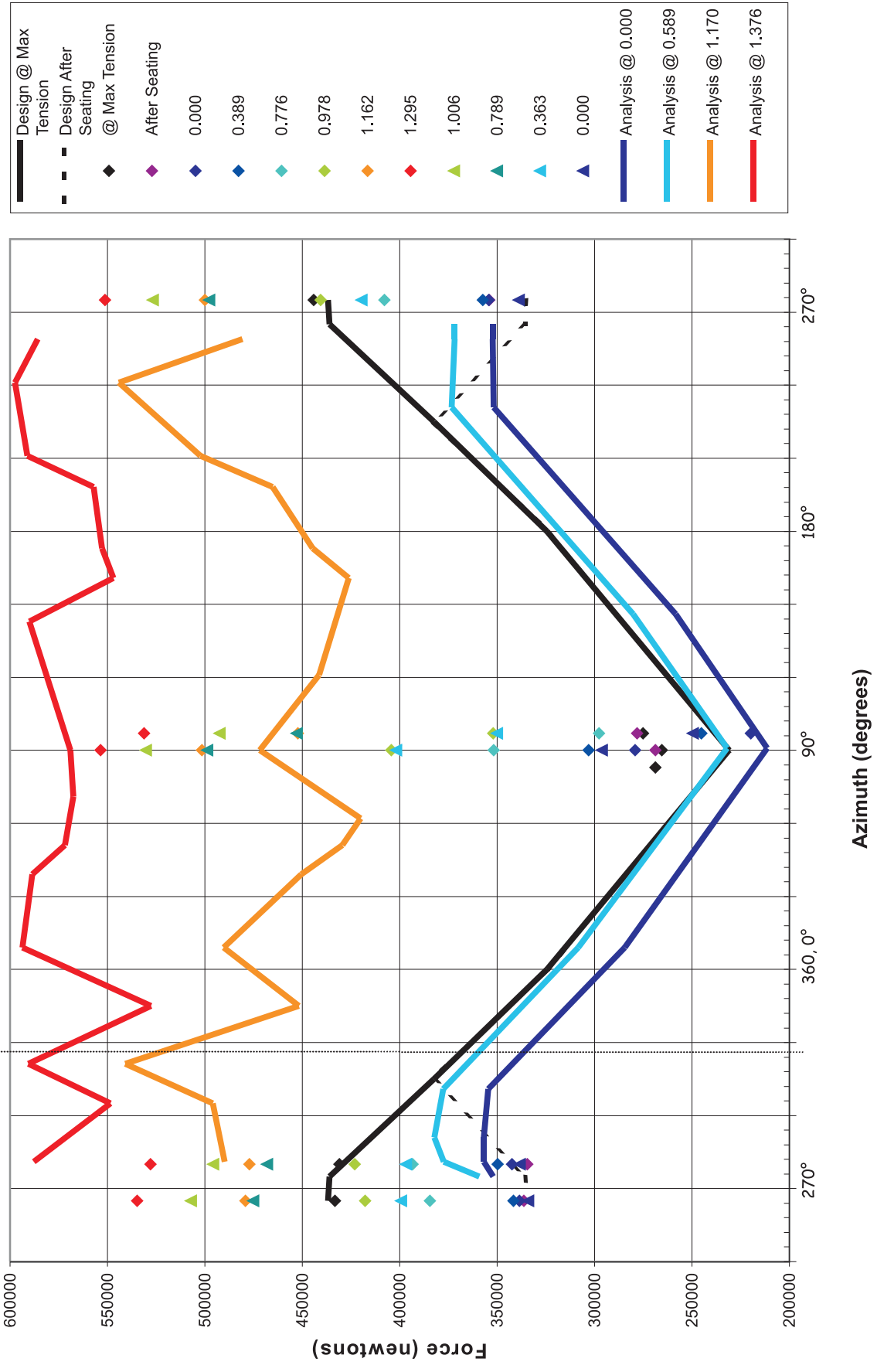
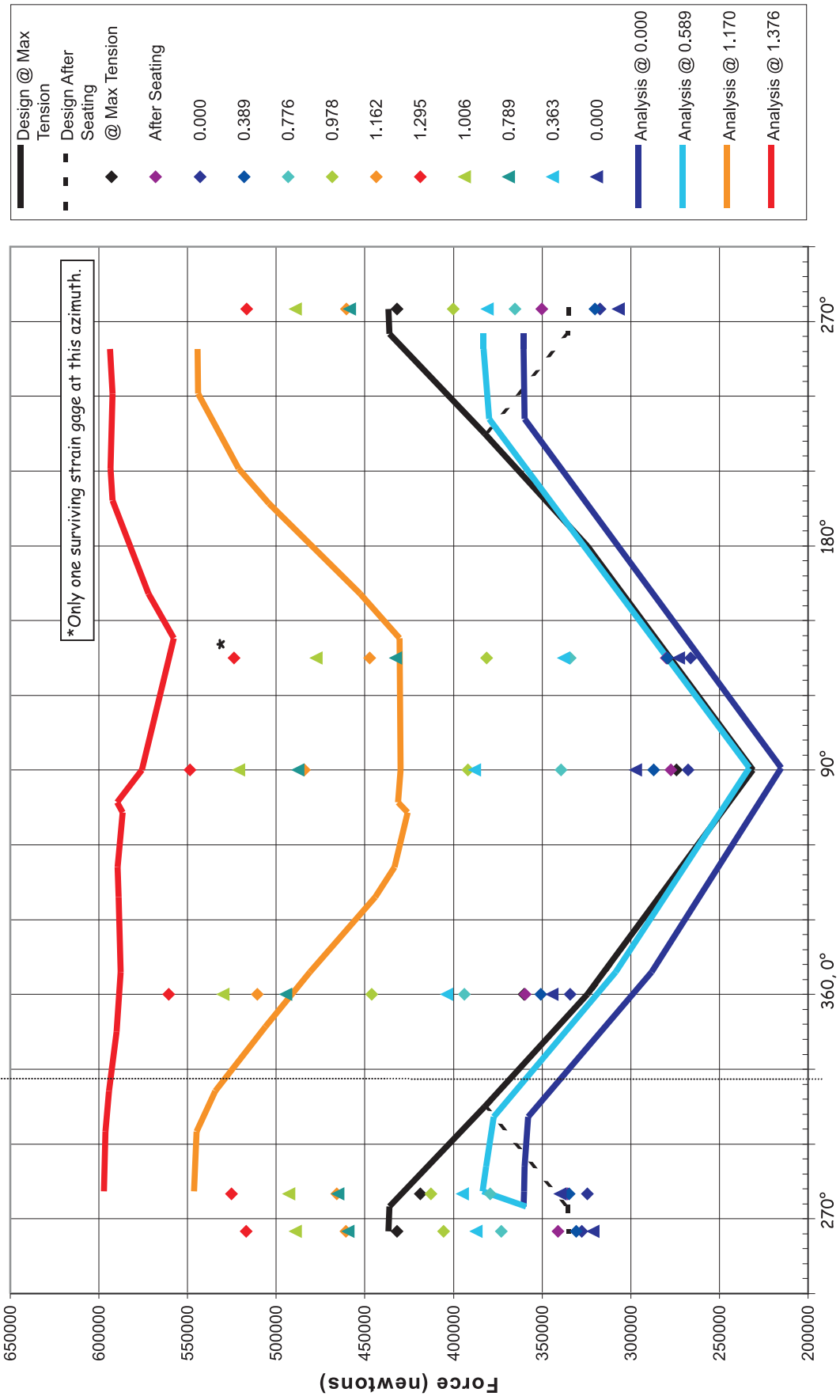


Figure 6-50. H53 Hoop Tendon Force Comparisons to Posttest Run #9



Azimuth (degrees)

Figure 6-51. H67 Hoop Tendon Force Comparisons to Posttest Run #6

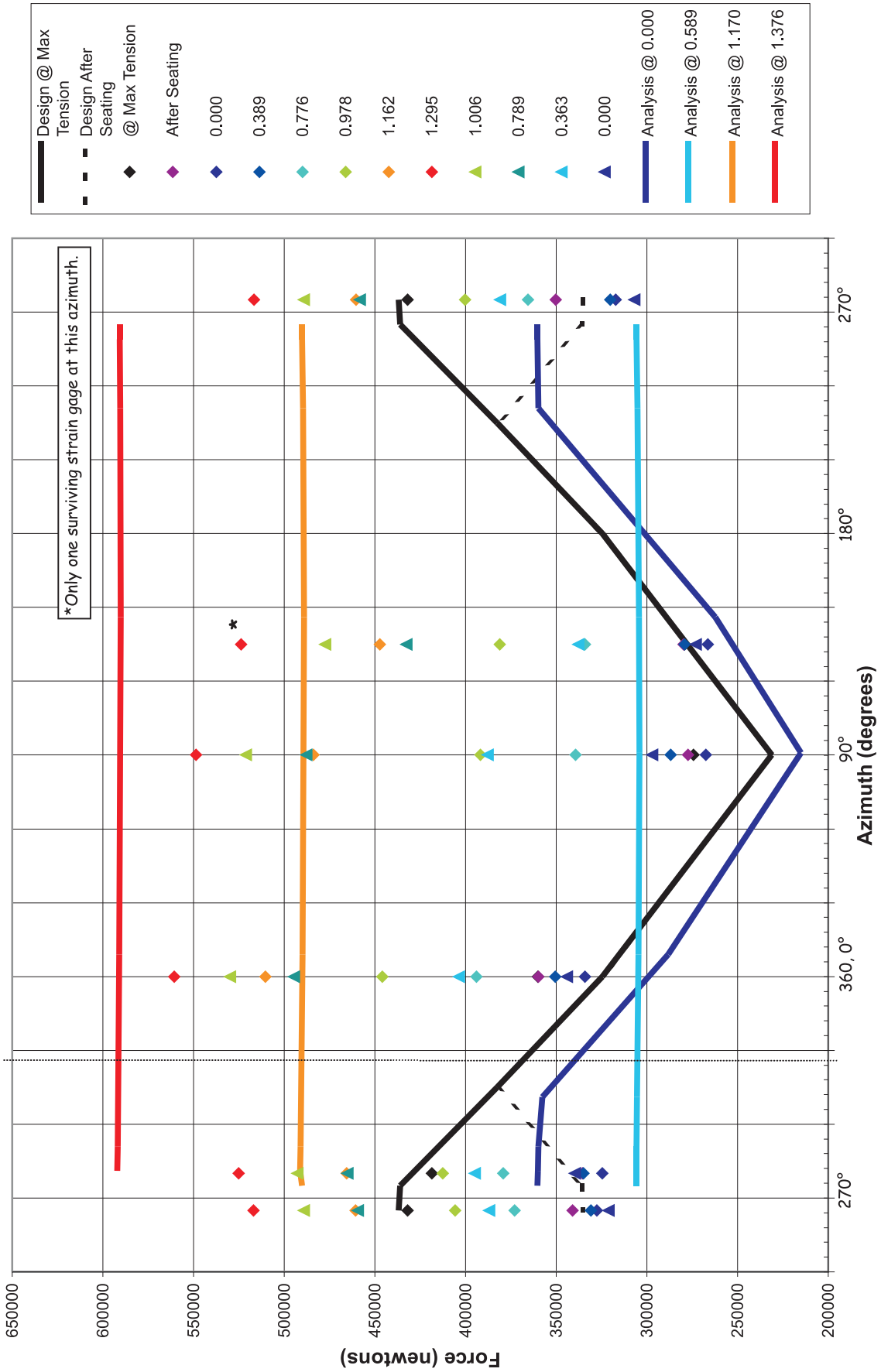


Figure 6-52. H67 Hoop Tendon Force Comparisons to Posttest Run #7

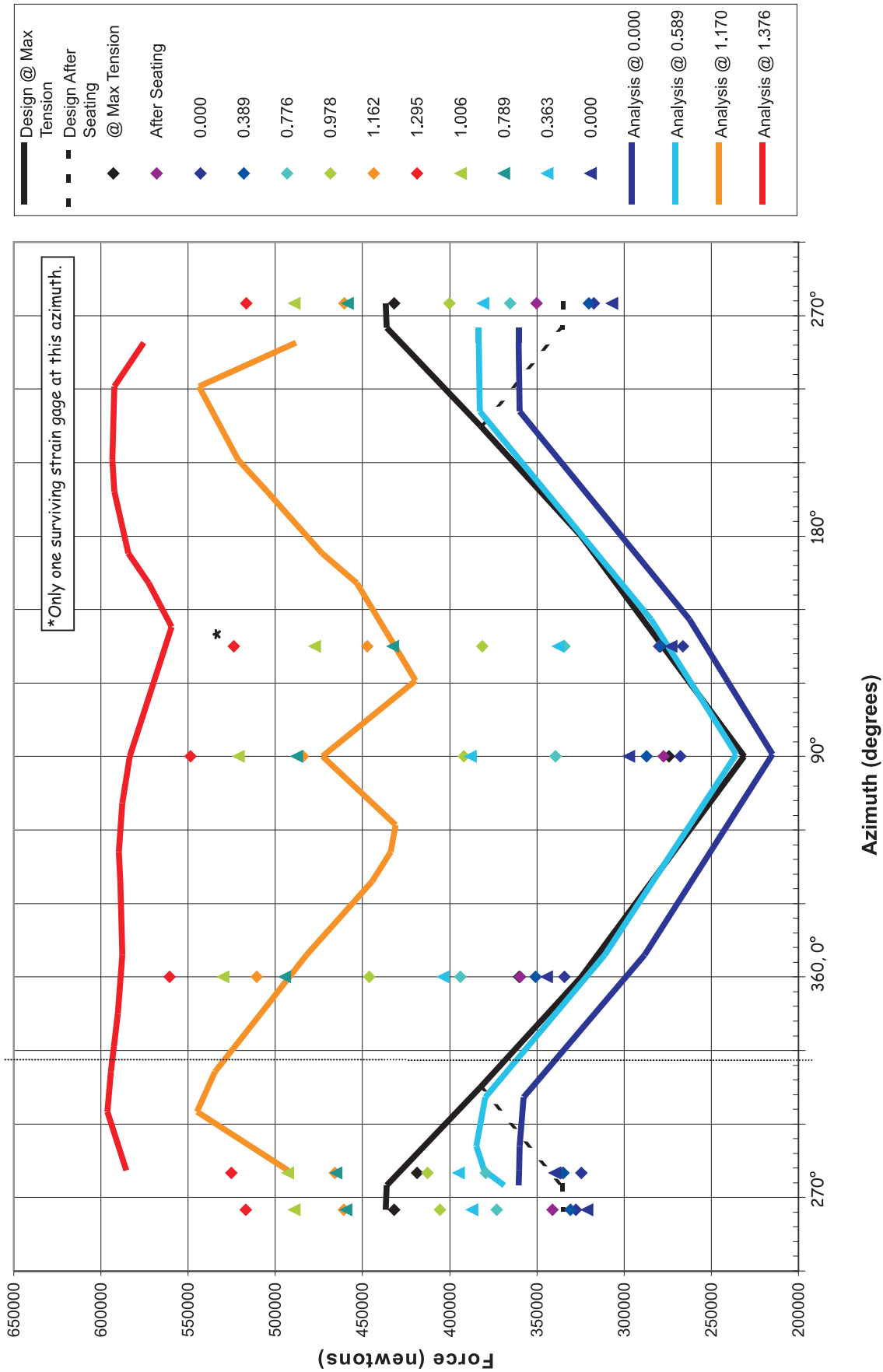


Figure 6-53. H67 Hoop Tendon Force Comparisons to Posttest Run #9

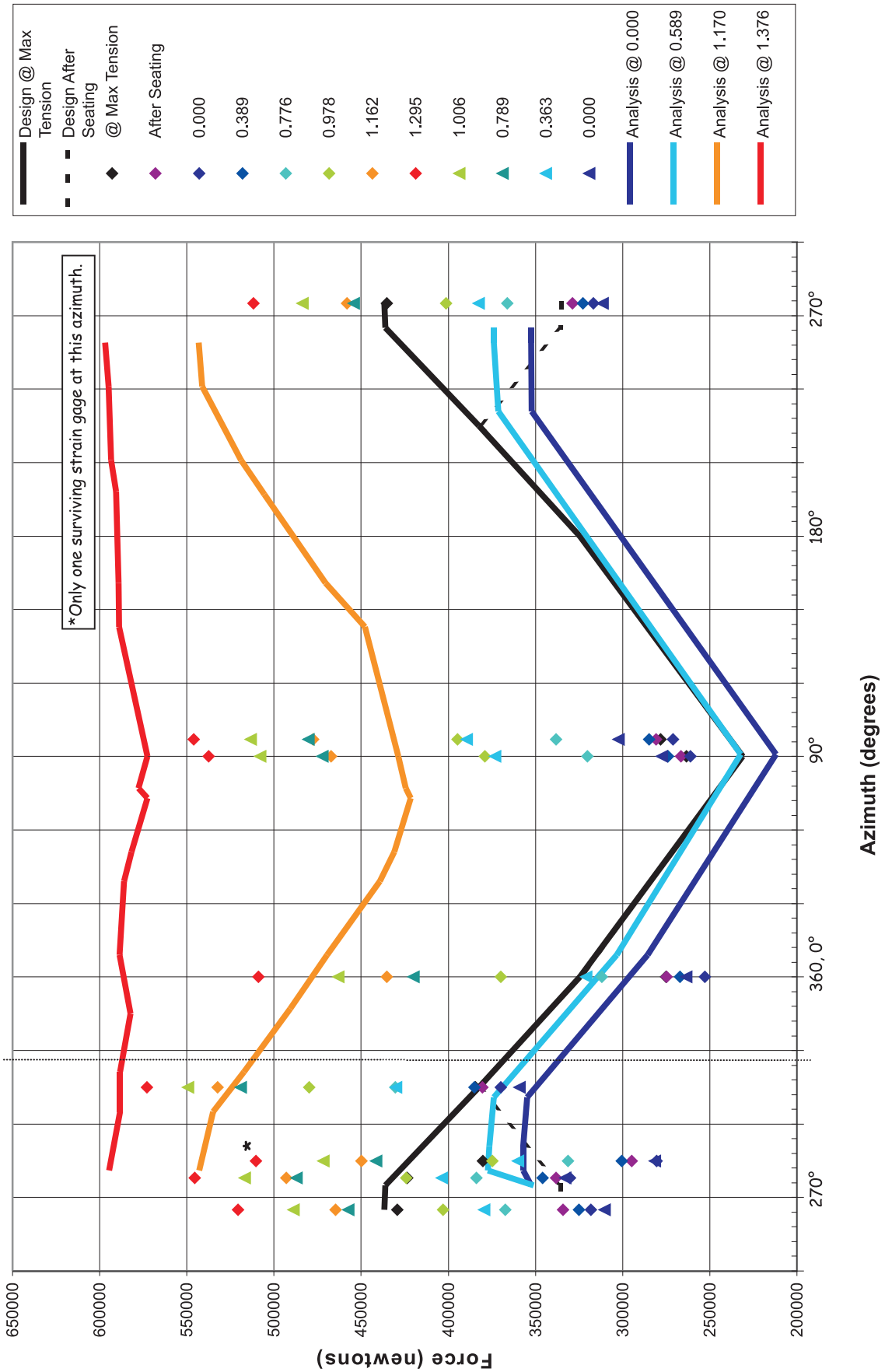


Figure 6-54. H68 Hoop Tendon Force Comparisons to Posttest Run #6

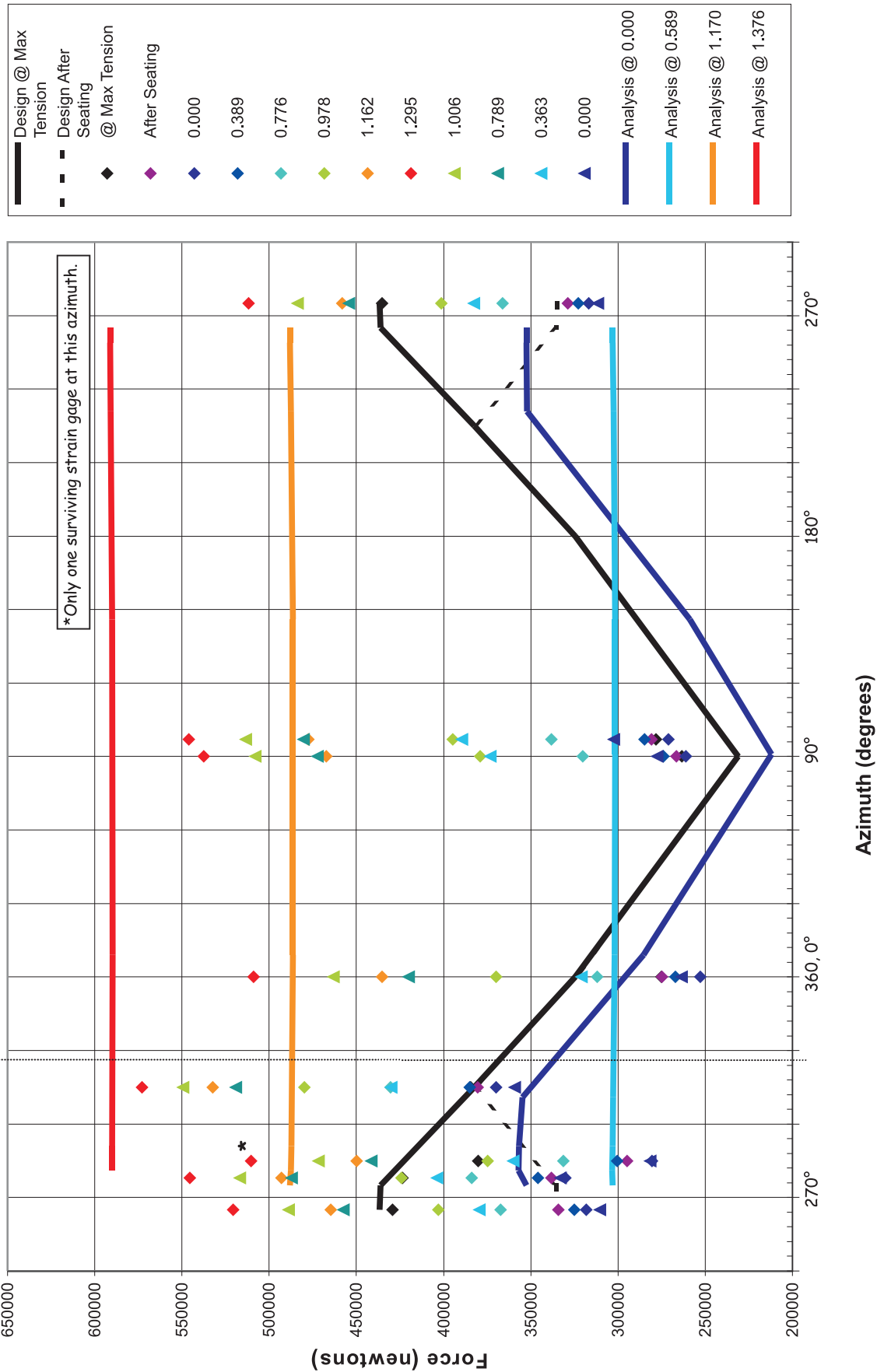


Figure 6-55. H68 Hoop Tendon Force Comparisons to Posttest Run #7

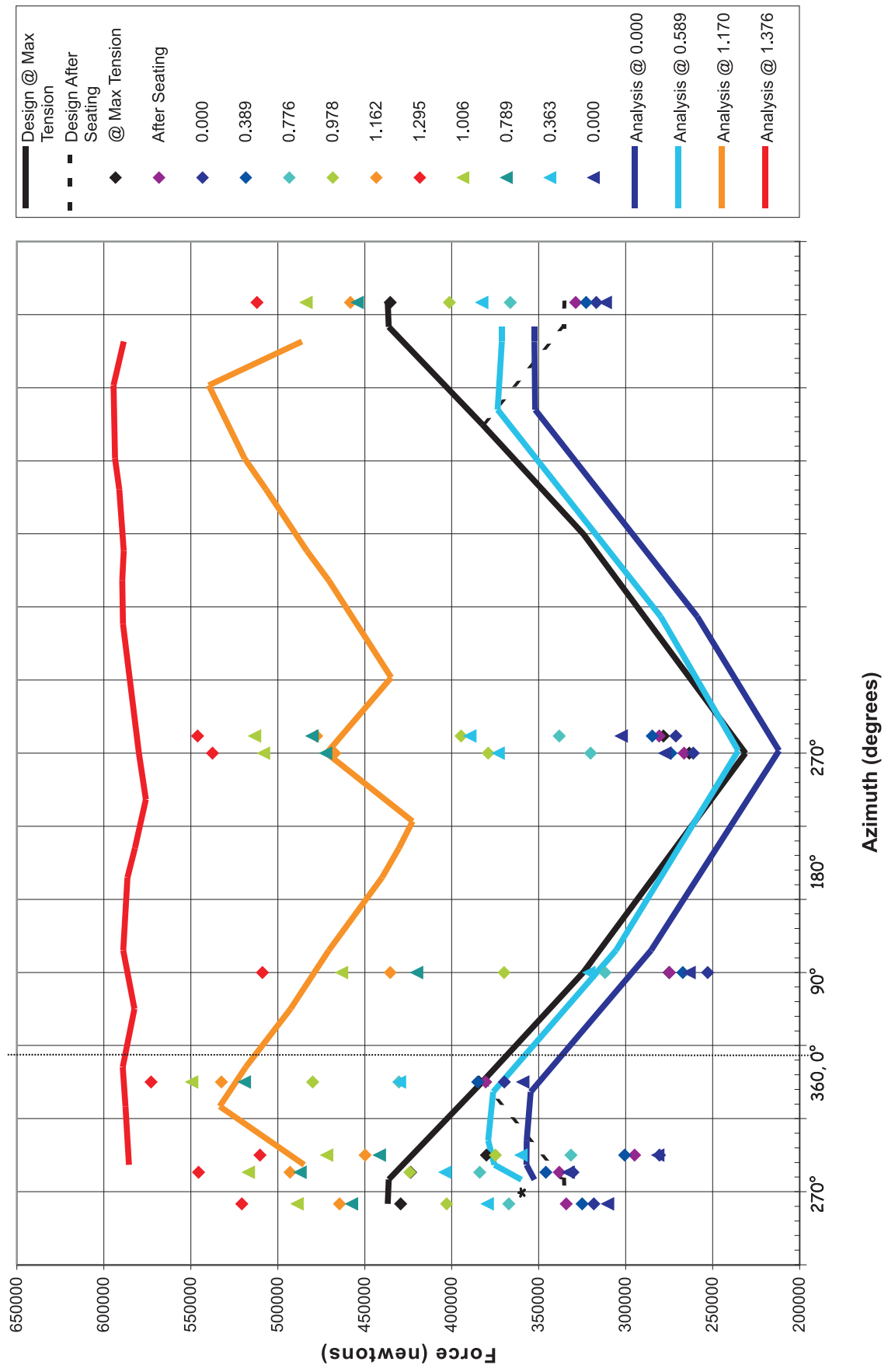


Figure 6-56. H68 Hoop Tendon Force Comparisons to Posttest Run #9